I. Dynamics at the Galileo Probe Site on Jupiter

and

II. Orbital and Thermal Evolution of Ganymede

Dissertation by

Adam Peter Showman

In Partial Fulfillment of the Requirements

for the Degree of

Doctor of Philosophy

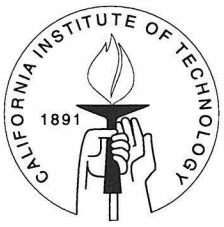

California Institute of Technology

Pasadena, California

1999

(Defended September 10, 1998)

Acknowledgements

I wish to express my gratitude to Andy Ingersoll for the guidance he has given me as my thesis advisor. His creativity, analytical ability, enthusiasm, and especially his humility have all provided inspiration. I've particularly enjoyed our numerous intellectual debates. His friendly manner and genuine interest in getting my feedback on his ideas have led to a comfortable environment for discussion. Further, because of his open style in discussing things with me, I've been able to watch how his ideas evolve over time — which has taught me that most good ideas have a long history and are seldom born overnight! This has been a great learning experience and has (along with many other qualities) made him an invaluable mentor. Thanks.

Dave Stevenson played a pivotal role in my early scientific training. When I was an undergraduate at Stanford, he invited me to work with him as a SURF, despite the fact that we'd never met and he knew almost nothing about me. That experience was important in my decision to pursue graduate studies at Caltech. In his roles as my academic and (other) research advisor, Dave has been very patient and wise. On many occasions my learning has been substantially accelerated by his amazing ability to coherently explain complex concepts — not to mention willingness to humor barrages of questions beyond the call of duty. Again, thanks.

Several younger folks have also acted as informal mentors. During my first couple of years, Jim Lyons and I had many engaging discussions about martian dust storms as well as more philosophical topics such as how to choose good research problems. Nilton Renno arrived just as my interest in terrestrial atmospheric dynamics and climate was building momentum. I clung to Nilton with white knuckles, hoping to sponge up every possible scrap of knowledge about convection in Earth's atmosphere. Our conversations shaped many of my current views on atmospheric convection and gave me a connection with atmospheric science which I hope to strengthen in the future. About the same time, Renu Malhotra initiated the collaboration that led to

my two summers in Houston, among my most memorable times at Caltech. She also gave me confidence that it's possible to bridge fields and wear several different hats. Finally, for the past year James Cho has provided immense help in getting me up to speed with the numerical shallow water code. He has answered numerous questions about numerics and helped teach me geophysical fluid dynamics. He has also been a good friend who has patiently listened to many updates on the soap opera that has been my social life these past couple of years (even though he never wanted to go hiking with me). I'm deeply indebted to all of you.

My friends have been an important part of my life at Caltech. Thanks to John Carri, Ushma, Jen, Bob, Lan, Cherie, and the dance crowd for making life richer and being my family away from home. Thanks to my high school and college friends Eric, Jeff, Joe, Waymond, Jaw, and Kari for great Christmas vacations and being there over the long haul. Ash and Sarah made department and conference life enjoyable and provided lots of computer help. With the occasional conversation at meetings and elsewhere, Don Banfield provided useful perspectives which made a difference during some rough spots. Thanks also to all the people up and down the hall, including Rob K., Alexey, Liz, Hui, Ulyana, Albert, and Anthony, who all made office life more fun. On the administrative side, Priscilla Piano was a great social advisor, Mike Black provided invaluable help with the computers, Kay, Irma, and Tammie helped things run more smoothly, and Tammie provided enough laughs to boil off stress.

My interactions with many other people also enriched my academic life. Thanks to Peter Goldreich for a class that was great fun to T.A., Yuk Yung for many interesting conversations about the interaction of chemistry and dynamics (as well as more philosophical topics), and Mike Brown for discussions about jovian lightning. Field trips led by Kerry Sieh, Bob Sharp, Lee Silver, Bruce Murray, Barclay Kamb, and Brian Wernicke were both enjoyable and educational. I also want to thank D. Hinson, P. Mahaffy, P.J. Gierasch, G. Schubert, R. Young, Paul Schenk, and W.B. McKinnon for useful discussions which contributed to the work presented here. D.H. Atkinson and A. Seiff graciously shared their preliminary data, and W.M. Folkner, R. Woo, H. Niemann, and the mass spectrometer team allowed us to present the data shown in

Fig. 2.1. Chapters 2, 4, and 5 are slightly modified texts of three *Icarus* articles (see the Overview). The copyright to these articles belongs to Academic Press, and the articles are reprinted here with permission.

Finally, I wish to thank my parents for their love and support over the years. I owe them for a great childhood filled with love, friends, and intellectual and creative fun. More recently, they have always been willing to listen and provide good advice during tough times, tried to make things easier however they could, and provided good companionship during my visits home.

Abstract

The low abundances of water and H_2S measured by the Galileo probe at Jupiter suggest that the probe entered a downdraft where dry air from above cloud top advects to 10 bars or deeper. I use basic physical constraints to extract dynamical information from three aspects of Galileo probe data. First, I suggest that to remain dry, the downdraft must be underlain by a stable layer which inhibits mixing of volatiles from below; this requires the downdraft to be mechanically forced. Second, on rapidly rotating planets, the Coriolis and centripetal forces caused by winds usually balance the horizontal pressure-gradient force (which gives information about horizontal density differences). Therefore, I use the known winds versus depth at the probe site to infer horizontal density differences between the probe site and its surroundings. Under reasonable assumptions, these densities are consistent with a downdraft at the probe site. Third, I use ideas of horizontal mixing and column stretching to explain how the observed vertical profiles of ammonia, H_2S, and water vapor can be produced in a downdraft. Finally, I discuss some apparent inconsistencies between these simple models. I also describe preliminary efforts to explore the origin, stability, and evolution of the downdrafts using the shallow water equations.

The differences between Ganymede and Callisto have led to speculation that Ganymede's history was shaped by tidal heating from an orbital resonance. Using the numerical model developed by Malhotra (1991, *Icarus* **94,** 399), I demonstrate that Io, Europa, and Ganymede could have passed through either of two (previously unexplored) Laplace-like resonances en route to the current Laplace resonance. Under reasonable conditions, these resonances produce great enough tidal heating in Ganymede to be geophysically significant. I also coupled the orbital evolution to an internal model of Ganymede to explore the effect of the resonance on Ganymede's interior. If Ganymede's tidal Q decreases strongly with temperature, the coupling can lead to massive, short-lived heating episodes which can melt much of the icy interior.

Such heat pulses require the initial ice temperature to be extremely cold ($< 200\,\mathrm{K}$), however, so they may be unlikely.

Contents

Chapter 1 Overview

This thesis consists of three papers and an additional chapter summarizing progress on my current research. The scope is broad: half of the work involves dynamics in Jupiter's atmosphere, while the other half comprises orbital and internal evolution of icy satellites. The particular topics are somewhat fortuitous, although my wide interests give me a propensity to take on many different projects. When I first arrived at Caltech in 1992, I was interested in planetary atmospheres and so I began discussions with Andy Ingersoll and Yuk Yung about possible research topics. This soon led to a proposition — and plans for a thesis — on martian dust storms using Mars Observer data (with Andy). Meanwhile, I liked Dave's breadth and research style, so I chose my second proposition with him on the icy moons of Jupiter. The demise of Mars Observer derailed my original thesis plans. Afterward, I contemplated theses on a variety of topics in both planetary science and terrestrial climate, using a variety of possible approaches ranging from laboratory geochemistry to dynamical modeling. In the end the possibility of new spacecraft data from Galileo proved irresistable. The unexpected dryness seen by the probe — while frustrating to cosmochemists — provided a fascinating new dynamics problem, and I set to work in attempt to explain probe data with the idea of a dry downdraft at the probe site. This led to the paper in Chapter 2, which has appeared as A.P. Showman and A.P. Ingersoll 1998, "Interpretation of Galileo probe data and implications for Jupiter's dry downdrafts," *Icarus* **132,** 205-220. In this paper, I addressed three problems raised by Galileo probe data in an attempt to construct a coherent model for conditions at the probe site. The ideas on gradient wind analysis of the probe winds, column stretching, isopycnal mixing, the relevance of the cloud data, and the distinction between the two scenarios were mine. The ideas on indirect circulations and energetics in Section 2 resulted from a set of collaborative discussions with Andy. All the calculations presented in the paper were done by me.

It still remains to determine whether the downdraft scenario is dynamically possible. Perhaps the most appropriate dynamical model is the shallow water model, which describes the evolution of a relatively dry weather layer overlying a deep, moist interior with fixed dynamics. In the model, a dry region — analogous to that seen by the probe — corresponds to a region where the interface between the layers bows downward. To explore the origin and evolution of the dry regions, I began collaborating with James Cho, who has extensive experience with pure 2D and shallow water codes. I summarize current progress on the project in Chapter 3.

The final two chapters of the thesis are the result of my Ganymede work. The substantial time delay between the disappearance of Mars Observer and my final choice of the jovian dynamics project provided an opportunity to carry the Ganymede work further than I had originally planned. After completing my Ganymede proposition, I began collaborating with Renu Malhotra at the Lunar and Planetary Institute, where I spent two productive summers. I constructed a model of Ganymede's interior which I coupled to Renu's orbital model; our goal was to determine whether the coupled system allows massive episodic heating in Ganymede. Our original plan was to assume the system passed through one of the Laplace-like resonances explored by Renu in 1991. While pursuing this study, however, I discovered the existence of two additional resonances which pump Ganymede's eccentricity to higher values than those seen by Renu in 1991. These new resonances require parameter values which are slightly different than those explored by Renu in 1991, which is why she did not see them. I performed many numerical simulations to characterize these resonances (without coupling to a Ganymede model), which culminated in the paper in Chapter 4. This paper has appeared as A.P. Showman and R. Malhotra 1997, "Tidal evolution into the Laplace resonance and the resurfacing of Ganymede," *Icarus* **127**, 93-111. (The *Icarus* paper includes an analytical calculation by Renu in an appendix. Because this is not my work, I have not included the appendix in the thesis.) The paper in Chapter 5 includes the coupled orbital and thermal simulations, along with my calculations of (1) the extent to which Ganymede would expand during a major heating episode and (2) the magnitude of lithospheric stress and cracking which is expected

from such expansions. This paper was published as A.P. Showman, D.J. Stevenson, and R. Malhotra 1997, "Coupled orbital and thermal evolution of Ganymede," *Icarus* **129,** 367-383.

Chapter 2

Interpretation of Galileo probe data and implications for Jupiter's dry downdrafts

Adam P. Showman

and

Andrew P. Ingersoll

Division of Geological and Planetary Sciences 150-21

California Institute of Technology

Pasadena, CA 91125

2.1 Abstract

The Galileo probe found the jovian abundance of H_2S to be 30% solar at the 8 bar level, while the abundance of water was less than 3% solar at 12 bars. From 8-20 bars, H_2S increased to three times solar, and water apparently increased as well. Since H_2S and water condense at 2 and 5 bars, respectively, the probe probably entered a dry downdraft wherein dry air above 2 bars is advected to 12 bars or deeper (Owen et al. 1996, Eos Spring Suppl., 77, S171). This is consistent with the fact that the probe entered the south edge of a 5-μm hot spot, a local region of Jupiter's atmosphere known from spectral modelling to be unusually low in cloud abundance (Orton et al. 1996, Science 272, 839).

We use basic physical constraints to address three problems raised by Galileo probe data. First, it is unclear how the hypothesized downdraft remains dry, since simple models of convection preclude dessication below the 2 and 5 bar condensation levels. We suggest that to suppress moist plumes from below, the downdraft must be of low density below 5 bars and hence thermally indirect, requiring mechanical forcing from other parts of the atmosphere. Second, if geostrophic balance holds, the Galileo probe winds imply that the hot spot (north of the probe site) contains a stable layer from 1-5 bars; this is inconsistent with a downwelling, since downwellings should be adiabatic below 2 bars due to the low radiative flux divergence. We show that when the centripetal acceleration of curving parcel trajectories is included in the force balance, however, a variety of density profiles is possible within the hot spot (depending on the radius of curvature of the winds). The most plausible profile implies that the hot spot is nearly dry adiabatic and that the equatorial zone south of the probe site is stable from 2-6 bars, suggesting moist adiabatic upwellings with a water abundance of 1-2 times solar. This is consistent with Galileo and Voyager images suggesting upwelling at the equator. The profile further implies that from 1-5 bars the hot spot is denser than the equatorial zone south of the probe site. Third, probe data indicate that NH_3 increased with depth below 1 bar and became constant by 8 bars, H_2S began increasing below 8 bars and levelled off by 16 bars, while water

only began increasing below 12 bars and was still increasing with depth at 20 bars. We propose that lateral mixing along isopycnals (surfaces of constant potential density) could produce the observed pattern; alternatively, the downwelling might consist of column stretching, so that the NH_3, NH_4SH and water lifting condensation levels were pushed to 8, 16 and > 20 bars, respectively. In either case, the simplest form of this model requires the downdraft to be less dense than the surroundings from 0.5 to 20 bars. In its simplest form, this model is therefore incompatible with our favored interpretation of the winds; more detailed studies will be necessary to resolve the problem.

2.2 Introduction

The Galileo probe took *in situ* measurements of Jupiter's atmosphere from the 0.4 bar level, near the visible cloud tops, to the 20 bar level, 150 km deeper. Among the measurements came the surprising result that the H_2S mole fraction at the 8-bar level was 1×10^{-5}, while the water vapor mole fraction at 12 bars was 6×10^{-5} or less (Niemann et al. 1996, 1998; Atreya 1996). These values are roughly 30% and $< 3\%$ of "solar" abundance, defined as solar S/H and O/H mixtures with the sulfur and oxygen speciated into H_2S and H_2O, as expected for Jupiter's atmosphere. These results are puzzling because Jupiter probably formed from a reservoir with solar or greater S/H and O/H (Gautier and Owen 1989); further, between 8 and 16 bars, H_2S surged from 0.3 to 2.7 times solar, and water also apparently increased by an order of magnitude between 12 and 20 bars (although the absolute water abundance is still uncertain at depth; Niemann et al. 1998, Mahaffy 1996). Global depletion of these volatile species is therefore ruled out. Condensation cannot explain the low abundances at 8 bars, because H_2S and water only condense above 2 and 5 bars, respectively, when abundances are near solar (Weidenschilling and Lewis 1973). The probe therefore apparently fell into a dry downdraft, a region where dry air from above cloud top is advected to 12 bars or deeper, producing locally dessicated conditions to those depths (Owen et al. 1996, Atreya 1996). Young (1998) summarizes the probe results.

The idea of a downdraft is consistent with the fact that the probe entered the south edge of a 5-μm "hot spot," a local region in Jupiter's north equatorial belt which has unusually high 5-μm emission (Orton et al. 1996, 1998). The high emission emanates from deep levels, suggesting that these $10^3 - 10^4$ km-sized spots are severely depleted in both cloud abundance (Carlson et al. 1994) and water and ammonia vapor (Carlson et al. 1996, Roos-Serote et al. 1998, Drossart et al. 1998). Further, hot spots reside within belts, where modeling of Voyager thermal data predicts downwelling (Gierasch et al. 1986, West et al. 1992). Thus, the idea that downwelling occurs within hot spots is reasonable.

However, there are problems reconciling the downdraft hypothesis with other data and basic physical constraints. In this paper, we propose solutions to three problems raised by Galileo probe data.

In Section 2.3, we consider the first problem: How do we keep the downdraft dry to 20 bars? Simple models of convection suggest that downdrafts are denser than updrafts. If so, moist plumes rising from Jupiter's interior should be buoyant within the downdraft, and should quickly mix H_2S and water vapor up to the condensation levels at 2 and 5 bars. In order for the downdraft to remain dry, upward transport of moist plumes must be suppressed. The subsiding air must therefore be underlain by a stable layer, and must be *less dense* than the surroundings. This implies that the circulation is thermally indirect (updrafts denser than downdrafts). Such circulations increase the atmosphere's potential energy; we show that this increase can be driven either by loss of kinetic energy or by a flux of geopotential energy from another part of the atmosphere. We describe several mechanisms for creating the low density air. Indirect circulations have already been proposed to exist above the ammonia cloud tops on Jupiter (Gierasch et al. 1986), and are important on Earth.

The second problem, considered in Section 2.4, is explaining the probe winds. The probe measured eastward winds of $90\,\mathrm{m\,s^{-1}}$ at cloud top, increasing to $180\,\mathrm{m\,s^{-1}}$ at 5 bars, then decreasing slightly to $170\,\mathrm{m\,s^{-1}}$ at 20 bars (Atkinson et al. 1996, 1997). Because of Jupiter's high rotation rate and large size, atmospheric features are normally thought to be in geostrophic balance, a balance between pressure-gradient and

Coriolis forces. When combined with hydrostatic balance, the well-known "thermal wind" relation results (Holton 1992, p. 73). This equation relates the vertical wind profile to the latitudinal gradient of density with depth at the probe site. The fact that $\partial u/\partial p > 0$ from 1-5 bars implies that over this pressure range the hot spot (north of the probe site) is less dense than the equatorial zone (south of the probe site); further, the slightly decreasing winds from 5 to 20 bars suggest that the hot spot is marginally denser than the equatorial zone in that layer. The hot spot is therefore statically stable from 1 to 5 bars. This is difficult to reconcile with downwelling in the hot spot, because subsiding regions should be dry adiabatic below 2 bars, where the net radiative flux divergence is low (Sromovsky et al. 1996, 1998; Hunten et al. 1980).

To resolve this problem, we show that geostrophic balance may not hold. At the probe site's equatorial latitude of 6.5°N, the Coriolis force is relatively weak and the centripetal force due to curving wind trajectories becomes important. This invalidates the thermal wind equation. Using a generalization of the equation valid for gradient wind balance (a balance between pressure-gradient, Coriolis, and centripetal forces), we calculate possible vertical profiles of the latitudinal density gradient. The profiles depend on the local radius of curvature of the winds, which is poorly known. For certain values of the radius of curvature, the hot spot is denser than the equatorial zone in the 1-5 bar layer, but is less dense than the equatorial zone in the 5-12 bar layer. These gradients therefore predict a stable layer from 1-5 bars *south* of the probe site, where modelling of Voyager data suggests upwelling (Gierasch et al. 1986), and allow the hot spot to be dry adiabatic below 2 bars, consistent with a downwelling. This resolves the problem.

In Section 2.5 we attack another vexing observation, shown in Fig. 2.1: that NH_3 increased rapidly below 1 bar, reaching a plateau below 8 bars (Folkner et al. 1998); H_2S began increasing below 8 bars and tentatively levelled off by 16 bars; while water only began increasing below 12 bars and was still increasing with depth at 20 bars (Niemann et al. 1998). This pattern mimics that predicted by equilibrium condensation models (Weidenschilling and Lewis 1973) but occurs at much greater

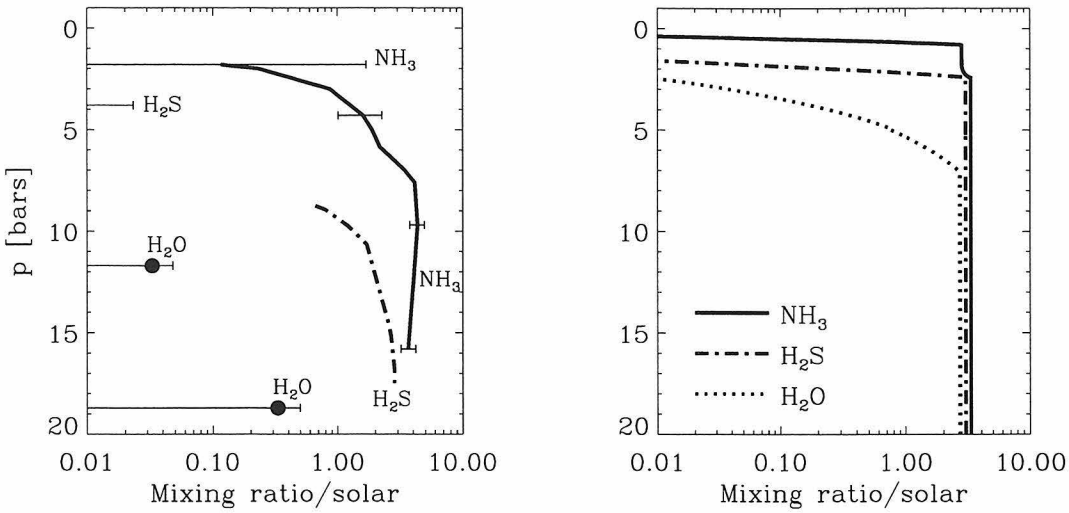

Figure 2.1: (Left) Abundances of NH_3, H_2S, and H_2O vs. pressure as measured by the Galileo probe. The NH_3 profile (thick solid line) is from Folkner et al. (1998), while the H_2S data (thick dash-dot line) and H_2O data (filled circles) are from Niemann et al. (1998). The filled circles represent actual detections of H_2O which are upper limits because of the possibility of outgassing from the equipment; the upper limit on H_2S at 3.8 bars is a non-detection. All data are preliminary and may be revised in the future. (Right) Profiles of NH_3 (solid line), H_2S (dash-dot line), and H_2O (dotted line) as predicted from an equilibrium condensation model, assuming deep abundances near 3 times solar. Comparison with the model shows that the observed increases with pressure cannot be caused by condensation. If they were caused by mixing from below, however, one would expect the mixing ratios of the three gases to increase together. The observed behavior is therefore puzzling.

pressures. Lateral mixing has been proposed by Atreya et al. (1997) to account for the observed pattern. However, this requires material to descend by $\sim 50 - 100$ km as it mixes from the surroundings into the probe site. We assume such mixing takes place on isopycnals (surfaces of constant potential density) and explore the implications. This provides a natural explanation for why horizontal mixing does not moisten the downdraft, despite the vigorous horizontal motions observed in Jupiter's atmosphere. We also offer an alternate hypothesis to explain the data in Fig. 2.1: that the downdraft consists simply of stretching of the air column, with no mixing.

In Section 2.6, we return to the question of forcing posed in Section 2.3. Armed with constraints on the hot spot's density versus depth developed in Sections 2.4 and 2.5, we consider the following question: Can the atmospheric heat engine supply enough energy to push dry air to 10-20 bars, as observed? The data tentatively suggest that the atmospheric circulation *is* energetic enough to push dry air to 10-30 bars, and possibly much deeper. This provides a consistency check that the postulated indirect circulation is energetically reasonable. However, we do not provide a detailed mechanism.

In Section 2.7 we summarize our results and discuss an apparent inconsistency between our favored interpretations of the wind and mass spectrometer data.

2.3 Puzzle I: Keeping the downdraft dry

For the downdraft to be dry, it must be underlain by a stable layer, so that moist plumes rising from below are suppressed. If the density is independent of horizontal position in the deep atmosphere, this implies that (just above the stable layer) the descending air is less dense than the upwellings at the same pressure.

There are two important questions we must tackle to understand this anomalous situation. First, what mechanisms exist for creating the low density air? These mechanisms will determine how high (above the stable layer) the low density air extends. Second, what sort of forcing is required to make such air descend? In this section we propose possible answers. Because of the paucity of data, our aim is more

to clarify the possibilities rather than espouse any particular model. We also discuss examples of indirect circulations on Earth. Finally, we compare our model to other hypotheses which have been proposed for explaining the dryness at the probe site.

2.3.1 Creating the low density air

Figure 2.2 schematically shows mechanisms for creating a low density downdraft, by qualitatively depicting two possible thermodynamic paths followed by air which rises in the region surrounding the hot spot and descends in the hot spot. The left panel depicts a cartoon of the proposed circulation, while (a) and (b) show the two scenarios. In (a) and (b), the horizontal axis is virtual temperature, defined as $T_v = Tm_d/m$, where T is temperature, m_d is the mass per molecule of "dry" air (free of ammonia, H_2S, and water), and m is the mass per molecule of the mixture. Virtual temperature measures density at a given pressure: high T_v implies low density and vice versa. Both scenarios assume a homogenous deep atmosphere containing roughly solar water. The deep atmosphere extends in some regions up to the water condensation level near 5 bars, where it produces cloudiness and upwelling. Above the condensation level ($p < 5$ bars), these upwellings follow a moist adiabat; most of the condensate is assumed to rain out. The moist adiabats have smaller $|\partial T_v/\partial z|$ than a dry adiabat because of the warming and decrease of molecular mass associated with condensation and rainout; such regions are termed "statically stable." In the first scenario (a), the radiative equilibrium temperature is less than the air temperature near the ammonia cloud top. The dry downwellings therefore *cool* by radiation at $p < 2$ bar (becoming denser than the upwelling), and follow a dry adiabat below 2 bars. However, they cool insufficiently to become denser than the upwellings (and deep atmosphere) *below* the water condensation level; therefore, they are less dense than the surroundings from 5 bars to the bottom of the downdraft. If the radiative cooling is great enough, the downwelling column (averaged from 0.5 bars to the bottom of the downdraft) may be denser than the upwelling column. This would provide a natural mechanism for driving the downdraft; on average, the circulation would be thermally direct

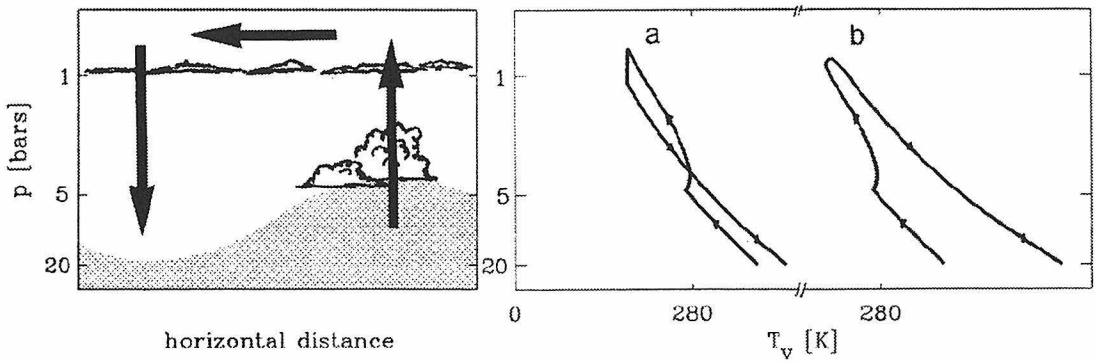

Figure 2.2: A model to explain the dryness at the probe site. (Left) A schematic of our proposed circulation; arrows denote air motion and the stippled region indicates air with high water vapor content. (Right) Two possible thermodynamic paths followed by air rising in the regions surrounding the hot spot and descending in the hot spot. The plots have the same vertical axis; the horizontal axis for the thermodynamic paths is virtual temperature. (a) Updrafts follow a moist adiabat above the 5 bar water condensation level; downdrafts *cool* by radiation above 2 bars and follow a dry adiabat below. Downdraft is less dense at $p > 5$ bars. (b) Updrafts follow a moist adiabat, but radiatively *warm* in upper troposphere. Downwellings follow dry adiabat. Downdrafts are less dense for $p > 0.5$ bars. Both models produce a deep stable layer which suppresses the mixing of volatiles into the downdraft. The difference between the moist and dry adiabats has been exaggerated for clarity.

(downdrafts denser than updrafts).

The radiative equilibrium temperature is poorly known, however, and could be greater than the upwelling air temperature above 0.5 bars. In that case, as shown in (b), radiative *warming* occurs above 0.5 bars as the air rises. (Because net radiative cooling to space occurs at all latitudes on Jupiter, this warming must be accompanied by radiative cooling elsewhere within the column. For example, if the updrafts in Fig. 2.2b occur in thunderstorms, some of the downdraft air could cool radiatively while subsiding between thunderstorms. The remainder would ascend, warm radiatively [a result of having cooled adiabatically to temperatures below the radiative equilibrium temperature], and descend in the hot spot. Only the latter thermodynamic path is depicted in Fig. 2.2b.) When the air descends it is therefore warmer

than the upwelling. In this scenario, the updrafts are denser than the dry downdrafts at all heights below ~ 0.5 bars. Gierasch et al. (1986) proposed an analogous mechanism to account for the upper tropospheric belt-zone temperature difference and cloud patterns: upwelling occurs in the (cold) zones and downwelling in the (warm) belts.

A third scenario exists. If the descent time from the tropopause to a few bars is much less than the radiative time (a few years), minimal radiative cooling or warming would occur. The downdraft and updraft would be of comparable density above a few bars, but the downdraft would be less dense at deeper levels. This scenario can be considered a special case of (b).

The two scenarios have one feature in common: the difference in virtual temperature between the downdrafts and updrafts increases with depth from ~ 2 to 6 bars. (For example, in (a), $T_{v,\,\mathrm{down}} - T_{v,\,\mathrm{up}}$ is negative at low pressures, crosses through zero near 5 bars, and becomes positive at $p > 5$ bars.) This feature will aid our interpretation of the probe winds in Section 2.4.

2.3.2 Forcing the dry air downward

Atmospheric convection operates as a heat engine, converting potential energy into kinetic energy by pressure forces acting on buoyant updrafts and dense downdrafts. When high density air rises and low density air sinks, as in the present case, potential energy is increased; this increase in potential energy occurs either by destruction of kinetic energy or by work done by pressure forces created elsewhere in the atmosphere. To quantify this energetic cycle, consider the hydrostatic atmospheric kinetic energy equation from Haltiner and Williams (1980, p. 20)

$$\frac{\partial K}{\partial t} + \nabla \cdot [\mathbf{v}(K + \Phi)] + \frac{\partial}{\partial p}[\omega(K + \Phi)] = -\frac{\omega}{\rho} + \mathbf{v} \cdot \mathbf{F} \tag{2.1}$$

where $K = \mathbf{v} \cdot \mathbf{v}/2$ is atmospheric kinetic energy per mass, $\mathbf{v}$ is the horizontal wind, $\omega = dp/dt$ is the vertical velocity in pressure coordinates, Φ is geopotential, ρ is density, p is pressure, $\mathbf{F}$ is the frictional drag force, and $\nabla = (\partial/\partial x, \partial/\partial y)$. The term

$-\omega/\rho$ represents conversion of potential energy into kinetic energy by pressure forces. (This conversion can be seen by considering the hydrostatic enthalpy equation from Haltiner and Williams:

$$\frac{\partial H}{\partial t} + \nabla \cdot (\mathbf{v}H) + \frac{\partial(\omega H)}{\partial p} = \frac{\omega}{\rho} + Q \tag{2.2}$$

where H is enthalpy per mass and Q is heating by radiation, conduction, and viscous dissipation of kinetic energy.) Returning to the kinetic energy equation, we average in the horizontal over a local area around the indirect circulation and integrate over mass from a lower pressure p_{bot} (below the bottom of the dry downdraft) to an upper pressure p_{top} of 270 mbar, near the tropopause. Rearranging, the equation becomes

$$\int \frac{1}{\rho}\frac{dp}{dt}\, dm = -\int \dot{K}\, dm - \int \left(\frac{1}{A}\int_{\text{sides}} (K+\Phi)\mathbf{v}\cdot\mathbf{n}\, dl\right) dm$$

$$-\frac{1}{g}\left[\omega(K+\Phi)\right]_{\text{top}} + \frac{1}{g}\left[\omega(K+\Phi)\right]_{\text{bottom}} - D \tag{2.3}$$

where D is the dissipated power per area in the volume, $\mathbf{n}$ is the outward normal vector, and A is the horizontal area of the domain. The integration element dm is mass per area and dl is distance (along an isobar) around the sides of the volume. The left side of the equation is a measure of the change in gravitational (and internal) energy brought about by atmospheric motion. It is the difference between the power stored in the thermally indirect parts of the circulation and that released in the thermally direct parts (it is positive if thermally indirect circulations dominate and negative if direct ones dominate).

The equation states that creation of column integrated enthalpy by atmospheric motion (as would occur in an indirect circulation) is balanced by importation of kinetic and geopotential energy into the volume minus the power per area lost to dissipation or stored as kinetic energy. In steady state, therefore, the indirect circulation can be forced by importation of either kinetic or geopotential energy through the boundaries. In the former case, the imported kinetic energy is created by pressure forces elsewhere

in the fluid; in the latter case, these pressure forces do work directly on the indirect circulation without any intermediate generation of kinetic energy. If the downwelling column is denser than the upwelling column (as could be the case in Fig. 2.2a), the net circulation is thermally direct, doing work on the environment. In this case, the thermally indirect motion below 5 bars is driven by geopotential energy flux (through the 5 bar surface) from the overlying direct motion.

The best example of an indirect circulation powered by importation of geopotential energy is the lower stratospheric circulation on Earth. The upwelling air at the equator cools so much by adiabatic expansion that it becomes colder than the subsiding air at higher latitudes; this atmospheric motion creates enthalpy, which is destroyed by radiation (Tomatsu 1979). Near the tropopause, the isobars bow upward where upwelling occurs and downward where downwelling occurs. This leads to importation of geopotential energy across the 150 mbar surface at a rate of $0.3\,\mathrm{W\,m^{-2}}$ (Tomatsu 1979). Simple scaling suggests that the kinetic energy flux is considerably smaller. In geostrophic balance, the ratio of kinetic to geopotential energy flux is $\Delta K/\Delta\Phi \approx u^2/fuL \approx u/fL \approx 0.1$, where u is a typical wind speed at the tropopause, L is a characteristic length (a few 1000 km), and f is the Coriolis parameter.

Gierasch et al. (1986) have proposed an analogous circulation above 0.5 bars on Jupiter. We can estimate the boundary terms for the jovian circulation using vertical velocities from Gierasch et al. (1986) and West et al. (1992). The zonal jets have typical speeds of $40\,\mathrm{m\,s^{-1}}$, which in geostrophic balance implies that the difference in geopotential energy (along isobars) between belts and zones is $3 \times 10^4\,\mathrm{m^2\,s^{-2}}$ (at 30° latitude, assuming the belt-zone spacing is 5000 km). Retrieved vertical velocities, of order $\omega = 6 \times 10^{-5}\,\mathrm{Pa\,s^{-1}}$ at 270 mbar, suggest that upwelling occurs in regions of high Φ and downwelling in regions of low Φ; the resultant geopotential energy flux is $\sim 0.08\,\mathrm{W\,m^{-2}}$. In contrast, the mean kinetic energy is $\sim 2 \times 10^3\,\mathrm{m^2\,s^2}$, implying a flux of order $\sim 0.005\,\mathrm{W\,m^{-2}}$. At the probe site's latitude of 6.5°N, the calculation gives geopotential and kinetic energy fluxes of $0.05\,\mathrm{W\,m^{-2}}$ and $0.02\,\mathrm{W\,m^{-2}}$ (using $u = 100\,\mathrm{m\,s^{-1}}$), although the assumption of geostrophic balance is less likely to hold since the Rossby number is about 0.5.

2.3.3 Comparison of our model with other proposed models

Two other proposed scenarios exist for depletion of volatiles and clouds at the probe site down to 20 bars. Guillot (1996, 1995) suggested that convection is inhibited at depths where water vapor (hence molecular mass) rises with pressure, and that the low volatiles measured by the probe might be a globally widespread condition. He hypothesized that the internal heat is transported upward by radiation or diffusive (oscillatory) convection (Turner 1973). We differ from Guillot's viewpoint in two respects. First, in the absence of a downdraft, small scale mixing should transport volatiles upward across the stable layer to the condensation level. We feel that a downdraft is needed to counteract this mixing. Compensating updrafts must exist elsewhere; volatiles would not be depleted in those regions. Second, temperature differences between these (large-scale) updrafts and downdrafts could transport heat — we need not require radiation or diffusive convection to deliver the entire heat flux.

Engel et al. (1996) hypothesized that rapid subsidence inhibits upward transport of water vapor from Jupiter's interior. They used a height and time dependent cloud model to calculate cloud densities as a function of the imposed large-scale subsidence rate; upward mixing of water was modelled as a diffusive process, with a diffusivity calculated from mixing length arguments. With no subsidence, the model produced clouds much thicker than those observed by Galileo; a subsidence rate of $1 - 2\,\mathrm{m\,s^{-1}}$ was needed to keep the model dry and free of clouds. (This velocity matches that predicted by mixing length theory for Jupiter.) The resultant downwelling time from the tropopause to the 10-bar level is about one day. This subsidence rate is fast enough to preclude radiative cooling of the downdraft.

In contrast to Engel et al., we suggest that dryness at the probe site is maintained by a deep stable layer which inhibits convection from below. In absence of subsidence, the stable layer will rise as volatiles are mixed upwards by turbulence below the layer; subsidence is therefore still necessary to maintain the position of the stable layer in steady state. The required descent time is quite long, however, and is consistent with the radiative time constant. We can calculate the required subsidence rate as follows.

Suppose that convective plumes from the deep atmosphere overshoot into the stable layer, entraining a small amount of the low density air into the deep atmosphere. This process produces potential energy, which derives from the kinetic energy of the overshooting plumes. Assume the power per area provided by the kinetic energy is $P_{\rm conv}$. If a mass per area dp/g of low density air is mixed down a distance h below the stable layer over a time dt, then the increase in potential energy per area is

$$\frac{\Delta T_v}{T_v}\frac{dp}{g}gh \sim P_{\rm conv}dt$$

where ΔT_v is the virtual temperature stability of the layer (relative to a dry adiabat) and T_v is the virtual temperature. The stable layer therefore migrates upward at a velocity (in pressure coordinates) of dp/dt given by

$$\frac{dp}{dt} = \frac{P_{\rm conv}T_v}{\Delta T_v h}$$

The dry air must therefore subside at this rate for the position of the stable layer to be maintained. We estimate $P_{\rm conv}$ as follows. The internal heat flux at the equator is about $5\,{\rm W\,m^{-2}}$ (Ingersoll and Porco 1978). If the entire heat flux is convected and if we assume the convective motions are 20% efficient in producing kinetic energy (as would be expected from heat engine arguments if convection occurs over a scale height), then $P_{\rm conv} = 1\,{\rm W\,m^{-2}}$. We use $\Delta T_v = 4\,{\rm K}$, comparable to the expected difference in virtual temperature between the upper troposphere and deep atmosphere for solar water abundance. Using $T_v = 400\,{\rm K}$ and $h = 60\,{\rm km}$ (one scale height), we obtain a subsidence rate of $2 \times 10^{-3}\,{\rm Pa\,s^{-1}}$ necessary to keep the downdraft dry. The resulting descent time from the tropopause to 10 bars is 20 years. Even if we take $P_{\rm conv} = 5\,{\rm W\,m^{-2}}$, the descent time is 4 years, still long enough to allow radiative cooling of the downdraft.

The trade-wind inversion on Earth is maintained by processes similar to those suggested here (Betts 1973, Emanuel 1994). Because of the strong inversion, subsidence speeds of $0.005\,{\rm m\,s^{-1}}$ are sufficient to balance upward mixing of boundary layer air, despite the fact that boundary layer plumes *below* the inversion move at vertical

speeds up to $1\,\mathrm{m\,s^{-1}}$ (e.g., Garratt 1992, p. 214).

2.4 Puzzle II: The probe winds

The winds obtained by Doppler tracking of the Galileo probe signal from the orbiter are shown in Fig. 2.3 (Atkinson et al. 1996, 1997). The preferred fit to the data yields zonal winds which are $90\,\mathrm{m\,s^{-1}}$ at the 0.5 bar ammonia cloud level, increasing to $180\,\mathrm{m\,s^{-1}}$ at 5 bars and decreasing to $170\,\mathrm{m\,s^{-1}}$ below 15 bars. The 1-σ uncertainty is roughly $10\,\mathrm{m\,s^{-1}}$, so the decrease in speed from 5 to 15 bars is valid to about 1-σ. The increase in winds from 0.5-5 bars appears robust, and agrees with the winds obtained by Doppler tracking of the probe signal from the ground (Folkner et al. 1996). Further support for the winds is provided by probe acceleration data (Seiff et al. 1997a).

As described in the Introduction, these wind data are difficult to understand if geostrophic balance holds. When geostrophic and hydrostatic balance are combined, the well-known "thermal wind" relation results (Holton 1992, p. 73):

$$\left(\frac{\partial T_v}{\partial y}\right)_p = \frac{pfm_d}{k}\left(\frac{\partial u}{\partial p}\right)_y \tag{2.4}$$

where T_v is virtual temperature, y is distance northward, p is pressure, m_d is the mass per molecule of "dry" air (free of ammonia, H_2S, and water), k is Boltzmann's constant, u is the zonal wind, $f = 2\Omega \sin\phi$ is the Coriolis parameter, Ω is the planetary rotation rate, and ϕ is latitude. The fact that $\partial u/\partial p > 0$ from 1-5 bars implies a stable layer in the hot spot in that layer, which seems inconsistent with a downwelling. However, at the probe's equatorial latitude of 6.5°N, the Coriolis force is relatively weak and the centripetal force due to curving flow trajectories becomes important. The thermal wind equation may therefore not hold, and another force balance must be used. In this section, we use the more general "gradient wind" force balance, a balance between pressure-gradient, Coriolis, and centripetal accelerations. We derive a range of possible vertical profiles of density in the hot spot as compared to that in

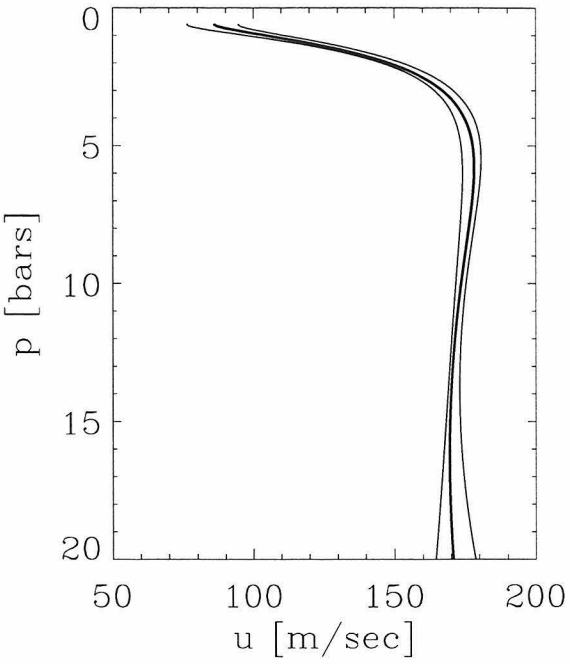

Figure 2.3: Winds versus depth measured by Doppler tracking of Galileo probe signal from the orbiter (from Atkinson et al. 1997). Thick curve is nominal fit to data; thin curves denote the 1-σ error envelope.

the equatorial zone. The profiles are not unique because the new relation contains one poorly known parameter, the local radius of curvature of the winds at the probe site. (The profile obtained from geostrophic balance will be one such profile.) We then discuss the plausibility of each profile.

The gradient wind force balance in the meridional direction is

$$\frac{u^2}{R} + fu + \frac{\partial \Phi}{\partial y} = 0 \tag{2.5}$$

where R is the local radius of curvature of the wind trajectory (positive for trajectories curving to the left and negative for those curving to the right) and $\partial\Phi/\partial y$ is the gradient of geopotential Φ with northward distance y. (This equation holds for curving flow at the point where the flow is zonal.) Differentiating this equation with respect to pressure and using hydrostatic balance, we obtain the gradient-wind generalization of the thermal wind relation:

$$\left(\frac{\partial T_v}{\partial y}\right)_p = \frac{p m_d}{k}\frac{\partial u}{\partial p}\left(\frac{2u}{R} + f\right) \tag{2.6}$$

No high resolution images exist for the probe entry hot spot, so R is unknown. We treat it as a free parameter. Galileo images of a different hot spot, however, show a large clockwise circulation southeast of the hot spot (Vasavada et al. 1998). These images suggest that negative (clockwise) values of R may be most appropriate.

When we substitute the known winds (Atkinson et al. 1996, 1997) into the equation using many values of R, we find that three types of $\partial T_v/\partial y$ profile exist. Examples of each are displayed in Fig. 2.4 (top row, panels a-c). The solid lines in the top panels result from using Atkinson et al.'s nominal wind profile (thick line in Fig. 2.3). To determine the approximate error in the $\partial T_v/\partial y$ curves, we constructed many hypothetical wind profiles which deviated from the nominal profile, yet still passed within the error envelope of the winds. The deviations were assumed to have a vertical wavelength of a few bars. The error bars in Fig. 2.4 (top row) delineate the range of $\partial T_v/\partial y$ values obtained from these hypothetical wind profiles. The profiles end at 12 bars because, at $p > 12$ bars, the uncertainty in $\partial T_v/\partial y$ becomes much

greater than the mean value (this results directly from the increasing error in the winds from 12 to 20 bars; see Fig. 2.3).

The densities can also be expressed using the virtual potential temperature, defined as (Salby 1996, p. 124)

$$\theta_v \equiv T_v \left(\frac{p_0}{p} \right)^{\frac{\gamma-1}{\gamma}} \tag{2.7}$$

where $p_0 = 1$ bar is a reference pressure and $\gamma = c_p/c_v$ is the ratio of specific heats at constant pressure and volume. Virtual potential temperature (which is equivalent to potential density) is more convenient than virtual temperature for expressing height variations of density because it accounts for the compressibility of air. When θ_v is constant with pressure, the profile is statically neutral to dry convection; when θ_v increases with height, the profile is stable to dry convection, and when θ_v decreases with height, the profile is unstable to dry convection.

The bottom row of Fig. 2.4 (panels d-f) shows the density profiles 2000 km north of the probe site, at the probe site, and 2000 km south of the probe site obtained by linearly extrapolating the dashed-dot profiles of $\partial T_v/\partial y$ plotted in the top row. The densities are expressed using virtual potential temperature. The dashed-dot profiles in panels (a)-(c) (top row) were chosen so that $\partial\theta_v/\partial y$ is independent of p wherever possible. When $\partial\theta_v/\partial y$ decreases with pressure ($\partial^2\theta_v/\partial y\partial p < 0$), the region south of the probe site must be taken as neutrally stable; the extrapolation is carried out toward the north, and all such regions contain some stability. (If we took the probe site or region to the north as neutrally stable, our extrapolation would force some regions to the south to be statically unstable, which is impossible.) When $\partial\theta_v/\partial y$ increases with pressure ($\partial^2\theta_v/\partial y\partial p > 0$), however, the region to the north is taken as neutrally stable, and the extrapolation is carried out toward the south. When $\partial^2\theta_v/\partial y\partial p$ changes sign, the region pinned to an adiabat switches from north to south of the probe site. The nominal $\partial T_v/\partial y$ profile (solid curve in panels (a)-(c)) requires several such switchings, leading to complicated interpretation. Most of the switchings, however, result from subtle variations in the nominal $u(p)$ which are far

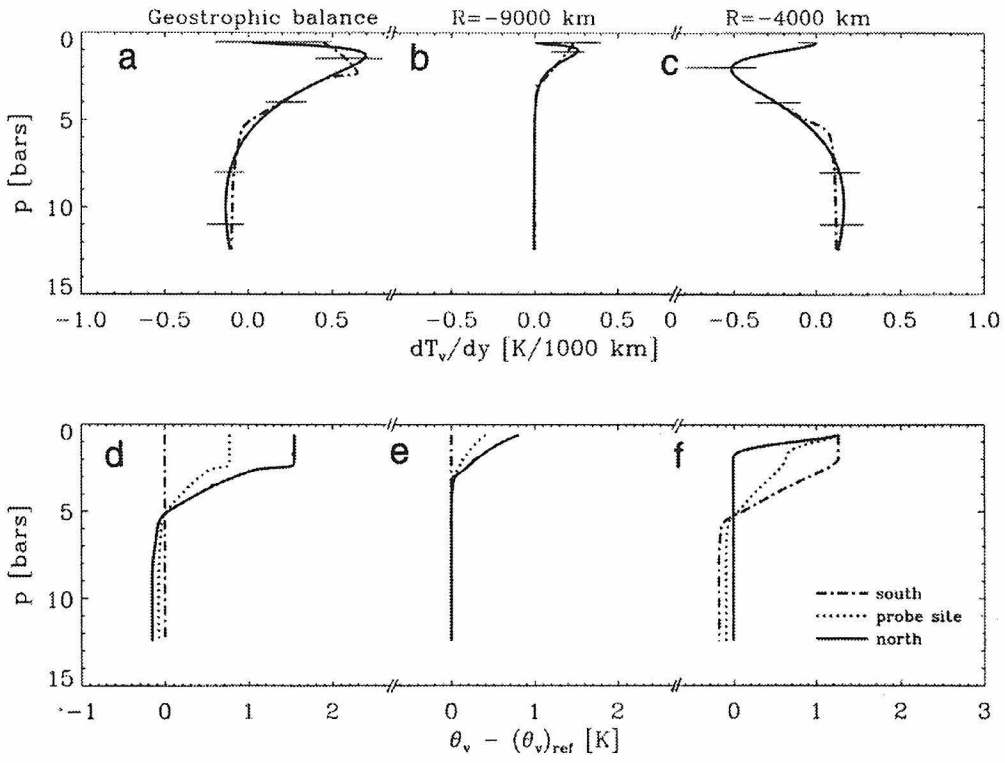

Figure 2.4: Top row: Profiles of $\partial T_v/\partial y$ versus pressure obtained from the winds assuming gradient wind balance, for three cases: (a) geostrophic balance ($R \to \pm\infty$), (b) $R = -9000$ km, and (c) $R = -4000$ km. Bottom row: θ_v versus pressure obtained by linearly extrapolating the $\partial T_v/\partial y$ profiles (from the top row) 2000 km north and south of the probe site. (The θ_v profiles are plotted relative to a reference θ_v profile which is constant with height.) Based on simple models of convection, the cases in the leftmost and middle columns are difficult to understand, but the rightmost makes sense. It is qualitatively similar to Fig. 2.2a.

below the error bars; hence, these switchings contain no information. By using the dashed-dot curves where $\partial\theta_v/\partial y$ is independent of pressure wherever possible, we limit the number of switchings to those *required* by the data.

Consider the first type of profile, shown on the left for geostrophic balance ($R \to \pm\infty$); qualitatively similar profiles hold for negative (clockwise) values of R exceeding 12,000 km in magnitude or for any positive (counterclockwise) value of R. Here, $\partial T_v/\partial y$ is positive from 1-5 bars and (marginally) negative from 5-12 bars. This implies that the hot spot (to the north of the probe site) is *less dense* (greater T_v) from 1-5 bars than the equatorial zone (south of the probe site). The hot spot is denser than the equatorial zone below 5 bars, however. This is seen in the virtual potential temperature profiles in Fig. 2.4d; the profiles were constructed by assuming the region to the south is dry adiabatic (i.e., neutrally stable). (We could have chosen the region to the south to be stable, in which case the hot spot would be even more stable. Similarly, if we chose the hot spot or the probe site to be neutral, the region to the south would be unstable to dry convection, which is impossible. Fig. 2.4d shows the *minimum* stability inside the hot spot and at the probe site consistent with the physical requirement that no region within 2000 km of the probe site be unstable. This is probably an appropriate distance to use because it is comparable to the size of atmospheric features, and therefore to the maximum range over which $\partial T_v/\partial y$ can be reliably extrapolated.) The region to the north shows a strong stable layer from 2-5 bars (θ_v decreasing with depth). This results directly from the fact that $\partial u/\partial p$ decreases strongly from 1 to 5 bars, which is a robust feature in the wind data. The greater density in the hot spot below 5 bars results from the decrease in wind speed from 5-12 bars, and is therefore robust to about 1-σ.

The results in Fig. 2.4d violate our expectations. First, because of the low radiative flux divergence below 2 bars (Sromovsky et al. 1996, 1998), downwellings should follow dry adiabats there. Although a stable layer above 5 bars can result from moist convective upwelling with a solar water abundance, this is not consistent with downwelling in the hot spot. Second, because Voyager data suggest upwelling near the equator (Gierasch et al. 1986), we might expect the region south of the probe

site to contain a stable layer resulting from moist upwelling. However, the region south of the probe site is less stable than the probe site itself (Fig. 2.4d), which is nearly dry adiabatic (Seiff et al. 1997b); the equatorial zone region south of the probe site must therefore be even closer to dry adiabatic. The inferred profiles are difficult to understand because they predict that the virtual temperature between downdrafts and updrafts decreases with depth, contrary to expectation. Third, the dry downwelling should be less dense below 5 bars, while Fig. 2.4d suggests the reverse. Therefore, while the geostrophic case plotted in Fig. 2.4a and d is consistent with the winds, it cannot be reconciled with our expectations about how and where convection occurs.

Consider instead the second type of profile, shown in the middle column of Fig. 2.4 for $R = -9000\,\mathrm{km}$, and valid for any negative R (clockwise trajectory) with magnitude between 8000 and 12,000 km. This profile suggests that $\partial T_v/\partial y$ is positive from 0.5-3 bars and zero below 3 bars. Profiles north and south of the probe site therefore have equal densities (along isobars) below 3 bars, but above 3 bars the hot spot is less dense. The hot spot is therefore *stable* above 3 bars (Fig. 2.4e). (Below 3-4 bars, the virtual temperature gradient is zero because the pressure-gradient force has dropped out; the resultant balance — inertial balance — is between Coriolis and centripetal forces. For a given R, such balance occurs only for a particular value of u. Inertial balance approximately holds at all heights below 3 bars because the winds vary only slightly with depth there.) Although possible, this scenario is also difficult to reconcile with simple convection models. The stable layer cannot result from moist convective upwelling since water can only produce significant stable layers near 5 bars; the stability resulting from H_2S condensation is too small to match that required here. Radiative cooling and subsidence could produce a stable layer. This qualitatively matches the net flux radiometer observations that substantial cooling occurs at pressures less than 2-3 bars, with little cooling at greater pressures (Sromovsky et al. 1996, 1998). However, Fig. 2.4e suggests that the stability in the hot spot equals that in the equatorial zone at $p > 3$ bars. If the equatorial zone were an upwelling, it should be stable from 2-6 bars (Fig. 2.2). The hot spot would then also

contain a stable layer from 2-6 bars, which is difficult to understand.

The third scenario is shown in Fig. 2.4c for $R = -4000$ km; a qualitatively similar profile results for any negative values of R with magnitude less than 6000 km. Here, $\partial T_v/\partial y$ is negative from 1-5 bars and (marginally) positive from 5-12 bars; it is similar in magnitude but opposite in sign to the first case we described (left column of Fig. 2.4). Therefore, this profile suggests just the reverse: that from 1-5 bars, the region to the south is *less dense* than the region to the north of the probe site; below 5 bars, the region to the south is denser than that to the north. Virtual potential temperature profiles are shown in Fig. 2.4f, assuming the region 2000 km north of the probe site is dry adiabatic. (Above 1.5 bars, the region *south* of the probe site is assumed dry adiabatic.)

These ideas fit our expectations: they suggest that regions to the south are *stable* from 2-6 bars, consistent with moist adiabatic upwellings, and that the regions to the north are dry adiabatic below 1.5 bars. Further, they suggest that the hot spot is less dense from 5-12 bars (though again this result is robust to only 1-σ), as required to prevent mixing of volatiles from below. As before, the stable layer above 6 bars results from the major change in $\partial u/\partial p$ between 1 and 6 bars, a robust feature in the data. The pressure at the base of this stable layer results directly from the wind data and is *independent* of any assumptions about moist convection. Nevertheless, it agrees well with that predicted for moist adiabatic upwellings containing a water abundance of 1-2 times solar (Atreya and Romani 1985). (The magnitude of these density differences is poorly constrained. All values of $-6000\,\text{km} < R < 0$ yield $\partial T_v/\partial y$ profiles *qualitatively* similar to that in Fig. 2.4c, including the stable layer above 6 bars and the sign of the density differences at all levels. The exact *magnitude* of $\partial T_v/\partial y$ is sensitive to R, however.) Interestingly, the θ_v profiles show a stable layer above 1.5 bars in the hot spot. This feature, which appears to be robust, is suggestive of radiative cooling in the downwelling above 1.5 bars; further, it implies that the hot spot may be less dense than the equatorial zone above 0.5 bars, as suggested in groundbased infrared data (Orton et al. 1996).

In summary, based on simple notions of how convection should operate, we favor

the rightmost column of Fig. 2.4. The negative values of R required for this scenario are in qualitative agreement with the fact that a clockwise circulation was seen south of a hot spot in Galileo images, although the observed radius of curvature may be greater than 6000 km as measured in system III (Vasavada et al. 1998).

All values of R require the probe site to be slightly stable above a few bars depth. If the profiles had been calculated assuming the probe site were neutrally stable, then some regions away from the probe site would be unstable, which is impossible. The required stability at the probe site scales with the latitude range over which $\partial T_v/\partial y$ is extrapolated; for 2000 km extrapolation in either direction, the required stability is $\sim 1\,\mathrm{K}$ (Fig. 2.4d-f). Although the probe temperature measurements suggest a dry adiabatic profile (Seiff et al. 1997b), the uncertainty is about 1 K. The stable layer which is required for a consistent explanation of the winds may therefore be consistent with the temperature data.

The $\sim 1\,\mathrm{K}$ stability quoted above implies a Richardson number of about 0.5 between the ammonia cloud top and 5 bars.

In the scenarios above, we assumed that R was constant with depth. If R varies with depth, the number of possibilities multiplies by many-fold. We give one example. Suppose the hot spot is less dense than the equatorial zone at all depths (as in Fig. 2.2b) and that the probe entered the boundary between the two regions. $-\partial\Phi/\partial y$ (a positive quantity) then increases with depth from 0.5-20 bars. From 0.5-5 bars, geostrophic balance holds, so the increasing $u(p)$ allows the balance $fu = -\partial\Phi/\partial y$. At $p > 5$ bars, the wind is constant with depth, so the increasing $-\partial\Phi/\partial y$ must be balanced by u^2/R. This requires positive R with decreases with depth. The interpretation is as follows. The deep hot spot is a cyclonic vortex at the southern edge of the north equatorial belt; the probe fell into the south edge of the vortex. The top of the vortex is at 5 bars. Above that there is no vortex. This model explains the absence of a vortex in Galileo images of a hot spot (Vasavada et al. 1998), and may also explain the long lifetime of hot spots (Ortiz et al. 1998) — hot spots are all underlain by long-lived deep vortices which do not penetrate to the cloud level. If the winds are truly zonal, however, models such as this are improbable: the wind

vectors are unlikely to be parallel at all depths if the flow curvature varies with depth as well. However, Atkinson et al. (1997) *assumed* zonality in deriving their wind profile. Although tracking of the probe signal from the ground seems to corroborate this assumption from 1-5 bars (Folkner et al. 1997), substantial uncertainties exist, and their data place no constraints on the wind at $p > 5$ bars. Further, while Seiff et al.'s (1997a) analysis of probe accelerometer measurements have yielded a wind profile in qualitative agreement with that of Atkinson et al., they assumed zonality as well. It is possible that these data would allow non-zonal winds whose direction varied with depth; if so, models with height-variable R become more plausible.

2.5 Puzzle III: Introducing volatiles at different heights

As shown in Fig. 2.1, analysis of the attenuation of the probe radio signal suggests that ammonia increased rapidly with depth from 1-8 bars, reaching a plateau at $p > 8$ bars (Folkner et al. 1998). Further, according to data taken from the Galileo probe's mass spectrometer, H_2S surged from 0.3 times solar at 8.6 bars to solar by 9.6 bars, tentatively leveling off to 2.7 times solar at 16 bars (Niemann et al. 1996, 1998). Water, however, was less than 3% and $\sim$ 30% solar at 12 and 19 bars, respectively (Niemann et al. 1998). These measurements are puzzling. They suggest that the observed volatiles were not introduced into the downdraft by *vertical* mixing, since moist plumes rising from below should have the deep, constant ratios of the NH_3, H_2S and water mole fractions, and mixing of these plumes into the dry downdraft would not change these ratios.

Here we present two plausible mechanisms for producing the observed pattern of increasing volatiles with depth. An important clue is that the order in which the volatiles rise with depth mimics that predicted by equilibrium condensation models (Weidenschilling and Lewis 1973) but occurs at much greater pressures (Fig. 2.1).

2.5.1 Lateral mixing

First, as suggested by Atreya et al. (1997), volatiles could be introduced into the downdraft by *lateral* mixing. The volatiles from 1-8 bars at the probe site would have originated above the NH_3 lifting condensation level (at perhaps 0.6 bars for solar abundances) in an adjacent region, since this is the expected pressure range where ammonia increases strongly with depth while H_2S and water remain low (Fig. 2.1, right panel). Similarly, the increase in H_2S from 9-16 bars would occur because air originating near the NH_4SH condensation level (near 2 bars) elsewhere mixed downward to 9-16 bars at the probe site. The relative absence of H_2S above 9 bars would be explained because any material mixed to pressures less than 9 bars at the probe site would have originated above $\sim$ 1 bar in the source region, where H_2S is absent. The obvious mechanism is that the mixed air follows isopycnals, or surfaces of constant virtual potential temperature (Eq. 2.7). Physically, this simply means that when parcels move from one stable air column to another, they maintain their position of neutral buoyancy. If the new air column is less dense than the old column, the parcel's height of neutral buoyancy will decrease as it moves, so the mixed air will sink. Conversely, if the new column is denser, the mixed air will rise as it enters the new column. Mixing is observed to follow isopycnals in Earth's atmosphere and oceans when diabatic forcing is weak (e.g., Holton et al. 1995).

In Fig. 2.5 we illustrate the mixing process for two situations, corresponding to the density profiles in Fig. 2.2a and b. In Fig. 2.5a, the hot spot is denser than the surroundings from 1-5 bars and less dense below 5 bars, as would occur if the downwelling undergoes radiative cooling as it descends into the hot spot. Near the 5-bar level, the density in the hot spot is the same as in the surroundings; this corresponds to a horizontal isopycnal (surface of constant θ_v). Above 5 bars, the isopycnals bow upward within the hot spot because it is denser than the surroundings, while below 5 bars, they bow downward. This scenario cannot explain the observations. It predicts that H_2S should be present in the hot spot at all heights below 2 bars, contrary to observation; water should be abundant everywhere below 5 bars. Ammonia should

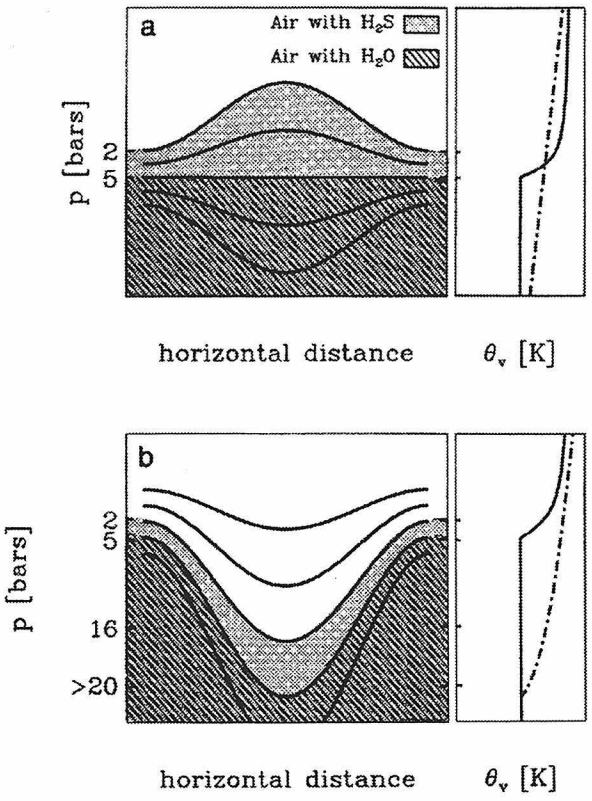

Figure 2.5: Cartoon depicting two possible scenarios for mixing volatiles into the downdraft, assuming mixing along isopycnals. Left panels depict isopycnals (solid lines) vs. pressure and horizontal distance; the hot spot is assumed to span the middle half of the horizontal axis. Right panels show the assumed virtual potential temperatures. The dashed-dot and solid curves are the profiles in the hot spot and surroundings, respectively. (a) From 1-5 bars the hot spot is assumed denser than the surroundings; for $p > 5$ bars, it is less dense (as in Fig. 2.2a). This cannot explain the data shown in Fig. 2.1. (b) The hot spot is assumed less dense for all $p > 0.5$ bars (as in Fig. 2.2b). This readily explains the observed profiles of NH_3, H_2S, and H_2O shown in Fig. 2.1.

be constant below 0.6 bars, in disagreement with observation (Folkner et al. 1998).

Figure 2.5b shows the second scenario. Here, the hot spot is less dense than the surroundings at all heights below 0.5 bars; this corresponds to the situation where the upwelling air radiatively warms before descending into the hot spot (or where the circulation time is so rapid that no radiative warming or cooling can occur). In this scenario, the isopycnals bow downward inside the hot spot at all heights. Therefore, volatiles at all heights move downward as they enter the hot spot. This scenario readily explains the mass spectrometer and signal attenuation observations compiled in Fig. 2.1. Air parcels containing traces of H_2S, which begin at perhaps 1 bar, move to 9 bars at the probe site. Air at the 2 bar NH_4SH lifting condensation level moves to 16 bars at the probe site. This explains why the H_2S mole fraction was constant below 16 bars. Material originating at 5 bars mixes to depths below 20 bars; this explains why the probe measured a water mole fraction which was still increasing at 20 bars. This model therefore provides a natural explanation for why the downdraft remains dry despite the fact that horizontal mixing appears to be very vigorous on Jupiter. (Possibly, dissipative processes could cause a small component of horizontal mixing *across* isopycnals. Subsidence would then be required to maintain Fig. 2.5b in steady state. This is analogous to the balance between subsidence and mixing described in Section 2.3.3.)

If lateral mixing is to explain the observed pattern of volatiles, therefore, an important implication results: the dry downdraft is *less dense* than the volatile source region at all depths below 0.5 bars. (Because mixing along isopycnals conserves θ_v — a measure of density — such mixing cannot affect the density structure. The low density must be independently created by another mechanism, perhaps that suggested in Section 2.3.) If the volatile source region is south of the probe site, this contradicts our favored interpretation of the probe winds, which suggests that (from 1-5 bars) the hot spot is denser than the region directly south of the probe site. Possibly, the volatiles mixed into the probe site originated in a different region with a greater density.

2.5.2 Column Stretching

Alternatively, the observed profiles might result from column stretching in complete absence of lateral mixing. In this scenario, the air at the probe site would have begun with ammonia decreasing above 0.6 bars, H_2S decreasing above 2 bars, and water decreasing above 5 bars, as predicted by thermochemical models (Weidenschilling and Lewis 1973; see Fig. 2.1). Suppose the top of the air column were maintained at roughly the same height, while the bottom of the column moved downward. As the column stretched, the *relative* location of all parcels within the column would be fixed. The increase in NH_3 from 1-8 bars would then be the signature of a "fossil" NH_3 lifting condensation level which originated at 0.6 bars but was pushed to 8 bars during the stretching process; similarly, the NH_4SH lifting condensation level would be pushed from 2 to 16 bars. The original water lifting condensation level near 5 bars would be pushed even deeper, explaining the observation that H_2S increased before water.

This scenario provides a natural explanation for the nearly dry adiabatic conditions at the probe site. A moist adiabat associated with three times solar H_2S produces 0.1 K of warming relative to a dry adiabat (Atreya and Romani 1985). We therefore expect 0.1 K of (temperature) stability between 9 and 16 bars at the probe site, consistent with observation. Although condensation of water yields warming of 2 K for solar abundance, this stability may have been positioned somewhat below 20 bars.

Stretching might occur in a manner analogous to flow over mountains on Earth. On Jupiter, the topography might consist of a deep ($p > 20$ bar) isopycnal surface which varies in height from place to place. As the air column moved over the variable isopycnal, it would stretch and contract. This speculation might be testable by measuring the vorticity ζ along air trajectories in Galileo images. Parcels tend to maintain constant values of potential vorticity, defined (in the shallow water context) as $(\zeta + f)/h$, where f is the Coriolis parameter and h is the height of the column. If air columns elongated as they moved over the hot spot, the value of ζ would change

along streamlines.

This scenario qualitatively matches Galileo orbiter observations that air flowed into a hot spot at $30\,\mathrm{m\,s^{-1}}$ from the southwest (Vasavada et al. 1998). If the column elongated and contracted as it entered and exited the hot spot, the time between elongation and contraction would be 1-2 days.

This simple model predicts that the dry downdraft is less dense than the initial (pre-stretched) profile at all pressures. *If* the initial, pre-stretched density profile is the same as that in the regions surrounding the hot spot, then the isopycnals must bow downward in the hot spot, as in Fig. 2.5b.

2.6 What do the data say about the forcing?

In Section 2.3 we proposed that the hot spot circulation is thermally indirect below 5 bars. For this hypothesis to be reasonable, the energy liberated by the atmospheric heat engine must be great enough to push dry air to 10 bars or deeper. In this section we address this issue by using available data to tentatively evaluate the magnitude and nature of the forcing. Because of the paucity of data, we cannot directly evaluate any of the terms in Eq. (2.3). However, we do have limited information on the vertical profiles of density from 0.5-20 bars in the hot spot relative to its surroundings. We therefore may be able to find the column integrated density in the hot spot and compare it to that in the surroundings. This comparison will allow us to determine whether the vertical flux of geopotential energy is sufficient to drive the indirect motions.

To attack this problem, we recast the kinetic energy equation (2.3) from Section 2.3 into another form. Averaging in time and assuming the circulation consists of a mean circulation followed by all parcels (an approach used on Earth by Renno and Ingersoll (1995)), Eq. (2.3) becomes

$$\dot{M} \int \frac{k}{m_d} \left(T_v \,|_{\rm up} - T_v|_{\rm down} \right) \, d\, ln\, p = \dot{M} \int \left(\frac{1}{\rho_{\rm up}} - \frac{1}{\rho_{\rm down}} \right) \, dp = \bar{F}_{\rm bot} + \bar{F}_{\rm top} + \bar{F}_{\rm sides} - \bar{D} \tag{2.8}$$

where the overbar denotes time average and $F_{\rm bot}$, $F_{\rm top}$, and $F_{\rm sides}$ are the sums of kinetic and geopotential energy flux at the bottom, top, and side boundaries. $\dot{M}$ is the mass per time transported through isobars in the updrafts and downdrafts divided by the horizontal area of the domain, $\rho_{\rm up}$ is the density in locations where a moving parcel's pressure decreases with time, and $\rho_{\rm down}$ is the density in regions where pressure increases with time.

Although we cannot evaluate $\dot{M}$, $\bar{F}_{\rm bot}$, $\bar{F}_{\rm sides}$, or D, the data provide constraints on $\int \rho_{\rm up}^{-1} - \rho_{\rm down}^{-1} \, dp$. If this integral is positive, the *column integrated* motion is thermally direct; the direct motion from 1-5 bars provides sufficient geopotential energy flux to drive the indirect circulation at deeper levels. If negative, the column integrated motion is thermally indirect, and other forcing is required.

Three forms of data have implications for the density of the hot spot relative to the surroundings. These are (1) a comparison of Voyager occultation and Galileo probe temperature data, (2) the interpretation of the probe winds presented in Section 2.4, and (3) the interpretation of the mass spectrometer data presented in Section 2.5. We consider each in turn.

2.6.1 Temperature data

The Voyager radio occultation experiment measured temperatures to the 1 bar level at two latitudes, one at the equator and another at 13°S in the south equatorial belt (Lindal et al. 1981). When corrected for the new He/H_2 value from Galileo (Niemann et al. 1996, von Zahn et al. 1996), the data imply temperatures of 169 K at 1 bar. The 5 K uncertainty quoted by Lindal et al. includes error in both the data themselves and in the assumed helium abundance. For a known helium abundance, the error in temperature is probably about half this value (Conrath et al. 1984). In

contrast, the Galileo probe measured a temperature of 166 ± 1 K at 1 bar (Seiff et al. 1997b). Thus, the hot spot appears to be colder at 1 bar than the regions sampled by Voyager.

If downwelling occurs in the hot spot and upwelling occurs at the equator (as suggested by high cloud abundance and cold temperatures there; Gierasch et al. 1986, Carlson et al. 1994), the temperatures listed above suggest that the motion at 1 bar is thermally direct. We wish to determine whether this thermally direct motion provides enough energy to force dry air to 10-20 bars. To do so, we assume that the external energy fluxes (minus dissipation) are negligible, so that the sole energy source is the direct loop in Fig. 2.2a. Eq. (2.8) then becomes

$$\int_{p_{bot}}^{p_{top}} \frac{1}{\rho_{\rm up}}\, dp = \int_{p_{bot}}^{p_{top}} \frac{1}{\rho_{\rm down}}\, dp \tag{2.9}$$

We now use Eq. (2.9) to estimate the depth of the dry downdraft. Combining data from the Galileo probe's atmospheric structure experiment (Seiff et al. 1996, 1997) with that from the Voyager radio occultation experiment (Lindal et al. 1981) allows us to estimate the two terms in the equation. We use the probe data for the downdraft. We use the Voyager data for the updraft; we extrapolate downward with a moist adiabat. When the saturation water vapor mixing ratio exceeds an assumed deep value (which occurs at 5, 6, or 7 bars for 1, 2, or 3 times solar respectively), we continue the extrapolation as a dry adiabat (as occurs in Fig. 2.2).

Figure 2.6a illustrates the virtual temperature vs. $\log p$ for the Galileo data (solid line) and for several moist adiabats, all of which pass through 169 K at 1 bar (other curves). The various moist adiabats assume different deep water abundances, from $1.0 - 3.0$ times solar. Figure 2.6b illustrates the same curves, but with the Galileo dry adiabat subtracted off. When interpreted as a single thermodynamic cycle (up along a moist adiabat and down along the dry adiabat), the area of the cycle is proportional to work done. Our assumption of no dissipation and no forcing implies no net work, so that the "positive" area (hatched) cancels out the "negative" area (stippled for the 2 times solar case). For a given moist adiabat, this specifies the depth to which

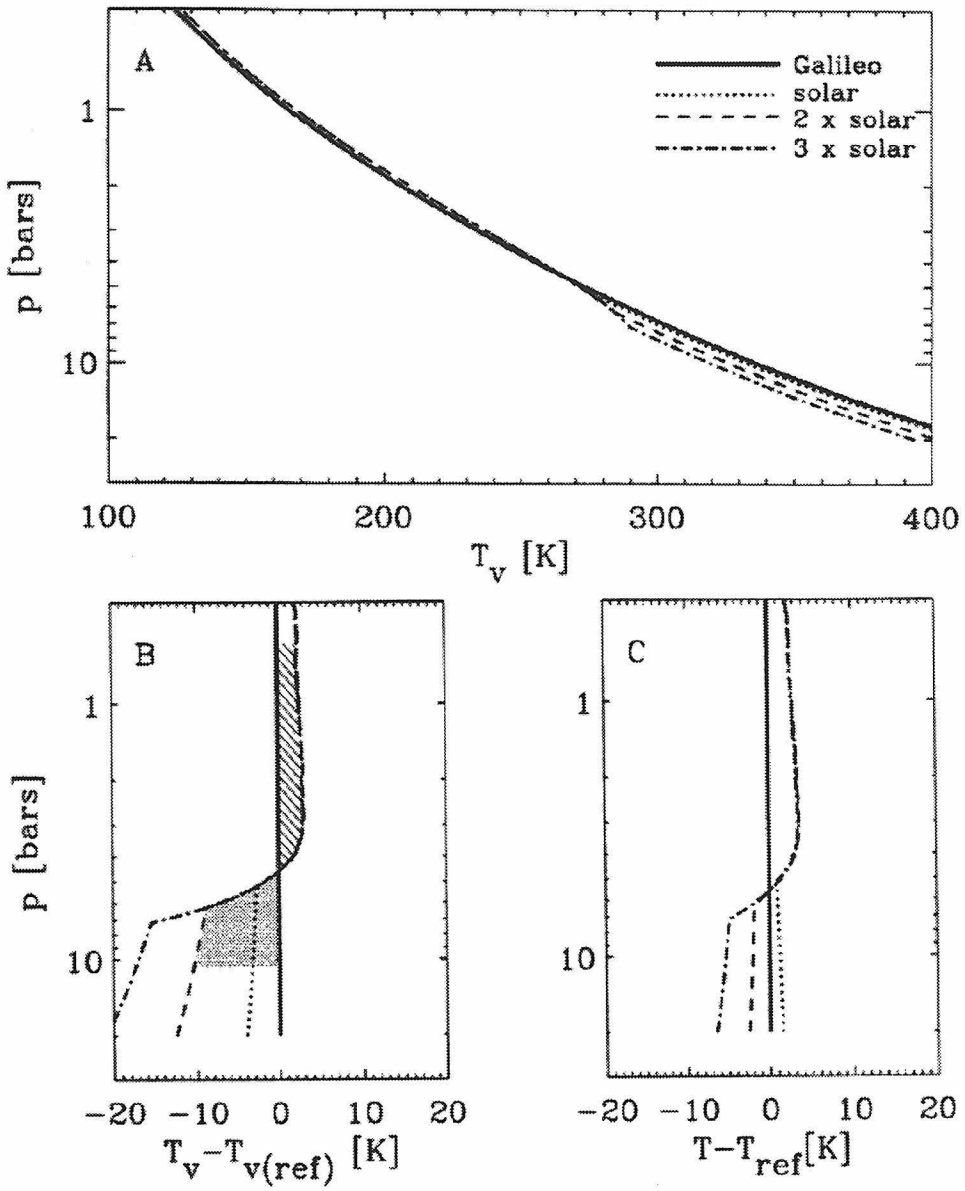

Figure 2.6: (a) Virtual temperature vs. $\log p$ for a dry adiabat representing the Galileo probe data (solid line), and for several moist adiabats with various assumed deep water abundances. All the moist adiabats pass through 169 K at 1 bar, as measured by the Voyager occultation. (b) Same, but with the dry adiabat subtracted off. The zero-dissipation/ forcing condition requires that the area between the probe data and a given moist adiabat is zero, implying for the 2 times solar case that the hatched area equals the stippled area. This sets the depth at the base of the downdraft. (c) Temperature vs. $\log p$, with the Galileo dry adiabat subtracted off.

the "negative" area can extend, i.e., it sets the depth of the dry downdraft. (We assume the downdraft has 20% solar water abundance above this depth; Niemann et al. 1996.) For 1, 2, or 3 times solar water, the downdraft extends to 30, 11, or 9 bars respectively. A virtual temperature stability of several K is predicted at the base of the dry downdraft.

Therefore, *in the absence of external mechanical energy fluxes*, the thermally direct motion from 1-5 bars can provide enough energy to force dry air to 10-30 bars, as observed. (If kinetic energy or pressure forces created elsewhere do additional work on the indirect circulation, the dry downdraft could extend even deeper.)

Because the scenario here requires radiative cooling, we expect the downwelling time to be of order years. If gradual upwelling occurs over half the area, the upwelling and downwelling times could be comparable. If upwelling occurs in isolated thunderstorms occupying a small fractional area (as on Earth), the upwelling time could be as short as hours.

2.6.2 Interpretation of wind data

Our favored interpretation of the probe winds (Fig. 2.4, rightmost column) suggests that the hot spot is denser than the equatorial zone from 1-5 bars, but less dense than the equatorial zone below 5 bars. Again, this suggests a thermally direct circulation overlying the indirect circulation. We use the solid and dashed-dot lines from Fig. 2.4f as the downdraft and updraft, respectively. We find that the integral in Eq. (2.8) (taken from 0.5 to 12 bars) is positive, so that the direct circulation releases more energy than the indirect circulation (from 5-12 bars) absorbs. If we extrapolate these curves downward we find that the depth at which the energy integrals balance — and hence the maximum depth of a dry downdraft powered only by the direct loop from 1-5 bars — is 1000 bars. (If only half the energy released in the direct loop goes into the indirect motion, the maximum depth is 100 bars.) The reason this depth is so much larger than that obtained from the temperature data is that according to the wind data, the virtual temperature in the downdraft is only 0.3 K greater than that in

the updraft at 10 bars. In contrast, the virtual temperature difference obtained from the temperature data is 4, 11, and 17 K for 1, 2, and 3 times solar water abundance, respectively.

These results suggest that the energy released in the thermally direct part of the circulation from 1-5 bars is sufficient to push dry air to depth comparable to, perhaps far exceeding, those sampled by the probe. Thus, if (1) the hot spot is denser than the surroundings (from 1-5 bars) as suggested by wind and temperature data, and (2) this density contrast is indicative of updraft-downdraft differences, then the hot spot circulation may be "self-driving," requiring no energy input from other regions on Jupiter.

2.6.3 Interpretation of mass spectrometer data

If lateral mixing is to explain the increase in H_2S at lower pressures than water, then the hot spot must be less dense at all heights from 0.5 bars to the base of the dry downdraft; this may be true for stretching as well. This suggests that external forcing of the downdraft is required (the integral in Eq. (2.8) is negative). Here we estimate the maximum possible forcing such dry downdrafts might require, and compare it to that made available by the atmosphere.

The power per area absorbed by indirect circulations can be estimated from Eq. (2.8). Suppose the dry downdrafts have a virtual temperature ΔT_v greater than that of the updrafts. The vertical mass flux in the dry downdrafts is $\dot{M} \approx \omega/g$, where $\omega = dp/dt$ is the vertical velocity in pressure coordinates. The mean power per area absorbed by the dry downdrafts is (from Eq. (2.8)) $\Delta T_v k\, ln(p_{bot}/p_{top})\omega/(g m_d)$. We assume the dry downdrafts extend from the ammonia cloud level ($p_{top} = 0.5$ bars) to a lower pressure $p_{bot} = 20$ bars, with $\omega = 6 \times 10^{-5}\,\mathrm{Pa\,s^{-1}}$ as obtained from retrievals at 270 mbar (West et al. 1992). We use $\Delta T_v = 3\,\mathrm{K}$, which corresponds to the density difference between updrafts and downdrafts below a few bars if the water abundance is near solar and little radiative cooling occurs near cloud top. The mean power per area absorbed by the indirect circulations is then about $0.1\,\mathrm{W\,m^{-2}}$. If we instead use

$\omega = 2 \times 10^{-3}\,\mathrm{Pa\,s^{-1}}$, as may be required to balance the upward mixing of volatiles (Section 2.3.3), the power per area is $3\,\mathrm{W\,m^{-2}}$. (This result assumes dry downdrafts cover essentially half the planet; if they are confined to local areas, the power per area would be lower.) These values are substantially less than Jupiter's $14\,\mathrm{W\,m^{-2}}$ mean heat flux, and could be comparable to the generation of large scale energy by atmospheric convection. Existence of such indirect circulations is thus energetically reasonable.

2.7 Discussion

The Galileo probe measured substantially depleted volatiles to 12 bars or deeper, suggesting that the probe entered a dry downdraft. We provided possible resolutions to three problems raised by Galileo probe data. To explain the dryness below the condensation level, we proposed that the downdraft is part of a thermally indirect circulation, operating as a heat engine in reverse. This suppresses convection from below and keeps the downdraft dry. Available data tentatively suggest that this circulation is energetically reasonable. Next, to explain the Galileo probe winds, we invoked gradient wind balance to calculate latitudinal gradients of density versus depth at the probe site. A range of profiles is possible, depending on the radius of curvature of the winds. Finally, the probe found that NH_3, H_2S, and water increased with depth at different rates (Fig. 2.1). We suggested that this signature results from either (1) lateral mixing along isopycnals, or (2) stretching of the air column down from $p < 0.5$ bars.

Some aspects of our different models are consistent with both external data and each other. Consider first our favored interpretation of probe winds. This interpretation suggests that for $p > 5$ bars, the hot spot is less dense than the equatorial zone—exactly as postulated to keep the downdraft dry (compare Fig. 2.4f with the cartoon in Fig. 2.2a). Further, this scenario requires a counterclockwise circulation south of the hot spot; such a circulation pattern was seen in Galileo images for another hot spot (Vasavada et al. 1998). Finally, it suggests a stable layer in the hot

spot above 1.5 bars. This stable region could allow the hot spot to be less dense than the equatorial zone for $p < 0.5$ bars, in accord with Voyager IRIS (Gierasch et al. 1986) and groundbased infrared (Orton et al. 1996) data.

The suggestion that the probe site is underlain by a stable layer (necessary to keep the downdraft dry) has both direct and indirect observational support. The temperature and mass spectrometer data together suggest that the probe site was statically stable below 12 bars, since temperature was dry adiabatic and molecular weight increased with depth. (Plumes rising from below would therefore have the same temperature as their surroundings but would have a greater molecular weight and hence density, so would be inhibited from rising.) If water increased to solar below 20 bars, for example, the virtual temperature stability would be 3 K. Further, the fact that NH_3, H_2S and water increased separately implies that the observed volatiles were not introduced into the downdraft by vertical convection from below. This is consistent with existence of a stable layer inhibiting such convection.

On the other hand, there appears to be a major inconsistency between our favored explantions for the wind and mass spectrometer data. Our favored interpretation of the winds (Fig. 2.4, rightmost column) suggests that from 1-5 bars, the hot spot (north of the probe site) is denser than the equatorial zone (south of the probe site). If lateral mixing is to explain the increase of volatiles at different heights, however, the hot spot must be less dense from 1-5 bars than the source region of the volatiles. If column stretching is to explain the increasing pattern of volatiles, then from 1-5 bars the hot spot should be less dense than the original (pre-stretched) column over this same height range. (This occurs because θ_v increases with height, so the stretching process increases θ_v at a given pressure.) In either case, if the region south of the hot spot has the same density structure as either the source region of the volatiles or the pre-stretched downdraft, then from 1-5 bars the hot spot must be less dense than the region to the south—in contradiction with our favored wind interpretation.

There are several possible resolutions to this inconsistency. The most likely explanation is that the region surrounding the hot spot is horizontally heterogeneous. If column stretching explains the volatile distribution, perhaps the original pre-stretched

column was denser than that south of the probe site. Upon stretching, the hot spot would remain denser (from 1-5 bars) than the region to the south; this would reconcile the wind and mass spectrometer analyses. Or, if mixing explains the volatile distribution, perhaps the volatiles in the hot spot originated in a region denser than that directly south of the probe site. This would allow the 1-5 bar region at the probe site to be denser than that directly south of the probe site (as suggested by the winds), yet less dense than the source region for the volatiles (as suggested by the mass spectrometer data). Another possibility is that our favored interpretation of the winds is incorrect; perhaps another scenario in Fig. 2.4 applies, the radius of curvature varies with depth, or gradient wind balance does not hold. Unfortunately, all of these possibilities are ad hoc and prevent us from achieving a satisfying synthesis of the Galileo data.

The clouds observed by the probe further complicate attempts to form a coherent picture. The nephelometer and net flux radiometer detected a cloud near 1.4 bars and possibly another above 0.5 bars, but no 5-bar water cloud (Ragent et al. 1996, 1998; Sromovsky et al. 1996, 1998). The simplest explanation is that the 0.5 and 1.4 bar clouds (presumed to be ammonia and NH_4SH) result from upward mixing of ammonia and H_2S vapor into the downdraft, as occurs in Fig. 2.5a; the sharp base of the 1.4 bar cloud would then be the NH_4SH lifting condensation level. As observed, Fig. 2.5a also predicts that no water cloud would form because water is not mixed upward as it enters the hot spot. As described in Section 2.5, however, Fig. 2.5a cannot explain the mass spectrometer and probe signal attenuation results from Fig. 2.1. The cloud and mass spectrometer/signal attenuation data might be reconciled if an upper tropospheric cloud were mixed or advected downward along isopycnals to 1.4 bars (consistent with Fig. 2.5b). This is unlikely, however. To explain the mass spectrometer/signal attenuation data, the isopycnals in Fig. 2.5b must bow downward by about 80 km, while the observed cloud was only $\sim 5-10$ km thick. Reconciling the data sets therefore requires the cloud to have existed at just the right pressure in the upper troposphere, so that when advected 80 km down, it ended up exactly at the lifting condensation level (as required to explain the cloud's

sharp base). Because cloud heights may follow isopycnals if the particle fall times are less than the cloud advection times, observations of cloud base pressures from Galileo NIMS or groundbased infrared data may help resolve this dilemma (e.g., Stewart et al. 1997).

New observations and modelling may help resolve the inconsistencies. Continued infrared and visible imaging observations from Galileo, Cassini, and the ground could clarify the extent to which dry regions are confined to hot spots, whether hot spots are coherent structures or waves propagating relative to the flow, and whether convergence (hence downwelling) occurs at hot spots (Vasavada et al. 1998). The answers may help us decide between the models presented here. High resolution imaging from Galileo and Cassini may constrain the radii of curvature likely to occur in the flow near hot spots, and nighttime lightning observations will help constrain the regions of upwelling.

Although the models of indirect circulations presented here were created to answer specific questions posed by Galileo data, they may have broader implications. Indirect circulations could play a central role in Jupiter's energetic cycle. The quasi-horizontal nature of atmospheric flows suggests that energy cascades from small to large scales (Charney 1971), contrary to the situation in three-dimensional flows. A sink for kinetic energy must therefore exist at the largest scales; otherwise, energy supplied by thunderstorms, baroclinic instabilities, or other sources at small scales would "pile up" at the largest scales and lead to continuous acceleration of the zonal jets. On Earth, friction against the surface removes much of this large-scale kinetic energy (Peixoto and Oort 1992, Tomatsu 1979), but the lack of a surface on Jupiter suggests that different mechanisms may be at work. Indirect circulations could provide the necessary sink on Jupiter, and it is therefore important to understand their dynamics.

2.8 References

ATREYA, S.K. AND P.N. ROMANI 1985. In *Planetary Meteorology,* ed. G. Hunt. Cambridge Univ. Press, Cambridge, 17.

ATREYA, S. 1996. In *International Conference on the Shoemaker-Levy 9 Jupiter Collision,* p. 2, Observatoire de Paris.

ATREYA, S., M.H. WONG, T. OWEN, H. NIEMANN, AND P. MAHAFFY 1996. Chemistry and clouds of the atmosphere of Jupiter: A Galileo perspective. In *Three Galileos: The Man, the Spacecraft, the Telescope* (conference proceedings) (J. Rahe, C. Barbieri, T. Johnson, A. Sohus, Eds.) Kluwer Academic Publishers, Dordrecht.

ATKINSON, D.H., J.B. POLLACK, AND A. SEIFF 1996. Galileo Doppler measurements of the deep zonal winds at Jupiter. *Science* **272,** 842-843.

ATKINSON, D.H., A.P. INGERSOLL, AND A. SEIFF 1997. Deep zonal winds on Jupiter: Update of Doppler tracking the Galileo probe from the orbiter. *Nature* **388,** 649-650.

BETTS, A.K. 1973. Non-precipitating convection and its parameterization. *Quart. J. Roy. Meteor. Soc.* **99,** 178-196.

CARLSON, B.E., A.A. LACIS, AND W.B. ROSSOW 1994. Belt-zone variations in the jovian cloud structure. *J. Geophys. Res.* **99,** 14,623-14,658.

CARLSON, R. AND 39 COAUTHORS 1996. Near-infrared spectroscopy and spectral mapping of Jupiter and the galilean satellites: results from Galileo's initial orbit. *Science* **274,** 385-388.

CHARNEY, J.G. 1971. Geostrophic turbulence. *J. Atmos. Sci.* **28,** 1087-1095.

CONRATH, B.J., D. GAUTIER, R.A. HANEL, AND J.S. HORNSTEIN 1984. The helium abundance of Saturn from Voyager measurements. *Astrophys. J.* **282,** 807-815.

DROSSART, P. AND 11 COAUTHORS 1998. The solar reflected component in Jupiter's 5 micron spectra from NIMS/Galileo observations. Submitted to *J. Geophys. Res.*

EMANUEL, K.A. 1994. *Atmospheric Convection,* Oxford Univ. Press, New York.

ENGEL, S., D.M. HUNTEN, A.S. ACKERMAN, AND O.B. TOON 1996. A whiff of cloud on Jupiter (abstract). *Bull. Amer. Astron. Soc.* **28,** 1141 [Abstract].

FOLKNER, W.M., R.A. PRESTON, J.S. BORDER, J. NAVARRO, W.E. WILSON, AND M. OESTREICH 1997. Earth-based radio tracking of the Galileo probe for Jupiter wind estimation. *Science* **275,** 644-646.

FOLKNER, W.M., R. WOO, AND S. NANDI 1998. Ammonia abundance in Jupiter's atmosphere derived from the attenuation of the Galileo probe's radio signal. Submitted to *J. Geophys. Res.*

GARRATT, J.R. 1992. *The atmospheric boundary layer.* Cambridge Univ. Press, New York.

GAUTIER, D. AND T. OWEN 1989. The composition of outer planet atmospheres. In *Origin and Evolution of Planetary and Satellite Atmospheres* (S.K. Atreya, J.B. Pollack, and M.S. Matthews, eds.) University of Arizona Press, Tucson.

GIERASCH, P.J., B.J. CONRATH, AND J.A. MAGALHAES 1986. Zonal mean properties of Jupiter's upper troposphere from Voyager infrared observations. *Icarus* **67,** 456-483.

GUILLOT, T. 1995. Condensation of methane, ammonia, and water and the inhibition of convection in giant planets. *Science* **269,** 1697-1699.

GUILLOT, T. 1996. A parallel between the results of the Galileo probe and the abundance of methane in Uranus and Neptune (abstract). *Bull. Amer. Astron. Society* **28,** 1142 [Abstract].

HALTINER, G.J. AND R.T. WILLIAMS 1980. *Numerical Prediction and Dynamic Meteorology.* John Wiley and Sons, New York.

HOLTON, J.R. 1992. *An Introduction to Dynamic Meteorology.* Academic Press, New York.

HOLTON, J.R., P.H. HAYNES, M.E. MCINTYRE, A.R. DOUGLASS, R.B. ROOD, AND L. PFISTER 1995. Stratosphere-troposphere exchange. *Rev. Geophys.* **33,** 403-439.

HUNTEN, D.M., M. TOMASKO, AND L. WALLACE 1980. Low-latitude thermal structure of Jupiter in the region 0.1-5 bars. *Icarus* **43,** 143-152.

INGERSOLL, A.P. AND C.C. PORCO 1978. Solar heating and internal heat flow on Jupiter. *Icarus* **35,** 27-43.

LINDAL, G.F. AND 11 COAUTHORS 1981. The atmosphere of Jupiter: an analysis of the Voyager radio occultation measurements. *J. Geophys. Res.* **86,** 8721-8727.

MAHAFFY, P. 1996. Recent calibration studies of the Galileo probe neutral mass spectrometer. *Eos* (fall suppl.), **77,** F438.

NIEMANN, H.B. AND 12 COAUTHORS 1996. The Galileo probe mass spectrometer: composition of Jupiter's atmosphere. *Science* **272,** 846-849.

NIEMANN, H.B. AND 11 COAUTHORS 1998. The composition of the jovian atmosphere as determined by the Galileo probe mass spectrometer. *J. Geophys. Res.*, in press.

ORTIZ, J.L, G.S. ORTON, S.T. STEWART, AND B.M. FISHER 1998. Evolution and persistence of 5-μm hot spots at the Galileo probe entry latitude. *J. Geophys. Res.*, in press.

ORTON, G. AND 40 COAUTHORS 1996. Earth-based observations of the Galileo Probe entry site. *Science* **272,** 839-840.

ORTON, G.S., B.M. FISHER, S.T. STEWART, J.L. ORTIZ, M. MARINOVA, S. HINKLEY, V. KRISHNAN, M. MASANOVIC, J. TESIC, AND A. TZIOLAS 1998. Characteristics of Galileo probe entry site from Earth-based remote sensing observations. *J. Geophys. Res.*, in press.

OWEN, T.C. AND 11 COAUTHORS 1996. *Eos* (spring suppl.), **77,** S171.

PEIXOTO, J.P. AND A.H. OORT 1992. *Physics of Climate,* American Institute of Physics, New York.

RAGENT, B., D.S. COLBURN, P. AVRIN, AND K.A. RAGES 1996. Results of the Galileo probe nephelometer experiment. *Science* **272,** 854-856.

RAGENT, B., D.S. COLBURN, K.A. RAGES, T.C.D. KNIGHT, P. ARVIN, G.S. ORTON, AND G.W. GRAMS 1998. The clouds of Jupiter: Results of the Galileo Jupiter Mission probe nephelometer experiment. Submitted to *J. Geophys. Res.*

RENNO, N.O. AND A.P. INGERSOLL 1995. Natural convection as a heat engine–a theory for CAPE. *J. Atmos. Sci.* **53,** 572-585.

ROOS-SEROTE, M.C. AND 12 COAUTHORS 1998. Analysis of Jupiter NEB hot spots in the 4-5 micron range from Galileo/NIMS observations: measurements of cloud opacity, water, and ammonia. Submitted to *J. Geophs. Res.*

SALBY, M.L. 1996. *Fundamentals of Atmospheric Physics,* Academic Press, New York.

SEIFF, A., R.C. BLANCHARD, T.C.D. KNIGHT, G. SCHUBERT, D.B. KIRK, D. ATKINSON, J.D. MIHALOV, AND R.E. YOUNG 1997a. Wind speeds measured in the deep jovian atmosphere by the Galileo probe accelerometers. *Nature* **388,** 650-652.

SEIFF, A., D.B. KIRK, T.C.D. KNIGHT, R.E. YOUNG, J.D. MIHALOV, L.A. YOUNG, F.S. MILOS, G. SCHUBERT, R.C. BLANCHARD, AND D. ATKINSON 1997b. Thermal structure of Jupiter's atmosphere near the edge of a 5-micron hot spot in the north equatorial belt. *J. Geophys. Res.*, in press.

SEIFF, A., D.B. KIRK, T.C.D. KNIGHT, J.D. MIHALOV, R.C. BLANCHARD, R.E. YOUNG, G. SCHUBERT, U. VON ZAHN, G. LEHMACHER, F.S. MILOS, AND J. WANG 1996. Structure of the atmosphere of Jupiter: Galileo probe measurements. *Science* **272,** 844-845.

SROMOVSKY, L.A., F.A. BEST, A.D. COLLARD, P.M. FRY, H.E. REVERCOMB, R.S. FREEDMAN, G.S. ORTON, J.L. HAYDEN, M.G. TOMASKO, AND M.T. LEMMON 1996. Solar and thermal radiation in Jupiter's atmosphere: initial results of the Galileo probe net flux radiometer. *Science* **272,** 851-854.

SROMOVSKY, L.A., A.D. COLLARD, P.M. FRY, G.S. ORTON, M.T. LEMMON, M.G. TOMASKO, AND R.S. FREEDMAN 1998. Galileo probe measurements of thermal and solar radiation fluxes in the jovian atmosphere. Submitted to *J. Geophys. Res.*

STEWART, S.T., G.S. ORTON, B.M. FISHER, AND K.H. BAINES 1997. The cloud structure of the jovian north equatorial zone: context of the Galileo probe entry latitude. Submitted to *J. Geophys. Res.*

TOMATSU, K. 1979. Spectral energetics of the troposphere and lower stratosphere. *Adv. Geophysics* **21,** 289-405.

TURNER, J.S. 1973. *Buoyancy Effects in Fluids.* Cambridge Univ. Press, Cambridge.

VASAVADA, A.R. AND 12 COAUTHORS 1998. Galileo imaging of Jupiter's atmosphere: the great red spot, equatorial region and white ovals. *Icarus*, in press.

VON ZAHN, U. AND D.M. HUNTEN 1996. The helium mass fraction in Jupiter's atmosphere. *Science* **272,** 849-851.

WEIDENSCHILLING, S.J. AND J.S. LEWIS 1973. Atmospheric and cloud structures of the jovian planets. *Icarus* **20,** 465-476.

WEST, R.A., A.J. FRIEDSON, AND J.F. APPLEBY 1992. Jovian large-scale stratospheric circulation. *Icarus* **100,** 245-259.

YOUNG, R.E. 1998. The Galileo probe mission to Jupiter: science overview. *J. Geophys. Res.*, in press.

Chapter 3

Shallow water models of Jovian equatorial dynamics

Adam P. Showman

James Y-K. Cho

and

Andrew P. Ingersoll

Division of Geological and Planetary Science 150-21

California Institute of Technology

Pasadena, CA 91125

3.1 Abstract

The perplexing dryness measured by the Galileo probe is most easily explained by a dry downdraft at the probe site. Such dry downdrafts have never been produced in an atmospheric dynamics model, however, and it is unclear whether they are dynamically possible. I am exploring the dynamical origin and evolution of such downdrafts using a global model consisting of a stratified atmosphere overlying a deep, adiabatic interior. To do so, I numerically solve the full non-linear shallow water equations, which are the simplest equations applicable for such a system. In this chapter I define the problem and describe my approach in attacking it.

3.2 Introduction

As described in the previous chapter, the Galileo probe measured substantially depleted abundances (relative to solar) of water and H_2S to the 10 bar level or deeper. Further, between 8 and 16 bars, H_2S surged from 0.3 to 2.7 times solar (Niemann et al. 1998), and ammonia rose from less than 2 to about 4 times solar from 1 to 10 bars (Folkner et al. 1998). There are also hints that the water abundance increased between 12 and 20 bars. (See Fig. 2.1 for a summary of the probe data on ammonia, H_2S, and water.) These measurements are inconsistent with global depletion of volatiles from Jupiter's interior; instead, a meteorological explanation is required. This requirement is qualitatively consistent with the fact that the probe entered a 5-μm hot spot, a local atmospheric region known to be unusually low in cloud abundance (Orton et al. 1996, Carlson et al. 1994). Several authors have therefore suggested that condensation and rainout removes water, ammonia, and H_2S from updrafts located outside the hot spot. This dessicated air then descends within hot spots (Showman and Ingersoll 1998 [which is presented in Chapter 2 of this thesis], Owen et al. 1996, Atreya 1996).

Such dry downdrafts have never been produced in an atmospheric dynamics model, however, and it is unclear whether they are dynamically possible. This strongly

limits interpretation of the Galileo probe data and prevents us from understanding their full implications for Jupiter. The key to understanding the probe data lies in a better understanding of hot spots. Therefore, I am investigating the origin, stability, and evolution of hot spots and their hypothesized downdrafts. To do so, I numerically solve the shallow water equations, which are the simplest model equations containing the major processes relevant for large-scale atmospheric dynamics. (The initial study uses a single-layer model; in the future I will extend the model to 64 vertical levels.) Such models have been successfully used to study Jupiter's multiple jets and vortices (e.g., Williams and Wilson 1988, Dowling and Ingersoll 1989, Cho and Polvani 1996), but these studies did not focus on hot spots or other equatorial phenomena. The project described here is the first systematic shallow water study of jovian equatorial dynamics. By testing the idea that the lack of water results from local meteorology rather than a global suppression, this work may help resolve one of the most perplexing puzzles raised by Galileo.

I first describe the available constraints in more detail. This is followed by a discussion of the physical model and numerical methodology.

3.3 Constraints on the nature of hot spots

Galileo and groundbased data provide constraints which lead to two qualitative end-member scenarios for the dynamics of hot spots. Hot spots reside at 8°N latitude within Jupiter's north equatorial belt. About 10 evenly spaced hot spots exist around the planet at any one time; they move together in a single reference frame, roughly $100\,\mathrm{m\,sec^{-1}}$ eastward in System III (Ortiz et al. 1998). The fact that vortices often form evenly-spaced trains and are ubiquitous features in Jupiter's atmosphere suggests that hot spots may be vortices advecting with the mean flow, which is also about $100\,\mathrm{m\,sec^{-1}}$ at the latitude of hot spots. However, Galileo images of a single hot spot show that it propagates relative to small cloud features and does not clearly resemble an organized vortex (Vasavada et al. 1998). These observations suggest an alternate scenario where hot spots constitute waves propagating relative to the

ambient air flow.

When the arguments presented in Section 2.5 are invoked, these two scenarios can each explain the pattern of volatiles observed at the probe site. (This pattern is shown in the left panel of Fig. 2.1, where it is seen that the abundances of ammonia, H_2S, and water all rose at different pressures. The *order* of the observed increases matches that of the condensation model in the right panel of Fig. 2.1 but occurs at much greater pressures.) In the first scenario, the hot spot contains a vortex which surrounds a relatively static column of dry air extending into the interior; gradual downward motion conteracts upward mixing of volatiles and keeps the hot spot dry. Volatiles enter the downdraft by lateral mixing. If the hot spot has lower density than the surroundings, the mixed air — which always maintains its level of neutral buoyancy — will move down as it enters the hot spot. This will prevent lateral mixing from moistening the downdraft. Further, if air outside the hot spot has volatile abundances resembling the right panel of Fig. 2.1, air mixed into the hot spot will produce a pattern resembling the observations in the left panel of Fig. 2.1.

In the alternate scenario, the hot spot is a wave propagating relative to the flow. Air columns approach the hot spot from the west, elongate as they enter the hot spot, and contract as they exit only days later. The elongation process can explain the abundances of ammonia, H_2S, and water. The initial (pre-stretched) column matches Fig. 2.1 (right panel). As the stretching occurs, air which originated at 0.5, 2, and 5 bars, respectively, is deflected to 8, 16, and > 20 bars inside the hot spot; this explains the observations in Fig. 2.1 (left panel). The stable layer expected near 5 bars is also deflected to pressures exceeding 20 bars, where it prevents upward mixing of moist air into the hot spot.

3.4 Physical model and numerical methods

The qualitative scenarios described in Section 3.3 constitute hypotheses for the nature of hot spots; my goal is to test these scenarios by determining whether they

are dynamically possible. Although Jupiter's fluid layer extends extremely deep, a preferred model consists of a vertically thin, stably stratified upper layer overlying a deep interior. A statically stable layer below the clouds has been suggested by observational studies of atmospheric waves (Flasar and Gierasch 1986, Allison 1990, Ingersoll and Kanamori 1994) and would result naturally from latent heat release associated with condensation of water near 5 bars. By suppressing vertical motion, such a stable layer would restrict the cloud-level flow to be quasi-horizontal, confined to a shallow "weather layer" with vertical extent — and velocities — much smaller than horizontal ones.

I have adopted the simplest such model, a two layer model where the thin upper layer represents the weather layer and the deep lower layer represents the convectively adjusted, neutrally stratified deep interior. By assuming the motions in the lower layer are steady in time and the densities in each layer are constant, the system reduces to the shallow water equations for a single layer (Dowling and Ingersoll 1989; see also Pedlosky 1987, Chapter 3):

$$\frac{d\mathbf{v}}{dt} = -f\mathbf{k} \times \mathbf{v} - g\nabla H$$

$$\frac{dH}{dt} = -H\nabla \cdot \mathbf{v}$$

where $\mathbf{v}$ and H are the horizontal wind velocity and vertical thickness of the weather layer, g is gravitational acceleration times the fractional density difference between the layers, $\mathbf{k}$ is the unit vertical vector, $f = 2\Omega \sin\phi$ is the Coriolis parameter, Ω is the planetary rotation rate, ϕ is latitude, and d/dt is the derivative following the flow. An additional term can be added to the first equation to account for the (specified) pressure gradients in the deep layer. Because the lower layer dynamics are specified, this model is often called the "1-1/2 layer" model. It is the simplest form of an isopycnal model, which is particularly appropriate to Jupiter because of the long radiative time and absence of a solid surface. Such models have a long history of successful use in studies of jets and vortices on the giant planets (Ingersoll and Cuong

1981, Williams and Wilson 1988, Dowling and Ingersoll 1989, Marcus and Lee 1994, Cho and Polvani 1996, Le Beau et al. 1998).

I will solve the equations on a rotating sphere using a numerical code which implements the spectral transform method. The fields are represented as sums of spherical harmonics up to specified values of zonal wavenumber and degree. To evaluate the spectral coefficients of nonlinear terms in the equations, the code transforms the fields to physical space, evaluates the products on the physical grid, and tranforms the products back to spectral space (Washington and Parkinson 1986, p. 192). The equations are updated using either explicit or semi-implicit time stepping. The code includes an optional numerical hyperdiffusion term and an Asselin filter to maintain numerical stability. Over the past year, I have tested the code against a standard set of solutions designed for the purpose of evaluating shallow water models (Williamson et al. 1992) and performed preliminary simulations to explore vortex and jet interactions under jovian conditions. These runs were performed on the Cray T3D at the Jet Propulsion Laboratory. As an example, a 720-hour simulation at 1.4° resolution requires $\sim$ 1400 seconds of integration time (per processor) when run using 4 processors on the T3D. Such short integration times indicate that extensive explorations of parameter space will be feasible.

My procedure will be as follows. I will run many simulations using different initial configurations of equatorial vortices and waves, as well as different values of viscosity, resolution, and deformation radius. I will then search the solutions for structures resembling the scenarios outlined in Section 3.3. If such structures occur, I will test their robustness to changes in the parameters with the aim of understanding why they occur near the equator, why they appear in the northern rather than southern hemisphere, and why $\sim$ 10 hot spots are preferred. If no solutions resembling hot spots are found, however, it suggests that hot spot formation requires some process excluded from the model. Possibilities include vertical wind shear or the details of the vertical stability. In the future, I plan to carefully test the effect of these additional processes by extending the model to 64 vertical levels; my aim is to systematically isolate the mechanisms responsible for hot spots.

3.5 References

ACHTERBERG, R.K. AND A.P. INGERSOLL 1994. Numerical simulations of baroclinic jovian vortices. *J. Atmos. Sci.* **51,** 541-562.

ALLISON, M. 1990. Planetary waves in Jupiter's equatorial atmosphere. *Icarus* **83,** 282-307.

ATREYA, S. 1996. In *International Conference on the Shoemaker-Levy 9 Jupiter Collision,* p. 2, Observatoire de Paris.

CARLSON, B.E., A.A. LACIS, AND W.B. ROSSOW 1994. Belt-zone variations in the jovian cloud structure. *J. Geophys. Res.* **99,** 14,623-14,658.

CHO, J.Y-K. AND L.M. POLVANI 1996. The morphogenesis of bands and zonal winds in the atmospheres on the giant outer planets. *Science* **273,** 335-337.

DOWLING, T.E. AND A.P. INGERSOLL 1989. Jupiter's Great Red Spot as a shallow water system. *J. Atmos. Sci.* **46,** 3256-3278.

FLASAR, F.M. AND P.J. GIERASCH 1986. Mesoscale waves as a probe of Jupiter's deep atmosphere. *J. Atmos. Sci.* **43,** 2683-2707.

FOLKNER, W.M., R. WOO, AND S. NANDI 1998. Ammonia abundance in Jupiter's atmosphere derived from the attenuation of the Galileo probe's radio signal. Submitted to *J. Geophys. Res.*

INGERSOLL, A.P. AND P.G. CUONG 1981. Numerical model of long-lived jovian vortices. *J. Atmos. Sci.* **38,** 2067-2076.

INGERSOLL, A.P. AND H. KANAMORI 1994. Waves from the collisions of comet Shoemaker-Levy 9 with Jupiter. *Nature* **374,** 706-708.

LE BEAU, R.P. AND T.E. DOWLING 1998. EPIC simulations of time-dependent, Three-dimensional vortices with application to Neptune's Great Dark Spot. *Icarus* **132,** 239-265.

MARCUS, P.S. 1988. Numerical simulation of Jupiter's Great Red Spot. *Nature* **331,** 693-696.

MARCUS, P.S. AND C. LEE 1994. Jupiter's Great Red Spot and zonal winds as a self-consistent, one-layer, quasigeostrophic flow. *Chaos* **4,** 269-286.

NIEMANN, H.B. AND 11 COAUTHORS 1998. The composition of the jovian atmosphere as determined by the Galileo probe mass spectrometer. *J. Geophys. Res.*, in press.

ORTIZ, J.L, G.S. ORTON, S.T. STEWART, AND B.M. FISHER 1998. Evolution and persistence of 5-μm hot spots at the Galileo probe entry latitude. *J. Geophys. Res.*, in press.

ORTON, G. AND 40 COAUTHORS 1996. Earth-based observations of the Galileo Probe entry site. *Science* **272,** 839-840.

OWEN, T.C. AND 11 COAUTHORS 1996. *Eos* (spring suppl.), **77,** S171.

PEDLOSKY, J. 1987. *Geophysical Fluid Dynamics.* Springer-Verlag, New York.

SHOWMAN, A.P. AND A.P. INGERSOLL 1998. Interpretation of Galileo probe data and implications for Jupiter's dry downdrafts. *Icarus* **132,** 205-220.

VASAVADA, A.R. AND 12 COAUTHORS 1997. Galileo imaging of Jupiter's atmosphere: the great red spot, equatorial region and white ovals. *Icarus*, in press.

WASHINGTON, W.M. AND C.L. PARKINSON 1986. *An introduction to Three-Dimensional Climate Modeling.* Oxford Univ. Press, New York.

WILLIAMS, G.P. AND R.J. WILSON 1988. The stability and genesis of Rossby vortices. *J. Atmos. Sci.* **45,** 207-241.

WILLIAMSON, D.L., J.B. DRAKE, J.J. HACK, R. JAKOB, AND P.N. SWARZTRAUBER 1992. A standard test set for numerical approximations to the shallow water equations in spherical geometry. *J. Comp. Phys.* **102,** 211-224.

Chapter 4

Tidal evolution into the Laplace resonance and the resurfacing of Ganymede

4.1 Abstract

We use the numerical model of Malhotra (1991) to explore the orbital history of Io, Europa, and Ganymede for a large range of parameters and initial conditions near the Laplace resonance. We identify two new Laplace-like resonances which pump Ganymede's eccentricity and may help explain the resurfacing of Ganymede. Near the Laplace resonance, the Io-Europa conjunction drifts at a mean angular velocity $\omega_1 \equiv 2n_2 - n_1$, while the Europa-Ganymede conjunction drifts at a rate $\omega_2 \equiv 2n_3 - n_2$, where n_1, n_2, and n_3 are the mean motions of Io, Europa, and Ganymede. We find that Laplace-like resonances characterized by $\omega_1/\omega_2 \approx 3/2$ and $\omega_1/\omega_2 \approx 2$ can pump Ganymede's eccentricity to ~ 0.07, producing tidal heating several hundred times higher than at the present epoch, and 2-30 times greater than that occurring in the $\omega_1/\omega_2 \approx 1/2$ resonance identified previously by Malhotra (1991). The evolution of ω_1 and ω_2 prior to capture is strongly affected by Q'_{Io}/Q'_J. (Here, $Q' = Q/k$ is the ratio of the tidal dissipation function to second degree Love number; the subscript J is for Jupiter.) We find that capture into $\omega_1/\omega_2 \approx 3/2$ or 2 occurs over a large range of possible initial satellite orbits if $Q'_{Io}/Q'_J \leq 4 \times 10^{-4}$, but cannot occur for values $\geq 8 \times 10^{-4}$. (The latter is approximately two-thirds the value required to maintain Io's current eccentricity in steady state.) For constant Q/k, the system, once captured, remains trapped in these resonances. However, we show that they can be disrupted by rapid changes in the tidal dissipation rate in Io or Europa during the course of the evolution; the satellites subsequently evolve into the Laplace resonance ($\omega_1 = \omega_2$)

with high probability. Because the higher dissipation in these resonances increases the likelihood of internal activity within Ganymede, we favor the $\omega_1/\omega_2 \approx 3/2$ and 2 resonances over $\omega_1/\omega_2 \approx 1/2$ for the evolutionary path taken by the Galilean satellites before their capture into the Laplace resonance.

In addition to its surface appearance, Ganymede's large free eccentricity (0.0015) has long been a puzzle. We find that the $\omega_1/\omega_2 \approx 3/2$ and $\omega_1/\omega_2 \approx 2$ resonances can pump Ganymede's free eccentricity up to $\sim 10^{-3}$ independent of Q'_{Gany}/Q'_J. We also show that Ganymede's free eccentricity cannot have been produced by impact with a large asteroid or comet.

4.2 Introduction

The orbital resonances among the jovian moons Io, Europa, and Ganymede present a fascinating dynamical system. The strongest resonant interactions are those between Io and Europa and between Europa and Ganymede. The ratios of mean motions (i.e., mean orbital angular velocities) of these satellite pairs are both near 2:1, causing their successive conjunctions to occur near the same jovicentric longitude. This allows their mutual gravitational perturbations to add constructively, and, as we shall see later, allows a secular transfer of energy and angular momentum from Io to Europa to Ganymede.

As the ratio of mean motions is not exactly 2:1, the conjunctions between Io and Europa drift at a mean angular velocity $\omega_1 \equiv 2n_2 - n_1$, while the conjunctions between Europa and Ganymede drift at a rate $\omega_2 \equiv 2n_3 - n_2$, where n_1, n_2, and n_3 are the mean motions of Io, Europa, and Ganymede. The Io-Europa conjunction is locked to Io's perijove and also to Europa's apojove; the Europa-Ganymede conjunction occurs when Europa is near perijove. These pairwise resonances are described by the libration of the following resonance angles:

$$\theta_{11} = 2\lambda_2 - \lambda_1 - \varpi_1 \quad \text{librates about } 0^\circ$$

$$\theta_{12} = 2\lambda_2 - \lambda_1 - \varpi_2 \quad \text{librates about } 180°$$

$$\theta_{23} = 2\lambda_3 - \lambda_2 - \varpi_2 \quad \text{librates about } 0°$$

where λ_i and ϖ_i are the satellites' mean longitudes and longitudes of perijove. In this paper, all subscripts $i = 1$, 2, or 3 refer to Io, Europa, or Ganymede, respectively, unless stated otherwise. (The Europa-Ganymede conjunction is not locked to either apse of Ganymede, so the other possible resonant variable, $2\lambda_3 - \lambda_2 - \varpi_3$, circulates through all possible values.) The fourth major resonance — the Laplace resonance — is characterized by the libration of the following critical angle:

$$\phi = 2\lambda_3 - 3\lambda_2 + \lambda_1, \quad \text{librates about } 180°$$

The Laplace resonance is a 1:1 commensurability between the rates of motion of the Io-Europa and Europa-Ganymede *conjunctions* (as opposed to the 2:1 commensurabilities between the satellites' *mean motions*): the Io-Europa conjunction drifts at the same rate as the Europa-Ganymede conjunction, so that $\omega_1/\omega_2 = 1$. Currently we have $\omega_1 = \omega_2 = -0.74°\text{day}^{-1}$. This is an extremely small value compared to the satellites' mean motions which range from approximately $50°\text{day}^{-1}$ for Ganymede to approximately $200°\text{day}^{-1}$ for Io.

These orbital resonances have a strong effect on the satellites' thermal evolution. Io's active volcanism and high thermal heat flux of $\sim 2\,\text{W}\,\text{m}^{-2}$ (Smith et al. 1979, Veeder et al. 1994) are probably caused by tidal dissipation associated with its resonantly forced orbital eccentricity of 0.0044 (Peale et al. 1979). Europa's tectonism possibly also results from tidal flexing (Malin and Pieri 1986). Although Ganymede's eccentricity is currently too low for significant tidal heating, the ancient resurfacing on this satellite (McKinnon and Parmentier 1986) may be linked to higher tidal dissipation in the past. Especially for Ganymede, knowledge of past orbital history is critical for elucidating the thermal evolution.

Yoder (1979) and Yoder and Peale (1981) constructed an analytic theory to explain the high rate of internal activity on Io as well as the origin of the Laplace

resonance from initially non-resonant orbits. According to this scenario, tides raised on Jupiter by the satellites cause the satellite orbits to expand outward over time. As Io approaches the 2:1 resonance with Europa, ω_1 approaches zero, forcing Io's eccentricity, e_1, to increase. However, tidal dissipation in Io (which increases with e_1) lowers Io's semi-major axis and eccentricity. This counteracts the effects of Jupiter's tides which push Io outward into 2:1 resonance with Europa, as well as the resonant gravitational perturbations from Europa which pump Io's eccentricity. Thus, an equilibrium characterized by constant values of ω_1 and e_1 is achieved, and the orbits of Io and Europa expand together while being locked in resonance. (This involves a secular transfer of orbital angular momentum from Io to Europa.) The equilibrium values of ω_1 and e_1 estimated by Yoder and Peale are $-1.2°$ day^{-1} and 0.0026, respectively. However, this is a metastable state as Europa approaches the 2:1 resonance with Ganymede and the Europa-Ganymede resonant perturbations become significant. During this evolution, ω_2 approaches ω_1 and the satellites are captured into the Laplace resonance. Yoder and Peale calculate that the capture probability is high provided $|\omega_1|, |\omega_2| \leq 2°$ day^{-1}. As Jupiter's tides continue to transfer angular momentum to the satellites (primarily Io), the Laplace resonance forces a secular transfer of orbital angular momentum from Io to Europa to Ganymede. A new equilibrium is reached in which ω_1 stabilizes at a new value, and the resonantly forced eccentricities of all three satellites also reach constant values. If the present state of the system is at this equilibrium, this theory predicts $Q_1'/Q_J' \approx 1.1 \times 10^{-3}$. (Here $Q' \equiv Q/k$ is the ratio of the tidal dissipation function to the second degree Love number, and subscript J refers to Jupiter.) Ganymede's eccentricity remains low in this scenario.

A second scenario was outlined by Greenberg (1982, 1987). He noted that the Yoder-Peale scenario was predicated on significant tidal dissipation within Jupiter, at a rate greater than any known physical mechanisms for tidal dissipation in gaseous planets. To circumvent this apparent difficulty, he suggested that Io, Europa, and Ganymede formed in orbits deep in resonance, with ω_1 and ω_2 closer to zero. Since satellite formation, dissipation in Io has decreased the satellite's semi-major axis

and increased $|\omega_1|$; thus, Io has evolved away from the 2:1 resonance with Europa. Similarly, Europa and Ganymede were deeper in the 2:1 resonance in the past, so that Ganymede would have had a higher forced eccentricity. This scenario allows slightly more tidal heating in Ganymede than at present (eccentricity ~ 0.003, as compared with the current free and forced eccentricities of 0.0015 and 6×10^{-4}). However, recent theoretical work on the tidal Q of gaseous planets (Ioannou and Lindzen 1993) and estimates of low upper bounds for the tidal Q of other outer planets ($Q < 39,000$ for Uranus [Tittemore and Wisdom 1989] and $Q < 3 \times 10^5$ for Neptune [Banfield and Murray 1992]) suggest than Q_J was low enough for significant orbital evolution, increasing the plausibility of the tidal assembly of the Galilean resonances.

Greenberg (1982) has also suggested the possibility of episodic tidal heating of Io, in which the Galilean satellites oscillate about the equilibrium point of the Laplace resonance, causing Io's Q' and resonantly forced eccentricity to vary periodically. This possibility was explored in some detail in Ojakangas and Stevenson (1986), and it remains a viable model for the present state of the system. However, it has not been shown to have significant import for Ganymede's evolution.

More recently, Malhotra (1991) showed that the evolutionary path described by the Yoder-Peale theory for the tidal assembly of the resonances is not unique. She found that for a wide range of initial conditions, the satellites would have encountered and been temporarily captured in one or more "Laplace-like" resonances $\omega_1/\omega_2 \approx j/(j+1)$, $j = 1$, 2, or 3, before evolving into the present state. (We define a "Laplace-like" resonance to be one in which the ratio of the mean conjunction drift rates, ω_1/ω_2, is that of two small positive integers.) Capture into any of these three resonances can occur at relatively high values of $|\omega_1|$ and $|\omega_2|$ ($\sim 7 - 8°\text{day}^{-1}$, before either pairwise resonance has achieved equilibrium), and is fairly likely. The 2:1 mean motion resonances then evolve in concert during passage through one of these Laplace-like resonances, as ω_1 and ω_2 continue to approach zero. At sufficiently small values of $|\omega_1|$ and $|\omega_2|$, the $\omega_1/\omega_2 \approx j/(j+1)$ resonance is disrupted and the satellites are captured into the Laplace resonance. Of potentially great significance for Ganymede was the discovery that the $\omega_1/\omega_2 \approx 1/2$ resonance pumps Ganymede's eccentricity

up to $\sim 0.01 - 0.03$, possibly enough for internal activity and consequent resurfacing.

For completeness, we mention here Tittemore's (1990) proposal for the tidal heating of Ganymede. In this scenario, Europa and Ganymede pass through the pairwise 3:1 mean motion resonance which chaotically pumps up their orbital eccentricities to large values ($e_{2,\max} \approx 0.13$, $e_{3,\max} \approx 0.06$) before the satellites eventually disengage from that resonance. (They are presumed to subsequently evolve to their present 2:1 resonant orbits). Tittemore argued that the extent of orbital evolution of Europa and Ganymede required in this scenario can be accommodated provided Io and Europa were locked in the pairwise 2:1 resonance early on. Tittemore's numerical modeling of the Europa-Ganymede 3:1 resonance passage did not include the 2:1 resonant perturbations of the Io-Europa interaction, and also neglected tidal dissipation within the satellites, both factors that significantly affect the dynamical evolution of the system. It is possible to overcome these deficiencies and it would be worth re-evaluating the 3:1 Europa-Ganymede resonance with a more complete numerical model. However, such a study is beyond the scope of the present work. We do not discuss this scenario further because it does not speak to the evolution of the satellites near the Laplace resonance.

The three scenarios of Yoder and Peale, Greenberg, and Malhotra are best visualized by plotting the system's path in $\omega_1 - \omega_2$ space. This will also prove useful for discussing our results. In Fig. 4.1 we depict the paths just discussed. The initial position in $\omega_1 - \omega_2$ space after satellite formation is completely unknown. (This position is related to the initial orbital semi-major axes of the satellites.) Consider the tidal assembly scenarios. Far from equilibrium of the pairwise 2:1 resonances and in the absence of any Laplace-like resonances, Io's orbit expands much more rapidly than Europa's, so ω_1 increases faster than ω_2. Starting from its initial position, the system thus moves nearly horizontally to the right in $\omega_1 - \omega_2$ space. In the Yoder-Peale scenario, the system evolves unhindered by any Laplace-like resonance to equilibration of the Io-Europa resonance, and ω_1 becomes constant (dash-dot line). As ω_2 continues to increase, the system then moves vertically upward in $\omega_1 - \omega_2$ space. Capture into the Laplace resonance, $\omega_1/\omega_2 = 1$, eventually occurs from below, i.e.,

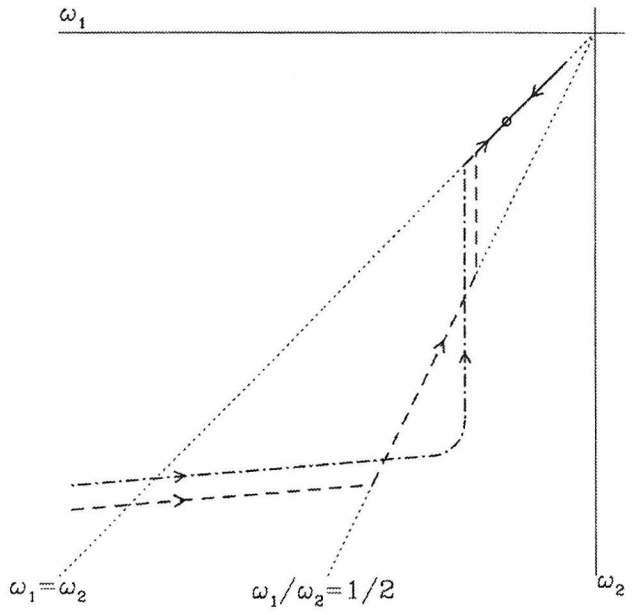

Figure 4.1: Several possible paths to the current state as proposed by previous authors, shown in $\omega_1 - \omega_2$ space. The current position is marked by a circle; the Laplace resonance, $\omega_1/\omega_2 = 1$, and the Laplace-like resonance, $\omega_1/\omega_2 \approx 1/2$, are shown in dotted lines. (Dot-dashed line) Yoder and Peale (1981) scenario in which the Io-Europa 2:1 resonance equilibrates before capture into the Laplace resonance; (Dashed line) Malhotra (1991) scenario for passage through $\omega_1/\omega_2 \approx 1/2$ prior to capture into the Laplace resonance. (Short solid line moving downward from near the origin) Greenberg (1987) scenario in which tidal dissipation in Jupiter is negligible.

from a smaller value of ω_1/ω_2. In contrast, Malhotra (1991) showed that the first metastable state in Yoder and Peale's scenario was unlikely to be achieved as there was a high probability that the approach to this state would be interrupted by capture into a $\omega_1/\omega_2 = j/(j+1)$ Laplace-like resonance. This is shown by the dashed line. Greenberg's scenario is shown with a solid line.

In this paper we use Malhotra's (1991) numerical model to explore evolution into the Laplace resonance over a much wider range of conditions than she examined. Our main finding is that two other Laplace-like resonances *above* the Laplace resonance, $\omega_1/\omega_2 \approx 2$ and $\omega_1/\omega_2 \approx 3/2$, have high capture probability and can pump Ganymede's eccentricity to ~ 0.07. Capture into these resonances is possible only if $Q_1'/Q_J' < 8 \times 10^{-4}$. (This upper bound is slightly smaller than the value needed to maintain the current orbital configuration in steady state, as discussed in Yoder and Peale, 1981.) If this condition is satisfied, capture into one of these resonances is quite likely. We also find that if the Q/k are constant in time, the satellites do not evolve into the Laplace resonance from these resonances. We show that rapid changes in Q_1'/Q_J' or Q_2'/Q_J' can cause disruption followed by capture into the Laplace resonance. Several plausible mechanisms can easily produce the requisite time variability in Q_i'/Q_J'.

The paper is organized as follows. In Section 4.3 we present our results. We begin with a brief description of the dynamical model. This is followed by a detailed description of some example runs. Next, we identify the conditions under which capture into $\omega_1/\omega_2 \approx 3/2$ or $\omega_1/\omega_2 \approx 2$ can occur, and we characterize the resonances by determining the eccentricities and dissipated power they produce under different conditions. We then explore the manner in which Q_1'/Q_J' or Q_2'/Q_J' must change to allow disruption of these new Laplace-like resonances and evolution into the Laplace resonance. We end the section with some additional results on the evolution of ω_1 and ω_2 toward equilibrium. In Section 4.4 we calculate the size of the cometary impactor necessary to excite Ganymede's free eccentricity to its current value (0.0015); we show that the free eccentricity cannot have been produced by cometary impact. In Section 4.5 we summarize our results and conclusions. Implications for Ganymede's thermal history are discussed in a companion paper.

4.3 Results

4.3.1 The model

The dynamical model we use is described in detail in Malhotra (1991). The model includes perturbations from Jupiter's gravity field to order J_4 and the mutual satellite perturbations to second order in the orbital eccentricities. The secular perturbations due to Callisto are also included. The effects of tidal dissipation in the planet as well as the satellites are parameterized by the tidal dissipation functions, Q_J, Q_i, and are included in the perturbation equations. The ratios Q_i'/Q_J' are free parameters which we specify as inputs to the model.

The differential equations are approximated by an algebraic mapping (details given in Malhotra, 1991). This speeds up the numerical simulation by a factor of several hundred. Even so, it is necessary to artificially enhance the rate of orbital evolution in order to obtain results within reasonable computational time. We used $Q_J = 100$ in all our runs. (The Q_i'/Q_J' are independently specified free parameters.) A typical run uses ~ 8 hours of CPU time on an HP-735/99Mhz workstation. To illustrate, suppose the "real" value of Q_J is 10^5; then, using $Q_J = 100$ in the numerical simulation means that the entire evolution over the 4.5 billion year age of the system is forced to occur over only 4.5 million years. Nevertheless, we expect that the qualitative features of the dynamics are not affected because tidal evolution with $Q_J = 100$ is slow enough to be adiabatic on the timescale of the gravitational perturbations. Quantitative confirmation of this assumption is discussed in Section 4.3.5.

We note here that the model accounts for only the low frequency resonant perturbations, so is valid only for sufficiently small $|\omega_1|$ and $|\omega_2|$. We restrict our calculations to $|\omega_1|, |\omega_2| < 10°\text{day}^{-1}$. Although this range corresponds to only a few percent change in a_1/a_2 and a_2/a_3, it is comparable to the extent of evolution expected over solar system history for reasonable Q_J values ($\sim 10^5$). The satellites may thus have formed in the region of validity of the model for ω_1 and ω_2.

For most of the simulations discussed in this paper, Ganymede's initial eccentricity was 0.001. Resonance encounter usually occurred (when at all) with an eccentricity

somewhat smaller than the initial value.

4.3.2 Example runs

In this section, we describe in detail the evolution of the system in three different runs. These illustrate the range of possible orbital and dynamical histories of the Galilean satellites that we have found in more than 200 numerical simulations. The time evolution of several parameters in these runs is plotted in Figs. 4.2, 4.3 and 4.4. Panels (a), (b), and (c) in these figures depict the evolution of the orbital eccentricities of Io, Europa, and Ganymede; panel (d) shows the ratio ω_1/ω_2, and (e) shows our assumed Q'_1/Q'_J. The time axis runs from 0 to $1.3 \times 10^4 Q_J$ years (assuming $k_J = 0.38$, following Gavrilov and Zharkov 1977). (In displaying the results of our simulations, we have factored out Q_J on the time axis. This stresses the fact that Q_J is unknown and that, for a given simulation with specified Q'_i/Q'_J over time, the timescale for the evolution scales linearly with Q_J.) Thus, the evolution shown in these figures would occur in 4 billion years if $Q_J = 3 \times 10^5$, but only 400 million years if $Q_J = 3 \times 10^4$. There is no special significance to the origin on the time axis. Note that the end state of the system in each of these runs is close to that observed at the present epoch: the satellites are trapped in the Laplace resonance, and the final orbital eccentricities are close to the observed forced eccentricities. The three runs differ in initial conditions and in the assumed tidal dissipation functions. Consequently, the runs differ in the sequence of Laplace-like resonances that the satellites encounter and temporarily enter before reaching the current state.

The initial values of the frequencies (ω_1, ω_2) in Figs. 4.2, 4.3 and 4.4 were $(-5.6, -3.2)$, $(-6.2, -2.6)$, and $(-4.7, -8.0)$ degrees per day, respectively. All three runs begin with $Q'_1/Q'_J = 4 \times 10^{-4}$. (Other parameter values are listed in the captions.) We also show the evolution for these runs on a $\omega_1 - \omega_2$ plot in Fig. 4.5. In Figs. 4.2 and 4.3, the initial value of ω_1/ω_2 is greater than 1, whereas in Fig. 4.4 it is less than 1. In all three cases, ω_1 and ω_2 both increase toward zero over time, but ω_1 increases more rapidly, so ω_1/ω_2 initially decreases.

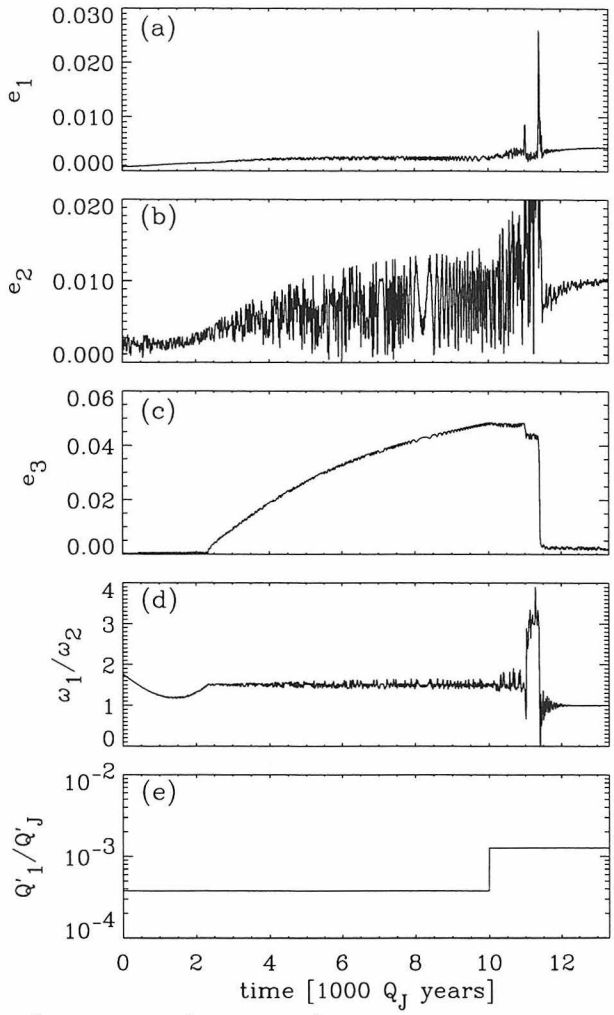

Figure 4.2: The first example run: the system was temporarily captured in the $\omega_1/\omega_2 \approx 3/2$ resonance before evolving into the Laplace resonance. Shown are time evolution of the eccentricities of (a) Io, (b) Europa, and (c) Ganymede, and (d) the ratio ω_1/ω_2; panel (e) shows the assumed Q_1'/Q_J' over time. The time axes in (a)-(e) are the same and run from 0 to $1.3 \times 10^4 Q_J$ years. In this run, the ratios of the tidal dissipation functions, Q_1'/Q_J' ($Q' \equiv Q/k$), were $Q_3'/Q_J' = 0.127$ and $Q_2'/Q_J' = 4.1 \times 10^{-3}$; Q_1'/Q_J' was initially set to 4×10^{-4} and was changed at time $10^4 Q_J$ years to 1.27×10^{-3}, which caused the system to jump from $\omega_1/\omega_2 \approx 3/2$ into the Laplace resonance ($\omega_1 = \omega_2$) after rapid fluctuation of the variables. The state of the system at the end of the integration is close to that observed at present.

In Fig. 4.2, ω_1/ω_2 initially passes through 3/2 from above without entering this resonance. The rate of change of ω_1 decreases, and at some point ω_1 becomes almost constant at a value near -2.5 to $-3.0°\text{day}^{-1}$ (see Fig. 4.5). (As in the Yoder-Peale scenario, competition between the effects of Jupiter's and Io's tides causes this effect, but here it occurs at a larger value of $|\omega_1|$ because Q_1'/Q_J' is one-third that in the Yoder-Peale scenario.) However, ω_2 continues to increase, so ω_1/ω_2 reverses direction and begins climbing. When $\omega_1/\omega_2 = 3/2$ is reached *from below*, resonance capture occurs. The resonance excites Ganymede's orbital eccentricity, and also causes large variations in Europa's eccentricity. ω_1 and ω_2 continue to increase, and a new equilibrium is reached. At time $t = 10^4 Q_J$ years, we abruptly increase Q_1'/Q_J' to 1.2×10^{-3}. This change destabilizes the $\omega_1/\omega_2 \approx 3/2$ resonance: a short time ($\sim 10^3 Q_J$ years) later, the orbital parameters exhibit large fluctuations and the satellites enter the Laplace resonance ($\omega_1 = \omega_2$).

The evolution in Fig. 4.3 is qualitatively similar to that in Fig. 4.2: ω_1/ω_2 initially decreases, minimizes, and then increases. The value of ω_1 at the minimum is roughly the same as in Fig. 4.2 (see Fig. 4.5). However, because we started with a greater initial value of ω_2, the minimum occurs at $\omega_1/\omega_2 > 3/2$ in Fig. 4.3, rather than at $\omega_1/\omega_2 < 3/2$ as in Fig. 4.2. Thus, in this case, the system never encounters the $\omega_1/\omega_2 = 3/2$ resonance. When ω_1/ω_2 approaches the value 2, the satellites are captured in this Laplace-like resonance. (Note again that this resonance capture occurs from *below*; the early encounter of ω_1/ω_2 with the value 2 *from above* did not result in resonance capture.) This resonance also pumps up Ganymede's eccentricity. At $t = 10^4 Q_J$ years, we change Q_1'/Q_J' to 2.5×10^{-3}, and the system jumps into the Laplace resonance.

In our third example, shown in Fig. 4.4, the system first enters the $\omega_1/\omega_2 \approx 1/2$ Laplace-like resonance. However, this resonance is soon disrupted, and ω_1/ω_2 increases past 1 (without entering the Laplace resonance), and is next captured into the $\omega_1/\omega_2 \approx 3/2$ resonance. When we change Q_1'/Q_J' to 1.2×10^{-3} at time at $t = 10^4\, Q_J$ years, the system jumps into the Laplace resonance. In this example there are *two* eccentricity pumping episodes, one for $\omega_1/\omega_2 \approx 1/2$ and one for $\omega_1/\omega_2 \approx 3/2$. If

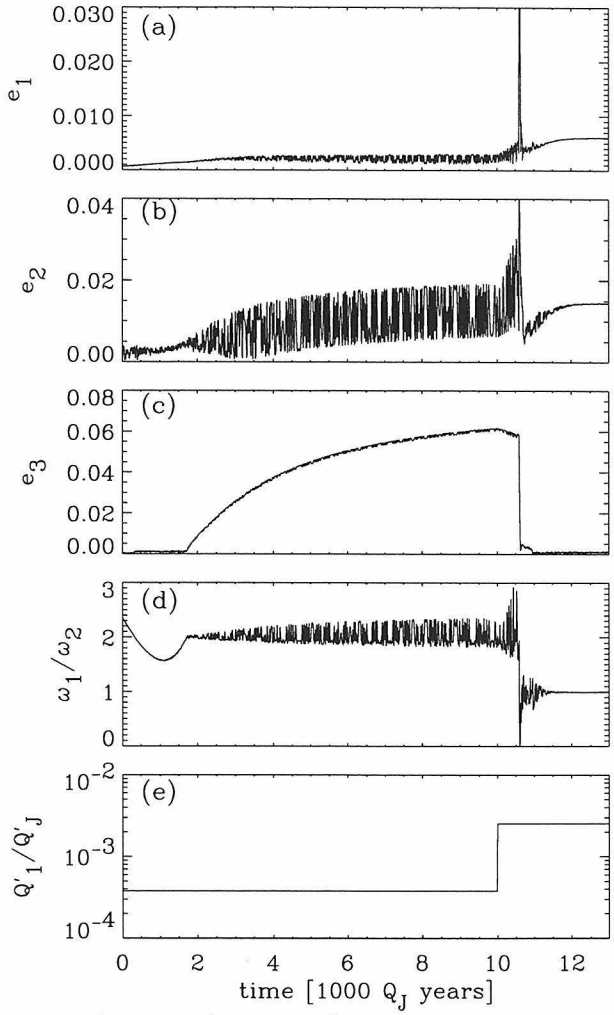

Figure 4.3: The second example run: the system was temporarily captured in the $\omega_1/\omega_2 \approx 2$ resonance before reaching the current configuration. All panels are the same as in Fig. 4.2. The tidal parameters Q'_i/Q'_J are the same as for Fig. 4.2, except that at $10^4 Q_J$ years, Q'_1/Q'_J was changed to 1.9×10^{-3}. This change disrupted the $\omega_1/\omega_2 \approx 2$ resonance and allowed capture into the Laplace resonance.

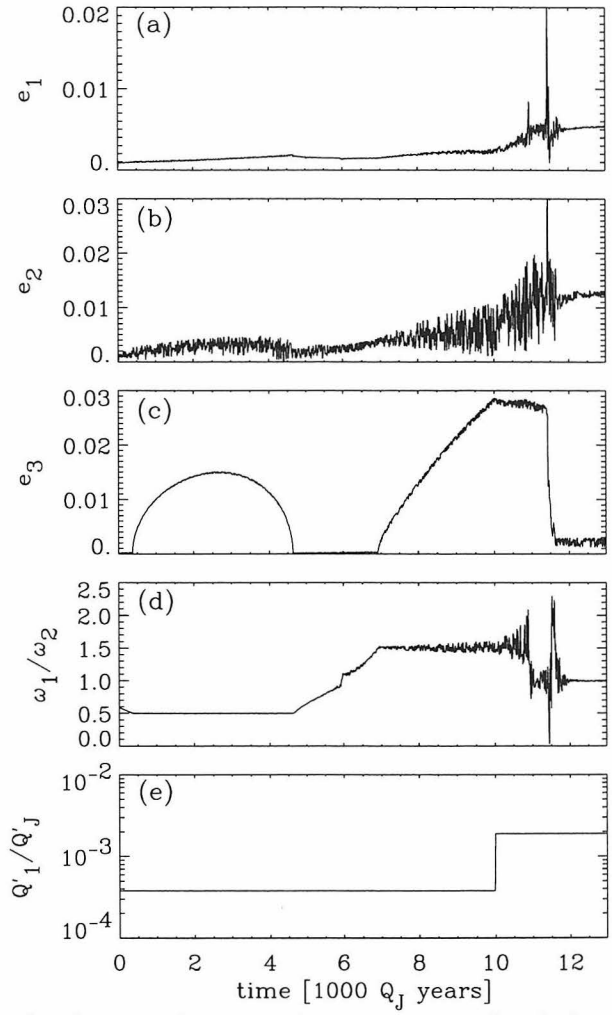

Figure 4.4: The third example run: the system evolved through both the $\omega_1/\omega_2 \approx 1/2$ and $\omega_1/\omega_2 \approx 3/2$ resonances in this run. All panels are the same as in Figs. 4.2 and 4.3. The ratios of tidal Q'_i/Q'_J are exactly the same as those used in Fig. 4.2, including the change in Q'_1/Q'_J to 1.27×10^{-3} at $10^4 Q_J$ years. The main differences are the initial values of ω_1 and ω_2.

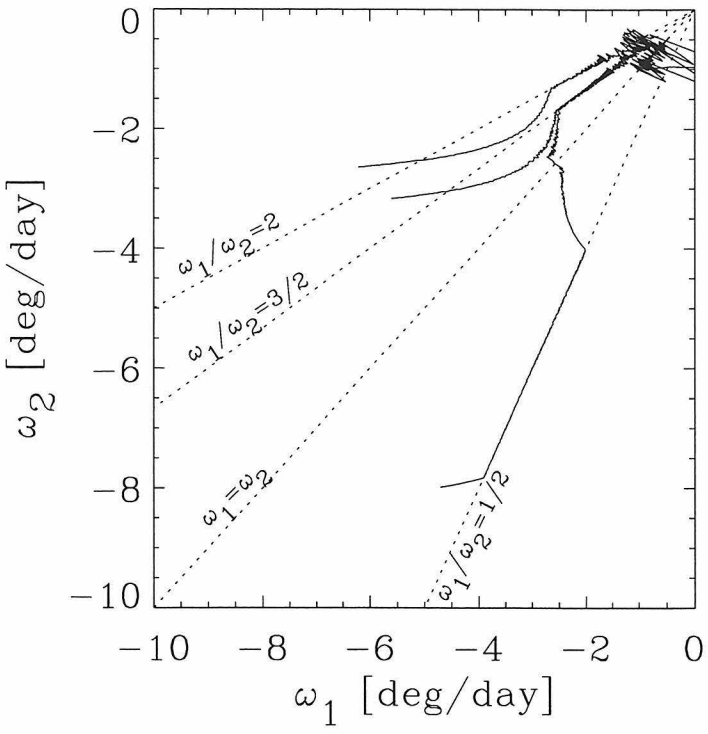

Figure 4.5: The paths of the system in the three example runs of Figs. 4.2–4.4 are displayed on an $\omega_1 - \omega_2$ diagram. Note that all three paths change to high slope at $\omega_1 \approx -3°\text{day}^{-1}$.

resurfacing is associated with each episode, two resurfacing events would occur.

Evolutionary paths as shown in Figs. 4.2, 4.3, and 4.4 represent plausible paths to the current state: in all three cases the system ends in the Laplace resonance. However, this has occurred only because we increased Q_1'/Q_J' by a factor of ~ 3 during each run; we will see later that decreasing Q_2'/Q_J' by a factor of ~ 100 also leads to disruption. Superficially, the discrete changes we make in the tidal Q's in these numerical experiments may appear artificial to the reader. However, despite the fact that most analytical orbital modeling assumes constant Q, time variability of Q_1'/Q_J' and Q_2'/Q_J is very likely. Indeed, the high Ionian heat flow measured by Veeder et al. (1994) may *require* time variable Q_1'/Q_J', given the lower bound on the time-averaged Q_J (Goldreich and Soter 1966, Yoder and Peale 1981). Furthermore,

laboratory experiments have shown that terrestrial rocks have strongly temperature dependent Q at high frequencies (Berckhemer et al. 1982). Although data at low frequencies are lacking, it is reasonable to expect temperature dependence at tidal frequencies also, especially at temperatures near the solidus. In addition, Io's and Europa's second degree Love numbers depend on satellite structure: they are near ~ 0.02 for a frozen interior but close to ~ 1 for a massively molten interior. Changes in satellite internal temperature or structure could thus cause large variations in Q_i'. Finally, processes may act in Jupiter to produce changes in Q_J (e.g., Stevenson 1983, Ioannou and Lindzen 1993), possibly of large amplitude. Any of these mechanisms could produce time variable Q_i'/Q_J' and may allow disruption of the $\omega_1/\omega_2 \approx 2$ or $\omega_1/\omega_2 \approx 3/2$ Laplace-like resonances followed by capture into the Laplace resonance.

When Q_1'/Q_J' oscillates (as a sinusoid or square wave) with periods of $\sim 10^8 - 10^9$ years and amplitudes comparable to that used in Figs. 4.2-4.4, the Laplace-like resonances are generally disrupted near a maximum in the cycle (not necessarily the first). However, subsequent minima of Q_1'/Q_J' do not cause a second resonance capture into the Laplace-like resonance — the system generally remains in the Laplace resonance itself. The Greenberg (1982)/Ojakangas and Stevenson (1986) model, in which the coupling between orbital dynamics and geophysics drives oscillation in Q_1'/Q_J', thus constitutes a plausible mechanism for disruption of the $\omega_1/\omega_2 \approx 3/2$ or 2 resonance and capture into the Laplace resonance.

4.3.3 Capture statistics for the $\omega_1/\omega_2 \approx 3/2$ and $\omega_1/\omega_2 \approx 2$ resonances

We have seen that the $\omega_1/\omega_2 \approx 3/2$ and $\omega_1/\omega_2 \approx 2$ Laplace-like resonances excite Ganymede's eccentricity to sufficiently high values that the consequent enhanced tidal heating could be geophysically significant. In order to estimate the viability of this scenario, we have to consider two issues: (1) What are the capture probabilities for $\omega_1/\omega_2 \approx 3/2$ and 2 resonances *assuming* they are encountered, and (2) What conditions allow ω_1 and ω_2 to evolve in such a manner that the resonances are encountered?

To answer these questions, we made many numerical simulations with a large range of initial conditions. Our study used values of ω_1 ranging from -9 to $-2°\text{day}^{-1}$ and of ω_2 ranging from -8 to $-1°\text{day}^{-1}$, with initial ω_1/ω_2 ranging from $0.2-3.1$. We used a variety of Q_1'/Q_J' values and Q_3'/Q_J' values. Most runs used $Q_2'/Q_J' = 4\times10^{-3}$ (which implies $Q_2 = 100$ for $k_2 = 0.03$, $Q_J = 3\times10^5$, and $k_J = 0.38$); in a few runs we varied Q_2'/Q_J by factors of ~ 2. The Q_i'/Q_J' are constant in time for all runs discussed in this subsection. First consider capture probabilities. Of 88 runs encountering $\omega_1/\omega_2 \approx 3/2$ from above, none was captured. However, of 64 runs encountering $\omega_1/\omega_2 \approx 3/2$ from below, 60 were captured. For the $\omega_1/\omega_2 \approx 2$ resonance, 0 of 36 runs were captured from above and 35 of 37 were captured from below. Thus, for both resonances, capture probabilities from below are very high, but capture from above apparently cannot occur. This behavior contrasts with that of the $\omega_1/\omega_2 \approx 1/2$, 2/3, and 3/4 resonances, for which capture occurs from above (Malhotra 1991). This also differs from the Laplace resonance, for which capture from either above or below can easily occur. The runs encountering these resonances from above use $Q_1'/Q_J' = (6\text{–}400)\times10^{-5}$, while those from below use $Q_1'/Q_J' = (6\text{–}80)\times10^{-5}$. We noticed no dependence of capture probability on Q_1'/Q_J within that range.

Next consider conditions leading to resonance encounter. From a wide variety of initial ω_1 and ω_2, capture into $\omega_1/\omega_2 \approx 3/2$ or 2 occurs commonly for $Q_1'/Q_J' \leq$ few $\times\, 10^{-4}$, but never for $Q_1'/Q_J' \approx 10^{-3}$. This phenomenon results not from a different capture probability at higher Q_1'/Q_J' but because the resonances are never encountered from below for these large values. The runs displayed in Figs. 4.2, 4.3, and 4.4 suggest an explanation for this phenomenon, which we have confirmed with another ~ 100 runs. As described by the Yoder and Peale (1981) scenario, ω_1 initially increases much faster than ω_2, so the system moves almost horizontally (with low positive slope) across the $\omega_1 - \omega_2$ plot. Eventually, ω_1 achieves equilibrium while ω_2 continues to increase, so ω_1/ω_2 minimizes and begins increasing, and the slope turns toward vertical (i.e., high positive slope). If $Q_1'/Q_J' \approx 10^{-3}$, as assumed by Yoder and Peale (1981), this happens at $\omega_1 \approx -1.2°\text{day}^{-1}$, as shown in Fig. 4.1. Unless ω_2 is very close to zero, the minimum occurs at $\omega_1/\omega_2 < 1$, so that the system encounters

the Laplace resonance before encountering $\omega_1/\omega_2 \approx 3/2$ or 2 from below. At these low values of $|\omega_1|$ and $|\omega_2|$, capture into the Laplace resonance is assured (Yoder and Peale 1981), so entry into $\omega_1/\omega_2 \approx 3/2$ or 2 cannot occur.

However, when Q_1'/Q_J' is lower, the equilibrium value of ω_1 is more negative. This phenomenon has two effects which favor capture into $\omega_1/\omega_2 \approx 3/2$ or 2. First, for given initial ω_1 and ω_2, equilibration occurs at larger values of ω_1/ω_2 than is possible for greater Q_1'/Q_J'. Thus, some runs minimize at ω_1/ω_2 *greater* than 1, which is essentially impossible at $Q_1'/Q_J' \approx 10^{-3}$. These runs will never encounter the Laplace resonance, and will therefore be captured into $\omega_1/\omega_2 \approx 3/2$ or 2 with near unit probability if the minimum value of ω_1/ω_2 is between 1 and 2. The fraction of initial ω_1 and ω_2 values for which such assured capture occurs increases with decreasing Q_1'/Q_J'. Second, scenarios which encounter the Laplace resonance from below do so at larger negative values of ω_1, for which capture into the Laplace resonance is unlikely (Yoder and Peale 1981). There is thus a significant probability that the system will not enter the resonance, but instead that ω_1/ω_2 will continue to increase. The system will then be captured into $\omega_1/\omega_2 \approx 3/2$ or 2 with high probability. Our simulations confirm this picture. Of the 27 runs which minimize at $\omega_1/\omega_2 < 1$ (for $Q_1'/Q_J' \approx 4 \times 10^{-4}$), 11 entered $\omega_1/\omega_2 = 3/2$ and 16 entered the Laplace resonance. (The run shown in Fig. 4.4 is one of the 11 that entered $\omega_1/\omega_2 \approx 3/2$.) These runs encountered the Laplace resonance at ω_1 and ω_2 between -3 and $-4°\text{day}^{-1}$.

These results are shown graphically in Fig. 4.6a–d which show the capture probabilities into various resonances on an $\omega_1 - \omega_2$ diagram. For concreteness, we show probabilities for $Q_1'/Q_J' = 4 \times 10^{-4}$. The figure depicts the capture probabilities into (a) the Laplace resonance, (b) the $\omega_1/\omega_2 \approx 3/2$ resonance, (c) the $\omega_1/\omega_2 \approx 2$ resonance, and (d) other resonances. The shading at a given (ω_1, ω_2) point gives the capture probability for the resonance in question, for evolution beginning at that point on the diagram. (The runs which enter $\omega_1 = \omega_2$ often pass through $\omega_1/\omega_2 \approx 1/2$, 2/3 or 3/4 first.) Dark hatching corresponds to unit probability, white to zero probability, and light hatching to intermediate ($\sim 50\%$) probability. The axes span approximately 0 to $-5°\text{day}^{-1}$. As can be seen, there are large portions of the diagram for which

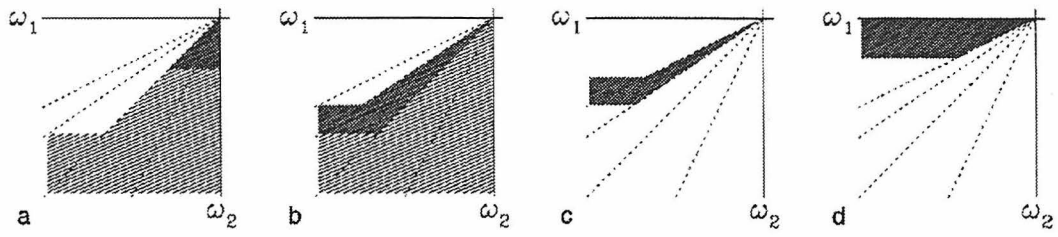

Figure 4.6: A schematic summary of capture probabilities as a function of initial ω_1 and ω_2 for the different resonances, shown on $\omega_1 - \omega_2$ plots. The probabilities shown hold for $Q_1'/Q_J' \approx 4 \times 10^{-4}$. Capture probabilities from given initial (ω_1, ω_2) are 1 if the point is black, 0 if the point is white, and are intermediate for grey. The four panels show probabilities for capture into (a) the Laplace resonance, (b) $\omega_1/\omega_2 \approx 3/2$, (c) $\omega_1/\omega_2 \approx 2$, and (d) 'other' states characterized by evolution to high ω_1/ω_2 values. The probabilities depend upon Q_1'/Q_J', as described in the text.

capture into $\omega_1/\omega_2 = 3/2$ or 2 is assured. More than half the area has moderate capture probability for $\omega_1/\omega_2 \approx 3/2$ and for the Laplace resonance. Runs starting in the dark region indicated in Fig. 4.6d evolved toward greater ω_1/ω_2, stabilizing at $\omega_1/\omega_2 \sim 8 - 40$, depending on initial conditions. We surmise that in these runs, where the system is initially very close to the Europa-Ganymede 2:1 resonance, equilibrium of the 2:1 pairwise resonances was achieved without the system ever becoming captured in a Laplace-like resonance.

The probabilities shown in Fig. 4.6 depend on Q_1'/Q_J'. For smaller values of Q_1'/Q_J', the pattern would be similar, but the axes would span a larger range of ω_1 and ω_2 and conversely for larger values of Q_1'/Q_J'. For example, for $Q_1'/Q_J' \sim 7 \times 10^{-5}$, the axes span 0 to $-10°\text{day}^{-1}$ in ω_1 and ω_2. If $Q_1'/Q_J' = 1 \times 10^{-3}$ the picture is very different: capture into the Laplace resonance would occur from everywhere in the $\omega_1 - \omega_2$ diagram except possibly for very small initial values of $|\omega_2|$; capture into $\omega_1/\omega_2 \approx 3/2$ or 2 is impossible. The corresponding Fig. 4.6a would then be almost fully black, and Figs. 4.6b and 4.6c would be fully white.

Capture probability also depends on e_3 before resonance encounter. It is shown in the appendix to Showman and Malhotra (1997) that capture into the $\omega_1/\omega_2 \approx$

2 resonance is likely if the initial $e_3 \leq 0.001$. Because the damping time for the eccentricity is on the order of 10^8 years for reasonable $(Q/k)_3$, Ganymede's eccentricity would likely have been negligible if resonance encounter occurred more than half a billion years after solar system formation.

In summary, for plausible values of Q_1'/Q_J', capture into $\omega_1/\omega_2 \approx 3/2$ or $\omega_1/\omega_2 \approx 2$ is moderately probable. For a substantial fraction of plausible initial conditions, the satellites pass through the $\omega_1/\omega_2 \approx 1/2$, 2/3, or 3/4 resonances.

4.3.4 Characteristics of $\omega_1/\omega_2 \approx 3/2$ and 2 resonances

As mentioned in the Introduction, the $\omega_1/\omega_2 \approx 3/2$ and $\omega_1/\omega_2 \approx 2$ Laplace-like resonances provide potentially much greater tidal heating in Ganymede than the $\omega_1/\omega_2 \approx 1/2$ resonance identified in Malhotra (1991). In Fig. 4.7, we display the maximum eccentricity and energy dissipation that Ganymede can achieve in the $\omega_1/\omega_2 \approx 3/2$ and 2 resonances, and compare them to the maximum possible for the $\omega_1/\omega_2 \approx 1/2$ resonance. As the dissipated power depends on Q_3'/Q_J', we plot the eccentricity and dissipation as a function of Q_3'/Q_J'. The eccentricity shown is the steady state eccentricity occurring after equilibration of the three body resonance. The dissipation is calculated from Q_3'/Q_J', Q_J', and the equilibrated eccentricity using the formula for tidal dissipation in a homogeneous, synchronously rotating satellite in an eccentric orbit (Peale and Cassen 1978):

$$\dot{E} = \frac{21}{2}\frac{k}{Q}\frac{R^5 G M_p^2 n e^2}{a^6}$$

where $\dot{E}$ is the dissipated power, R is the satellite's radius, a, e, and n are the orbital semi-major axis, eccentricity, and mean motion, M_p is the primary's mass (Jupiter), G is the gravitational constant, Q is the satellite's effective tidal dissipation function, and k is the satellite's second degree Love number; we use modern values $a = 1.07 \times 10^9\,\mathrm{m}$ and $n = 1.0 \times 10^{-5}\mathrm{s}^{-1}$. For the highest eccentricities shown, the equilibrium eccentricity is reached 1–2 $\times\ 10^4 Q_J$ years after resonance capture; however, for the lowest eccentricities, the equilibration time is only $\sim 10^3 Q_J$ years.

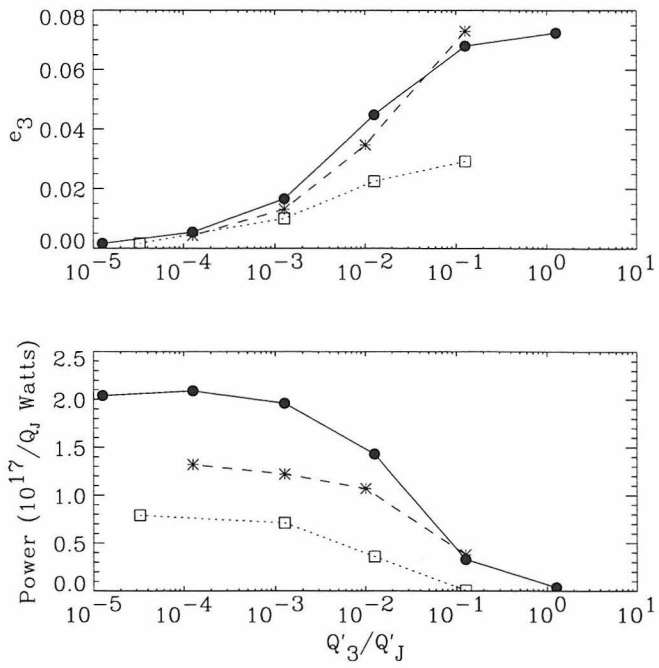

Figure 4.7: (a) Ganymede's maximum eccentricity, and (b) the dissipated power associated with those eccentricities, for the $\omega_1/\omega_2 \approx 2$, $\omega_1/\omega_2 \approx 3/2$, and $\omega_1/\omega_2 \approx 1/2$ resonances, as a function of Q'_3/Q'_J, the ratio of Q/k for Ganymede to that for Jupiter. Filled circles correspond to $\omega_1/\omega_2 \approx 2$, stars to $\omega_1/\omega_2 \approx 3/2$, and squares to the $\omega_1/\omega_2 \approx 1/2$ resonance. For the $\omega_1/\omega_2 \approx 3/2$ and 2 resonances, "maximum eccentricity" is the equilibrated (steady state) eccentricity; for the $\omega_1/\omega_2 \approx 1/2$ resonance, it is that at the peak of the largest possible eccentricity "bump." (Runs for $\omega_1/\omega_2 \approx 3/2$ and 2 used $Q'_1/Q'_J = 4 \times 10^{-4}$, and those for $\omega_1/\omega_2 \approx 1/2$ used 1.2×10^{-3}. All runs used $Q'_2/Q'_J = 4 \times 10^{-3}$.)

The maximum eccentricity and dissipation for $\omega_1/\omega_2 \approx 3/2$ or 2 is significantly greater than for $\omega_1/\omega_2 \approx 1/2$. Interestingly, as $Q'_3/Q'_J \to \infty$, the eccentricity saturates at a finite value, and as $Q'_3/Q'_J \to 0$, the eccentricity tends to zero.

The dissipation requires more careful consideration. For a given Q'_J, the dissipation saturates at a finite value as $Q'_3 \to 0$ but tends to zero for $Q'_3 \to \infty$. However, for a given Q'_3, dissipation$\to \infty$ as $Q'_J \to 0$, while dissipation tends to zero for $Q'_J \to \infty$. Dissipation is thus not solely a function of Q'_3/Q'_J; we plot it as such by incorporating Q_J into the vertical axis, using $k_J = 0.38$. For $Q_J \sim 3 \times 10^5$, the maximum dissipa-

tion for these resonances is few $\times 10^{11}$ W, about an order of magnitude lower than the primordial radiogenic heating rate (using carbonaceous chondritic radionuclide abundances for Ganymede's rock). If the resonances are disrupted before equilibration occurs, the actual peak eccentricity and dissipation would be lower, as occurs, for example, in Fig. 4.4 during the $\omega_1/\omega_2 \approx 3/2$ resonance.

We find that the dissipation and eccentricity for $\omega_1/\omega_2 \approx 3/2$ are roughly independent of ω_1 or ω_2 at capture. For a given Q_3'/Q_J', runs achieving values of $|\omega_1|$ from $2 - 8°\text{day}^{-1}$ at capture and from $1.5 - 4.3°\text{day}^{-1}$ at equilibrium of the three-body resonance yielded steady-state eccentricities differing by only 4%. Similar results hold for $\omega_1/\omega_2 \approx 2$. In contrast, Malhotra (1991) found that for $\omega_1/\omega_2 \approx 1/2$ the maximum eccentricity depends strongly on ω_1 at capture. This occurs because entry into the resonance at lower values of ω_1 and ω_2 allows a longer resonance lifetime, which leads to higher eccentricities. However, the $\omega_1/\omega_2 \approx 3/2$ and 2 resonances are never disrupted by themselves, so the lifetimes are not short enough to prevent equilibration of the eccentricity. The power and eccentricity for $\omega_1/\omega_2 \approx 1/2$ shown in Fig. 4.7 is the maximum found by Malhotra; capture at other ω_1 can produce a power for $\omega_1/\omega_2 \approx 1/2$ up to ~ 10 times lower.

Two runs (with $Q_3'/Q_J' \approx 10^{-1} - 10^{-2}$) entering $\omega_1/\omega_2 \approx 3/2$ yielded anomalously low eccentricities of ~ 0.008. These values fall far below the curve in Fig. 4.7. We do not understand this phenomenon, but the probability appears small, since it occurred in only 3% of our runs for $\omega_1/\omega_2 \approx 3/2$ and never occurred for $\omega_1/\omega_2 \approx 2$.

4.3.5 Disruption of $\omega_1/\omega_2 \approx 3/2$ and 2 resonances

For constant Q_i'/Q_J' values, none of the runs which entered $\omega_1/\omega_2 \approx 3/2$ or 2 was ever disrupted from the resonance. Thus, if the Q/k are constant in time, the $\omega_1/\omega_2 \approx 3/2$ and 2 resonances cannot be possible paths to the current state. However, we find that by changing Q_1'/Q_J or Q_2'/Q_J' during the run, the resonances can be disrupted and the satellites subsequently evolve into the Laplace resonance.

We did a number of runs to characterize the conditions leading to disruption.

Table 4.1: Disruption from $\omega_1/\omega_2 \approx 3/2$ into Other Resonances

	Time of disruption (Q_J years)			
$(Q_1'/Q_J')_0$	3×10^3	7×10^3	10^4	1.3×10^4
5×10^{-4}	No	No	No	No
8×10^{-4}	No	No	No	No
1.3×10^{-3}	$\omega_1 = \omega_2$	$\omega_1 = \omega_2$	$\omega_1 = \omega_2$	$\omega_1/\omega_2 \approx 2$

Note. Entries display the resonance entered after disruption. Runs labeled "no" were not disrupted from $\omega_1/\omega_2 \approx 3/2$.

First consider the $\omega_1/\omega_2 \approx 3/2$ resonance. This set of runs was started with $\omega_1 = -5.6°\text{day}^{-1}$ and $\omega_2 = -3.2°\text{day}^{-1}$, with initial $\omega_1/\omega_2 = 1.8$. The system thus encountered the $\omega_1/\omega_2 \approx 3/2$ resonance from above, passed through it without capture, minimized at $\omega_1/\omega_2 \simeq 1.2$, and as ω_1/ω_2 increased to 1.5, it entered the $\omega_1/\omega_2 \approx 3/2$ resonance from below at $\omega_1 = -2.5°\text{day}^{-1}$. We used $Q_3'/Q_J' = 0.0127$. The system entered resonance at $t = 2300\,Q_J$ years, and we continued the integration until $1.7 \times 10^4 Q_J$ years (5 billion years for $Q_J = 3 \times 10^5$). During this initial phase of the run, we kept Q_1'/Q_J' constant at 4×10^{-4}. Then, at a time t_0, we changed Q_1'/Q_J' to another value, $(Q_1'/Q_J')_0$. We used several different values of t_0 [$3300\,Q_J$, $6600\,Q_J$, $10^4 Q_J$, and $1.33 \times 10^4 Q_J$ years], and of $(Q_1'/Q_J')_0$ [5.0×10^{-4}, 7.6×10^{-4}, and 1.3×10^{-3}].

The results of these 12 runs are summarized in Table 4.1. None of the runs for the smaller two values of $(Q_1'/Q_J')_0$ were disrupted, and all four runs for the larger value were disrupted. The conditions for disruption thus seem relatively insensitive to the time during resonance at which disruption occurs. Of the four runs which were disrupted, three were captured into the Laplace resonance and one into $\omega_1/\omega_2 \approx 2$. Disruption usually occurred $\sim 10^3 Q_J$ years after t_0 rather than immediately; such delays are evident in Figs. 4.2–4.4 for our example runs. (When the system is disrupted from resonance, the new path taken is not predictable on a case by case basis. Thus, we cannot infer from Table 4.1 that capture probabilities into $\omega_1 = \omega_2$ vs. $\omega_1/\omega_2 \approx 2$ vary with time of disruption from $\omega_1/\omega_2 \approx 3/2$. Rather, our runs

suggest only that upon disruption of $\omega_1/\omega_2 \approx 3/2$, entry into the Laplace resonance is more likely than into $\omega_1/\omega_2 \approx 2$ in an *average* sense.)

We also tried runs for two smaller values of Q_3'/Q_J', 1.27×10^{-3} and 1.27×10^{-4}, with $(Q_1'/Q_J')_0 = 1.3 \times 10^{-3}$ and $Q_2'/Q_J' = 4.1 \times 10^{-3}$. The time between t_0 and disruption increased substantially over the case with $Q_3'/Q_J' = 0.0127$. Runs using the larger of these two values of Q_3'/Q_J' were disrupted, but runs with the smaller value did not disrupt before the end of the simulation. The resonance appears to be slightly more stable at low Q_3'/Q_J', presumably because of the lower eccentricities. Using a greater value $(Q_1'/Q_J')_0 = 1.9 \times 10^{-3}$ allows disruption of the resonance almost immediately at these low Q_3'/Q_J' values, however. Thus, the dependence on Q_3'/Q_J' seems much weaker than that on $(Q_1'/Q_J)_0$.

We also made four runs for $\omega_1/\omega_2 \approx 3/2$ in which we kept Q_1'/Q_J' constant over the run, but in which we increased or decreased Q_2'/Q_J' by one or two orders of magnitude at time t_0. Our initial value was $Q_2'/Q_J' = 4.1 \times 10^{-3}$ (same as that in the runs discussed above). We found that abruptly increasing Q_2'/Q_J' by one or two orders of magnitude during the run produced no visible effect on the resonances. Decreasing by one order of magnitude destabilized but did not disrupt the resonance, and decreasing by two orders of magnitude disrupted the Laplace-like resonance; the system then entered the Laplace resonance.

Next consider $\omega_1/\omega_2 \approx 2$. We find that this resonance is somewhat more stable than $\omega_1/\omega_2 \approx 3/2$, requiring an increase in Q_1'/Q_J' to $(Q_1'/Q_J')_0 = 1.9 \times 10^{-3}$ for disruption (using the same Q_3'/Q_J' and Q_2'/Q_J' as the 12 runs in Table 4.1). Changing Q_2'/Q_J' (but not Q_1'/Q_J') during the runs had the same effect as for the $\omega_1/\omega_2 \approx 3/2$ resonance: increasing Q_2'/Q_J' by one or two orders of magnitude had no effect, decreasing it by one order of magnitude destabilized but did not disrupt the resonance, and decreasing it by two orders of magnitude disrupted the resonance, with subsequent capture into the Laplace resonance.

Both resonances are stable to large *decreases* in Q_1'/Q_J' from 4×10^{-4} to 3×10^{-5}. The change simply shifted the three-body equilibrium from $-1.5°\text{day}^{-1}$ to $-8°\text{day}^{-1}$.

Finally, we mention two runs within the Laplace resonance, during which we

changed Q_1'/Q_J' to the large value $\sim 10^{-2}$. In these runs, Io's eccentricity reached a maximum value of 0.012 after the change, soon followed by disruption of the Laplace resonance. The system then settled at $\omega_1/\omega_2 \approx 9/10$. This result is consistent with the Yoder-Peale theory, which predicts the Laplace resonance to be unstable for $e_1 > 0.012$.

The above results can be understood as follows, in light of the analysis given in the appendix to Showman and Malhotra (1997). (That appendix gives a perturbative analysis of the $\psi_3 \equiv 2\theta_2 - \theta_1 - \varpi_3$ Laplace-like resonance, where $\theta_1 = 2\lambda_2 - \lambda_1$ and $\theta_2 = 2\lambda_3 - \lambda_2$; $lambda_1$, $lambda_2$, and $lambda_3$ are the mean longitudes of Io, Europa, and Ganymede, respectively, and ϖ_3 is Ganymede's longitude of perijove. This is one of the $\omega_1/\omega_2 \approx 2$ resonances and is relevant for pumping Ganymede's eccentricity.) Within any resonance, the equilibrium value of ω_1 (and hence, also the equilibrium value of Io's forced eccentricity, $\bar{e}_{12}$) is determined by the value of $D_1 \simeq 4.85(Q_J'/Q_1')$; $\bar{e}_{12}$ is proportional to Q_1'/Q_J' [see Eqs. (A49) and (A60) in the Appendix to Showman and Malhotra (1997)]. For $Q_1'/Q_J' = 4 \times 10^{-4}$, we find from Eq. (A60) of that paper that $\bar{e}_{12} \simeq 0.0020$ in the $\omega_1/\omega_2 \approx 2$ Laplace-like resonance; this is verified in the numerical simulations. (We have also estimated the equilibrium value for the $\omega_1/\omega_2 \approx 3/2$ Laplace-like resonance: $\bar{e}_{12} \simeq 0.0023$.) Note that the 3–body resonant interactions also force large amplitude oscillations about the mean forced eccentricity, so that the maximum eccentricity is significantly larger. When we change the value of Q_1'/Q_J' during the evolution, the equilibrium is shifted, and the system tries to evolve to the new equilibrium while maintaining the 3–body resonance lock. A decrease in Q_1'/Q_J' shifts $\bar{e}_{12}$ and $\bar{\omega}_1$ to smaller values, and the system accordingly moves to the lower equilibrium point, with no loss of stability. An increase in Q_1'/Q_J', on the other hand, raises these equilibrium values, and the system tries to move toward this higher equilibrium. In this case, there are several sources of instability.

1. The resonances are unstable when e_1 exceeds some maximum value. For the Laplace resonance, Yoder and Peale (1981) estimated the upper limit to be 0.012, from a linear stability analysis. For the other Laplace-like resonances, we expect a smaller upper limit for stability.

2. A second, qualitatively distinct source of instability is the overlap of all Laplace-like resonances sufficiently close to the origin in the ω_1, ω_2 plane. The numerical explorations by Malhotra (1991) as well as those in the present work indicate that sufficiently close to the origin in the ω_1, ω_2 plane, the phase space is dominated by the Laplace resonance. The Galilean satellites evolving along one of the Laplace-like resonances, $\omega_1/\omega_2 \approx j/(j+1)$ or $(j+1)/j$, eventually exit that resonance when both $|\omega_1|$ and $|\omega_2|$ become sufficiently small; after a period of chaotic evolution, they eventually enter the Laplace resonance.

3. Thirdly, the perturbation analysis in the appendix to Showman and Malhotra (1997) suggests that the evolution of ψ_3 is governed by a pendulum-like equation with an applied torque (caused by tidal dissipation in Jupiter and Io). The amplitude of the restoring term and magnitude of the tidal term fluctuate over the ψ_3 libration cycle (largely as a result of fluctuations in Io's eccentricity). When Q_1/Q_J is increased past a critical value, these fluctuations lead to a gradual increase in the libration amplitude of ψ_3. This causes disruption of the resonance.

All of the above three sources of instability come into play when we increase Q_1'/Q_J' during the course of the evolution. Which of them is the primary cause of resonance disruption depends upon the exact parameters and state of the system. But it is clear that even in the absence of the first two, a sufficiently large increase in Q_1'/Q_J' during the course of the evolution would certainly disrupt the resonance. Runs performed using sinusoidally varying Q_1'/Q_J' (with periods of order $10^3 Q_J$ years and peak-to-peak amplitudes similar to those shown in Figs. 4.2-4.4) show that resonance disruption still occurs easily; for such runs, the first two mechanisms listed above will be most relevant.

The tidal terms in the pendulum-like equation contain the factor Q_J^{-1}, implying that greater dissipation in Jupiter leads to greater tidal torque on the pendulum-like evolution of ψ_3. Evaluation of the strength of the tidal and restoring terms using $Q_J = 100$ (the value we use in our simulations) shows that the tidal term is about two orders of magnitude weaker than the restoring term for the ψ_3 resonance; for the Laplace resonance, the tidal term is about four orders of magnitude weaker. Therefore, we

conclude that the adiabaticity of the evolution of the real system near these resonances is preserved in our numerical simulations. (This also confirms that disruption of the $\omega_1/\omega_2 \approx 2$ resonance in our simulations does not result from domination of the restoring torque by the tidal torque. This is good because that is not a realistic disruption mechanism for the real system.) Further confidence that the evolution is adiabatic at $Q_J = 100$ was provided by Malhotra (1991), who carried out some runs using higher values of Q_J up to 1000 to confirm her results.

In the numerical experiments where we start with $Q_1'/Q_J' = 4 \times 10^{-4}$, and later increase its value by a factor of about 3, we note that the $\omega_1/\omega_2 \approx 3/2$ or 2 Laplace-like resonance is not immediately disrupted (cf. Figs. 4.2—4.4). Io's eccentricity increases towards the new equilibrium value, while the ratio ω_1/ω_2 is, on average, maintained at the resonant value. During this period, Ganymede's forced eccentricity is also maintained at a high value, although it does not continue its previous increase; this is further evidence of the fact that the Laplace-like resonance remains in place with the new value of Q_1'/Q_J', but there is no longer the same rate of secular transfer of orbital energy and angular momentum to Ganymede from Io and Europa. Eventually the $\omega_1/\omega_2 \approx 3/2$ or 2 resonance does become unstable, when Io's mean forced eccentricity approaches ~ 0.005 (maximum e_1 exceeds ~ 0.01). This is followed by a short period, $\sim 10^3 Q_J$ years, of chaotic, large-amplitude fluctuations in all dynamical variables, culminating in the satellites entering the Laplace resonance. The Laplace resonance cannot maintain Ganymede's high forced eccentricity, so e_3 plummets rapidly. It appears likely in this case that the parameters of the system conspire in such a way that all three causes of instability identified above occur nearly simultaneously.

In the above numerical experiments, we have chosen to use a very simple step-function model for the time variation of Q_1'/Q_J'. This is admittedly not a physically realistic model. However, physically realistic models for the Q and k_2 of Io as well as the Q of Jupiter remain highly unconstrained at the present time. Given this, building a specific physical model for the evolution of these parameters and folding it in with the orbital dynamics model is poorly justified. The numerical experiments here do serve our limited purpose of investigating the response of the 3-body Laplace-like

resonances to changes in Q_1'/Q_J'.

4.3.6 Other results

We report in this section the results of a few runs in which the system entered other resonances. One entered $\omega_1/\omega_2 \approx 13/6$, and another entered what was perhaps $\omega_1/\omega_2 \sim 7/3$ or $11/5$. Two runs spent a few percent of the integration time in $\omega_1/\omega_2 \approx 4/3$ before disruption into another resonance ($\omega_1/\omega_2 \approx 2$ in one case and $\omega_1/\omega_2 \sim 7/3$ in another). None of these resonances pumps Ganymede's eccentricity, and the combined probabilities for these paths appear low.

These resonances are dynamically similar to the $\omega_1/\omega_2 \approx 3/2$ and 2 resonances: capture occurred only from below, and, with the exception of $\omega_1/\omega_2 \approx 4/3$, disruption never occurred; the system equilibrated at values of ω_1 greater than that for the Io-Europa pairwise resonance alone. In contrast, resonances below $\omega_1/\omega_2 = 1$ are always disrupted, usually into the Laplace resonance or $\omega_1/\omega_2 \approx 3/2$ (depending on Q_1'/Q_J'); these resonances never achieved equilibrium. The resonances above the Laplace resonance thus seem to exhibit very different dynamics than those below the Laplace resonance.

4.4 Ganymede's free eccentricity

In this section, we consider the problem of Ganymede's large free eccentricity, $e_{\text{free}} = 0.0015$. This has long been a puzzle because the tidal damping time for Ganymede's eccentricity is $10^6 Q_3$, or about 10^8 years for a plausible $Q_3 \approx 10^2$; its free eccentricity should therefore have long damped by the present time. Although free eccentricity is often portrayed as a "remnant" primordial eccentricity, orbital resonances can pump the free as well as the forced eccentricity. (The free eccentricity is manifested in Figs. 4.2–4.4 as a rapid oscillation about the mean value.) Since the Laplace resonance does not pump Ganymede's free eccentricity, e_{free} may thus provide a useful constraint on past orbital evolution. We find that the free eccentricity Ganymede attains in the $\omega_1/\omega_2 \approx 3/2$ or 2 resonances is greater for smaller Q_1'/Q_J', possibly because smaller

Q_1'/Q_J' leads to equilibration of the three body resonances closer to the (ω_1, ω_2) origin. For constant $Q_1'/Q_J' \approx 4 \times 10^{-4}$, the $\omega_1/\omega_2 \approx 3/2$ and 2 resonances pump Ganymede's free eccentricity to $\sim 6 - 9 \times 10^{-4}$, independent of Q_3'/Q_J'. Although this is almost an order of magnitude higher than that typically achieved during $\omega_1/\omega_2 \approx 1/2$, it is still a factor of ~ 2 lower than that observed.

We consider here the size of an asteroidal or cometary impactor required to excite Ganymede's eccentricity to 0.0015, and compare this estimate with the impactor masses obtained from Ganymede's largest craters.

Let the comet strike Ganymede at an angle θ tangent to Ganymede's orbit, where θ is measured in an inertial reference frame centered on Jupiter. Let $\theta \sim 0$ imply an overtaking collision and $\theta \sim \pi$ imply a head-on collision. We assume the comet strikes through Ganymede's center of mass, so no change in rotation occurs. We further assume an inelastic collision in which Ganymede retains the cometary mass. If the eccentricity is initially zero, then the eccentricity after impact is (to second order in m/M, which is taken to be a small quantity)

$$e^2 = \left(\frac{m}{M}\right)^2 \left[4 + \frac{v_c^2}{v_i^2}(1 + 3\cos^2\theta) - 8\frac{v_c}{v_i}\cos\theta\right]$$

where m and v_c are the cometary mass and speed; M and v_i Ganymede's mass and speed. Both speeds are measured relative to Jupiter. For $v_c = v_i$ and $\theta = 0$, the comet should "soft land" on Ganymede without perturbing the eccentricity. As required, the equation gives $e = 0$ for this situation.

A comet capable of pumping Ganymede's eccentricity to 0.0015 must thus be of mass $\sim 10^{20}$ kg. Is this plausible? The largest fresh crater on Ganymede is Gilgamesh, which has a probable excavation diameter of 550 km (Shoemaker et al. 1982). We calculate the transient crater diameter using the relation from McKinnon and Schenk (1995), and then estimate the impactor mass from the scaling law in Chapman and McKinnon (1986, p. 502):

$$m = \frac{4\pi}{3}\rho\left[\frac{3V}{4\pi A}\right]^{3/(3-\alpha)}\left(\frac{3.22g}{u^2}\right)^{3\alpha/(3-\alpha)}$$

where V is the transient crater volume, ρ is the impactor density (assumed equal to the target density), u is impact speed, g is surface gravity, and A and α are dimensionless parameters. Using nominal values $u = 15\,\mathrm{km\,s^{-1}}$, $g = 1.5\,\mathrm{m\,sec^{-2}}$, plus $A = 0.19$ and $\alpha = 0.65$ appropriate to a solid ice target, we find that a $10^{17}\,\mathrm{kg}$ bolide created Gilgamesh. Choosing smaller values for A and α allows a larger impactor for a given crater size. Using $A = 0.1$ and $\alpha = 0.5$, which are plausible lower bounds, implies an impactor of mass $\sim 10^{18}\,\mathrm{kg}$, still far too small. Other large impact features on Ganymede, such as palimpsests, are so old that any eccentricity they produce would be damped by the present time. Thus, we conclude that Ganymede's eccentricity cannot have been produced by an impact.

Although the $\omega_1/\omega_2 \approx 3/2$ and 2 resonances excite Ganymede's free eccentricity to only half the current value in our runs, paths may exist which allow larger free eccentricities. Exploratory runs suggest that these resonances are slightly more stable to gradual billion-year changes in Q_1'/Q_J' than to abrupt changes (although disruption can still occur). Slow change to $Q_1'/Q_J' = 10^{-3}$ leads to $e_{\mathrm{free}} = 1.0 \times 10^{-3}$ in cases when disruption does not occur, and larger e_{free} may be possible if Q_1'/Q_J' rises even higher before disruption.

4.5 Summary

We have used the model of Malhotra (1991) to explore the orbital dynamics and tidal evolution of Io, Europa, and Ganymede near the Laplace resonance. Our principal results are those relevant to Ganymede's thermal history. We have shown that if the satellites passed through a Laplace-like resonance characterized by either $\omega_1/\omega_2 \approx 3/2$ or $\omega_1/\omega_2 \approx 2$, Ganymede's eccentricity could have risen as high as ~ 0.07. These resonances produce a tidal dissipation rate several hundred times higher than at the present epoch (for reasonable Q_J), and $\sim 2 - 30$ times higher than the maximum possible for the $\omega_1/\omega_2 \approx 1/2$ Laplace-like resonance identified by Malhotra (1991). Capture probabilities for these two resonances are ~ 0.9 if they are encountered from below (i.e., with ω_1/ω_2 increasing with time); the capture probability is negligible

otherwise. We have found that resonance capture can occur with initial conditions in a substantial fraction of the $\omega_1 - \omega_2$ plane (i.e., for a large range of initial a_1/a_2 and a_2/a_3 values) provided $Q_1'/Q_J' \leq 6 \times 10^{-4}$. This upper limit is slightly smaller than that needed to maintain Io's current eccentricity in steady state, $Q_1'/Q_J' \approx 1.1 \times 10^{-3}$ (cf. Yoder and Peale 1981). For the latter value, the properties of the evolution of ω_1 and ω_2 conspire with capture statistics for the Laplace resonance to prevent the system from ever encountering these new resonances from below. This explains why they were not seen by Malhotra (1991) who restricted her study to $Q_1'/Q_J' \approx 1.1 \times 10^{-3}$. We note that the smaller values of Q_1'/Q_J' (which allow capture in the $\omega_1/\omega_2 \approx 3/2$ and $\omega_1/\omega_2 \approx 2$ resonances) are reasonable, and could in fact be close to the modern value because that required for equilibrium at present may be too large to maintain Io's current heat flow (Veeder et al. 1994).

These new resonances differ from $\omega_1/\omega_2 \approx 1/2$ in one important respect: they achieve stable equilibria, and therefore are never disrupted if the Q/k are constant in time. However, we find that increasing Q_1'/Q_J' by a factor of ~ 3 or decreasing Q_2'/Q_J' by a factor of ~ 100 disrupts the resonances, allowing capture into the Laplace resonance with high probability. Several of the results of our numerical simulations were verified by a perturbation analysis of the low order resonant interactions (appendix, Showman and Malhotra 1997).

Just as in the previous study of Malhotra (1991), the net orbital expansion of the Galilean satellites required in these evolutionary paths is easily accommodated with a tidal dissipation function for Jupiter, Q_J, of a few $\times 10^5$.

In two companion papers we discuss the implications of resonance passage for Ganymede's thermal history. In Showman et al. (1997), which is presented in Chapter 5, we couple the orbital model to an internal model for Ganymede. Under certain circumstances, non-linear "thermal runaways" can occur within Ganymede, causing internal warming and melting of the ice mantle. In Showman and Stevenson (1996), we propose models of local, near-surface thermal runaways, and evaluate the efficacy of several resurfacing mechanisms. Because the greater dissipation increases the likelihood of resurfacing, we favor $\omega_1/\omega_2 \approx 3/2$ or 2 over $\omega_1/\omega_2 \approx 1/2$ for the orbital

history of the Galilean satellites before evolution into the Laplace resonance.

Since the current resonances do not explain Ganymede's free eccentricity, $e_{\rm free}$ is a remnant of Ganymede's prior history. We have shown that the mass of a cometary or asteroidal impactor required to pump $e_{\rm free}$ to its current value is $\sim 10^2 - 10^3$ times larger than that which produced Gilgamesh, the only candidate crater for such an impact. We surmise that the current free eccentricity is thus remnant from an ancient resonance passage. The $\omega_1/\omega_2 \approx 3/2$ and 2 resonances can pump $e_{\rm free}$ up to two-thirds its modern value. Our models employ constant or step-function Q_i'/Q_J', however. More realistic time variation in these parameters may yield larger $e_{\rm free}$.

Other observed orbital parameters of the Galilean satellites also hold memory of their prior evolution and may provide further constraints. The libration amplitudes for the θ_{11}, θ_{12}, θ_{23}, and Laplace resonances (Sinclair 1975) contain information about the age of the resonances, the $\omega_1 - \omega_2$ path followed in the past, the Q_i'/Q_J' and their time histories, and other factors. A successful model of the orbital and thermal history of these satellites should, in principle, yield simultaneously the current values of all four libration amplitudes; this constraint could allow some orbital histories to be excluded. In practice, however, the factors affecting the amplitudes might be difficult to separate, preventing useful constraints on any individual parameter from being developed. Further, it is also worth keeping in mind that for a dissipative system, there are multiple, non-unique, paths to an equilibrium (or quasi-equilibrium) state; the final state of the system would retain only partial memory of initial conditions and intermediate states.

4.6 References

BANFIELD, D. AND N. MURRAY 1992. A dynamical history of the inner Neptunian satellites. *Icarus* **99**, 390-401.

BERCKHEMER, H., W. KAMPFMANN, E. AULBACH, AND H. SCHMELING 1982. Shear modulus and Q of forsterite and dunite near partial melting from forced-

oscillation experiments. *Phys. Earth Planet. Inter.* **29**, 30-41.

CHAPMAN, C.R. AND W.B. MCKINNON 1986. Cratering of planetary satellites. In *Satellites* (J.A. Burns and M.S. Matthews, Eds.), pp. 492-580. Univ. of Arizona Press, Tucson.

GAVRILOV, S.V. AND V.N. ZHARKOV 1977. Love numbers of the giant planets. *Icarus* **32**, 443-449.

GOLDREICH, P. AND S. SOTER 1966. Q in the solar system. *Icarus* **5**, 375-389.

GREENBERG, R. 1982. Orbital evolution of the Galilean satellites. In *Satellites of Jupiter* (D. Morrison, Ed.), pp. 65-92. Univ. of Arizona Press, Tucson.

GREENBERG, R. 1987. Galilean satellites: evolutionary paths in deep resonance. *Icarus* **70**, 334-347.

HENRARD, J. 1983. Orbital evolution of the Galilean satellites: capture into resonance. *Icarus* **53**, 55-77.

IOANNOU, P.J. AND R.S. LINDZEN 1993. Gravitational tides in the outer planets. II. Interior calculations and estimation of the tidal dissipation factor. *Astrophys. J.* **406**, 266-278.

MALHOTRA, R. 1991. Tidal origin of the Laplace resonance and the resurfacing of Ganymede. *Icarus* **94**, 399-412.

MALIN, M.C. AND D.C. PIERI 1986. Europa. In *Satellites* (J.A. Burns and M.S. Matthews, Eds.), pp. 689-717. Univ. of Arizona Press, Tucson.

MCKINNON, W.B. AND E.M. PARMENTIER 1986. Ganymede and Callisto. In *Satellites* (J.A. Burns and M.S. Matthews, Eds.), pp. 718-763. Univ. of Arizona Press, Tucson.

MCKINNON, W.B. AND P.M. SCHENK 1995. Estimates of comet fragment masses from impact crater chains on Callisto and Ganymede. *Geophys. Res. Lett.* **22**, 1829-1832.

OJAKANGAS, G.W. AND D.J. STEVENSON 1986. Episodic volcanism of tidally heated satellites with application to Io. *Icarus* **66**, 341-358.

PEALE, S.J. AND P.M. CASSEN 1978. Contribution of tidal dissipation to lunar thermal history. *Icarus* **36**, 245-269.

PEALE, S.J., P. CASSEN, AND R.T. REYNOLDS 1979. Melting of Io by tidal dissipation. *Science* **203**, 892-894.

SHOEMAKER, E.M., B.K. LUCCHITTA, D.E. WILHELMS, J.B. PLESCIA, AND S.W. SQUYRES 1982. The geology of Ganymede. In *Satellites of Jupiter* (D. Morrison, Ed.), pp. 435-520.

SHOWMAN, A.P. AND D.J. STEVENSON 1996. Resurfacing of Ganymede and other icy satellites by passage through orbital resonance. Submitted to *Icarus.*

SHOWMAN, A.P., D.J. STEVENSON, AND R. MALHOTRA 1997. Coupled orbital and thermal evolution of Ganymede. *Icarus* **129,** 367-383.

SINCLAIR, A.T. 1975. The orbital resonance amongst the Galilean satellites of Jupiter. *Mon. Not. R. Astr. Soc.* **171**, 59-72.

SMITH, B.A., L.A. SODERBLOM, T.V. JOHNSON, A.P. INGERSOLL, S.A. COLLINS, E.M. SHOEMAKER, G.E. HUNT, H. MASURSKY, M.H. CARR, M.E. DAVIES, A.F. COOK II, J. BOYCE, G.E. DANIELSON, T. OWEN, C. SAGAN, R.F. BEEBE, J. VEVERKA, R.G. STROM, J.F. MCCAULEY, D. MORRISON, G.A. BRIGGS, AND V.E. SUOMI 1979. The Jupiter system through the eyes of Voyager 1. *Science* **204**, 951-972.

STEVENSON, D.J. 1983. Anomalous bulk viscosity of two-phase fluids and implications for planetary interiors. *J. Geophys. Res.* **88**, 2445-2455.

TITTEMORE, W.C. AND J. WISDOM 1989. Tidal evolution of the Uranian satellites: II. an explanation of the anomalously high orbital inclination of Miranda. *Icarus* **78**, 63-89.

TITTEMORE, W.C. 1990. Chaotic motion of Europa and Ganymede and the Ganymede-Callisto dichotomy. *Science* **250**, 263-267.

VEEDER, J.G., D.L. MATSON, T.V. JOHNSON, D.L. BLANEY, AND J.D. GOGUEN 1994. Io's heat flow from infrared radiometry: 1983-1993. *J. Geophys. Res.* **99**, 17,095-17,162.

YODER, C.F. 1979. How tidal heating in Io drives the Galilean orbital resonance locks. *Nature* **279**, 767-770.

YODER, C.F. AND S.J. PEALE 1981. The tides of Io. *Icarus* **47**, 1-35.

Chapter 5

Coupled orbital and thermal evolution of Ganymede

Adam P. Showman

Division of Geological and Planetary Sciences 150-21

California Institute of Technology

Pasadena, CA 91125

and

Lunar and Planetary Institute

3600 Bay Area Boulevard

Houston, TX 77058

David J. Stevenson

Division of Geological and Planetary Sciences 150-21

California Institute of Technology

Pasadena, CA 91125

and

Renu Malhotra

Lunar and Planetary Institute

3600 Bay Area Boulevard

Houston, TX 77058

5.1 Abstract

We explore the hypothesis that passage through an eccentricity-pumping resonance could lead to the resurfacing of Ganymede. To do so, we couple Malhotra's (1991) orbital model for the tidal evolution of the Laplace resonance to an internal model of Ganymede. Our model explores the conditions under which Ganymede can undergo global thermal runaway, assuming that the Q/k of Ganymede is strongly dependent on internal temperature. (Here Q is the tidal dissipation function and k is the second degree Love number.) We allow the system to pass through the $\omega_1/\omega_2 \approx 2$ or $\omega_1/\omega_2 \approx 1/2$ resonance, where $\omega_1 \equiv 2n_2 - n_1$, $\omega_2 \equiv 2n_3 - n_2$, and n_1, n_2, and n_3 are the mean motions of Io, Europa, and Ganymede. If Ganymede's initial internal temperature is either "too hot" or "too cold," no runaway occurs, while for intermediate temperatures (~ 200 K in the upper mantle), conditions are "just right," and runaway occurs. The range of mantle temperatures which allows runaway depends on the model for tidal Q; we use the Maxwell model which ties Q to the creep viscosity of ice. Runaways can induce up to $\sim 50 - 100$ K warming and formation of a large internal ocean; they occur over a $10^7 - 10^8$ year period. Assuming carbonaceous chondritic abundances of radionuclides in Ganymede's rocky portion, however, we find that the interior cannot cool to the initial temperatures needed to allow large runaways. If our model is correct, large runaways cannot occur, although small runaways are still possible. Different formulations of tidal Q or convective cooling may allow large runaways. Large runaways are also possible if radionuclides are substantially depleted, although this is unlikely.

We next consider the consequences of a large runaway, assuming it can occur. Ganymede can undergo $\sim 0.5\%$ thermal expansion (by volume) during the largest thermal runaways. Melting of the ice mantle provides up to $\sim 2\%$ expansion despite the fact that contraction produced by melting ice I offsets expansion produced by melting high pressure ice phases. Solid-solid phase transitions cause negligible satellite expansion. Lithospheric stresses caused by expansion of 2% over $10^7 - 10^8$ years are $\sim 10^2$ bars at the surface, and drop to a few bars at several km depth. Such

stresses could cause cracking to depths of several km. The cracking and near-surface production of warm or partially molten ice makes resurfacing a plausible outcome of a large thermal runaway. The tidal heating events proposed here may also be relevant for generation of Ganymede's modern-day magnetic field.

5.2 Introduction

Ganymede and Callisto have similar bulk properties but divergent surfaces. Callisto's surface is old and shows little sign of endogenic volcanic or tectonic activity. Half of Ganymede's surface resembles that of Callisto, but the other half was resurfaced long after late heavy bombardment. The differences between the satellites are puzzling, because one might expect that satellites with similar bulk properties would follow similar evolutionary pathways. Understanding why the two satellites evolved so differently is potentially important for understanding icy satellite formation and evolution generally.

There have been many previous attempts to explain why Ganymede but not Callisto might undergo upper mantle activity (e.g., melting), most of which assume the divergent evolutionary paths were caused by small quantitative differences in initial conditions, size, or composition of the two satellites (Squyres 1980, Cassen et al. 1980, Schubert et al. 1981, McKinnon 1981, Lunine and Stevenson 1982, Friedson and Stevenson 1983, Kirk and Stevenson 1987). Generally, such studies show that one must carefully tune poorly known parameters in order to get extensive activity in Ganymede but not Callisto. Such mechanisms are therefore unlikely. In addition, these models generally provide no plausible means for transporting material to the surface, even if mantle activity seems likely. A comprehensive review of the problem and early work is given by McKinnon and Parmentier (1986).

Although Ganymede's current eccentricity is low (0.0015), the eccentricity might have been high enough in the past for tidal dissipation to drive internal activity (Showman and Malhotra 1997 [which is presented as Chapter 4 of this thesis], Malhotra 1991, Tittemore 1990, Greenberg 1987). The most plausible scenario is that

of Malhotra (1991) and Showman and Malhotra (1997), in which Io, Europa, and Ganymede pass through a Laplace-like resonance before evolving into the presently observed Laplace resonance. These authors explored several scenarios by which the Laplace resonance, $\omega_1 = \omega_2$, was established; here $\omega_1 \equiv 2n_2 - n_1$, $\omega_2 \equiv 2n_3 - n_2$, and n_1, n_2, and n_3 are the mean motions (i.e., the mean orbital angular velocities) of Io, Europa, and Ganymede respectively. They showed that three scenarios, involving temporary capture into a resonance characterized by $\omega_1/\omega_2 \approx 1/2$, $3/2$, or 2, pump Ganymede's eccentricity to $\sim 0.01 - 0.04$.

Although the most optimum scenarios of Showman and Malhotra (1997) and Malhotra (1991) produce a mean heating great enough to significantly enhance upper mantle activity, this is untrue in general. Hence, it is unclear how the resonance causes resurfacing. The most violent mean heating rate possible during resonance passage is roughly 10^{13} W (Showman and Malhotra 1997), several times the primordial radiogenic heating rate of 3×10^{12} W occurring in Ganymede's rocky portion (assumed carbonaceous chondritic). This tidal heating rate requires Q_J to be near its time-averaged lower limit of 3×10^4 and that the system pass through the $\omega_1/\omega_2 \approx 2$ resonance, the most powerful of the three eccentricity-pumping Laplace-like resonances. (Here, Q_J is the tidal Q of Jupiter.) However, Q_J is unknown and could greatly exceed 3×10^4, implying a lower heating rate. Further, for a given Q_J, weaker heating would occur if the system passed through $\omega_1/\omega_2 \approx 3/2$ or $1/2$ rather than $\omega_1/\omega_2 \approx 2$. For example, passage through the $\omega_1/\omega_2 \approx 1/2$ resonance generates $\sim 2 \times 10^{11}$ W of dissipative heating if $Q_J = 3 \times 10^5$ (Showman and Malhotra 1997, Malhotra 1991). Relative to radiogenic heating, such tidal heating is weak and is unlikely to account for upper mantle activity or resurfacing.

If Q/k changes with time, however, the power dissipated during narrow time intervals can overwhelm radiogenic heating even when mean heating is below radiogenic. The tidal energy dissipation rate within a synchronously rotating satellite in an eccentric orbit is (Peale and Cassen 1978)

$$\dot{E} = \frac{21}{2}\frac{k}{Q}\frac{R^5 G M_p^2 n e^2}{a^6} \approx 2 \times 10^{18} \left(\frac{k}{Q} e^2\right) \text{ W}, \tag{5.1}$$

where R is the satellite's radius, a, e, and n are the orbital semi-major axis, eccentricity, and mean motion, M_p is the primary's mass (Jupiter), G is the gravitational constant, Q is the satellite's effective tidal dissipation function, and k is the satellite's second degree Love number, which parameterizes the height of the tidal bulge relative to the equipotential (Munk and MacDonald 1960); the numerical estimate given in Eq. (5.1) is for Ganymede. Suppose Q/k begins high (say 10^3), so that e reaches 0.02-0.04 within one of the Laplace-like resonances described by Showman and Malhotra (1997) or Malhotra (1991). If Q/k drops suddenly to ~ 10, the tidal dissipation would be a few $\times\ 10^{13}$ W, ten times greater than primordial radiogenic heating. Clearly such an event could make resurfacing far more likely.

Further, the energy released upon a large decrease in Q/k is great enough to allow internal activity. The change in Ganymede's orbital energy at constant orbital angular momentum is (for small e) $\Delta E \approx G M_J M e \Delta e / a$, where M_J and M are Jupiter's and Ganymede's mass, and Δe is the change in eccentricity. For circularizing the orbit, we take $e \sim \Delta e \sim 0.03$, which gives $\Delta E \approx 2 \times 10^{28}$ J. Complete melting of Ganymede's icy fraction (roughly one half Ganymede's mass) requires $0.5ML \approx 2 \times 10^{28}$ J, where $L \approx 3 \times 10^5$ J kg^{-1} is the latent heat of melting and M is Ganymede's mass. Thus, if Q/k plummets quickly enough for minimal convective loss of the dissipated energy, massive melting is possible.

We postulate that Ganymede's Q/k depends sensitively on Ganymede's internal temperature and structure, and that Q/k is lower for warm, molten states than for cold, frozen states. This provides a mechanism whereby Q/k can change very rapidly. Suppose Ganymede initially begins cold, with high Q/k. The eccentricity would therefore rise to a high value, thereby increasing dissipation. The warming caused by this dissipation would decrease Q/k slightly, which would increase the dissipation and accelerate the rate of warming and of decrease in Q/k. (This requires Q/k to decrease faster than e^2, so that $e^2 k/Q$ increases over time.) Thus, a positive

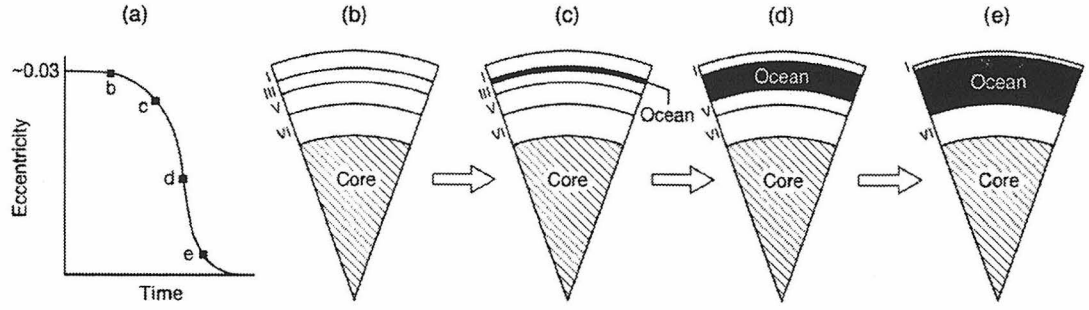

Figure 5.1: Qualitative effects of a thermal runaway on Ganymede's structure. (a) Schematic of Ganymede's eccentricity over time during the runaway. (b)-(e) Cross sections of Ganymede at various times during the runaway, as marked in (a). The initially frozen, differentiated Ganymede undergoes melting at the ice I-III interface, leading to formation of a massive internal ocean.

feedback could occur, in which Ganymede undergoes massive "runaway" heating and in which e plummets over an extremely short time interval.

In Fig. 5.1, we illustrate the qualitative effects of such a runaway on Ganymede's structure. Figure 5.1a schematically displays Ganymede's eccentricity over time during the runaway. Figures 5.1b-e show cross sections of Ganymede's interior at various times during the runaway, marked in Fig. 5.1a. Suppose the initial state is frozen and differentiated, containing a rock/iron core overlain by a water ice mantle of ice I, III, V, and VI. Because the ice mantle adiabatic temperature rises only gently with depth, and because the water ice melting temperature minimizes at the ice I-III interface (at $\sim 160\,\mathrm{km}$ depth), melting begins there, leading to formation of an ocean between these layers. As melting continues, the ocean grows, and both the ice I and III layers decrease in size. Eventually, ice I and V and then ice I and VI melt simultaneously. Alternatively, Ganymede might enter the runaway cold, containing only ices I, II, and VI. The runaway could convert the ice II into ices I, III, and V, leading to a final state similar to that shown in Fig. 5.1b (see phase diagram in Hobbs 1974). Either of these processes might lead to expansion and possibly lithospheric cracking.

In this paper, we explore the coupled orbital and thermal dynamics of Ganymede to answer several questions: (1) Can thermal runaways occur, and if so, what conditions are necessary for their occurrence? What range of mantle temperatures are needed at the onset of orbital resonance to trigger a runaway? Are such initial mantle temperatures plausible, given likely radiogenic heating and convective cooling rates? (2) How much warming or melting occurs during the runaways? Over what timescale do the runaways occur? (3) What are the implications of the runaways for lithospheric stresses and cracking?

To attack the first two questions, we construct a model of Ganymede's interior, from which we can calculate Q/k. We couple this model to Malhotra's (1991) orbital model, and follow the evolution of Ganymede's orbital and structural characteristics over time in a computer simulation. To answer the third question, we calculate the extent to which Ganymede would expand during a runaway from internal phase changes and thermal expansion. Using this value of strain and the runaway timescales, we can estimate the lithospheric strain rate encountered during the runaway, and solve for the lithospheric stress using the Maxwell equation.

The paper is organized as follows. Section 5.3 contains a description of the Ganymede thermal model. Section 5.4 describes the results of the coupled orbital-thermal model. In Section 5.5 we calculate the satellite expansion caused by runaway, and in Section 5.6 we calculate lithospheric stress as a function of depth and estimate the depth to which cracking can occur. In Section 5.7 we discuss the implications of our results for resurfacing. Although we have not modeled the detailed evolution of Ganymede's rock/iron core, the evolution of the ice mantle has important implications for the behavior of the core — and hence for Ganymede's magnetic field (Kivelson et al. 1996). We discuss these at the end of Section 5.7.

5.3 Model assumptions

We use the model of Malhotra (1991) for the orbital dynamics and tidal evolution of Io, Europa, and Ganymede near the Laplace resonance. The model uses a pertur-

bative expansion of the satellite gravitational interactions with secular and resonant terms up to second order in the satellite eccentricities; the perturbations due to the first two gravitational harmonics of Jupiter are also included. Tidal dissipation in the satellites and Jupiter is parameterized by the ratio Q/k of the tidal dissipation function to second degree Love number of each body. These ratios were free parameters in Malhotra's (1991) study. The equations of motion are obtained in a set of canonical variables which facilitates the construction of an algebraic mapping. This significantly speeds up numerical simulation of the system's long term evolution compared to conventional ODE integration schemes.

Even with the mapping method, numerical simulations with realistic values $Q_J \sim 10^5$ require prohibitively long computation times. We thus run the orbital model using $Q_J = 100$, which speeds up the evolution by a factor $Q_{J_{real}}/Q_{J_{computation}} \sim 10^3$. It is expected (but not rigorously proven) that when the ratios of satellite Q/k to Q_J are specified, the orbital dynamics is exactly the same, but proceeds $\sim 10^3$ times faster. We assume that the large, rapid changes in Q/k Ganymede undergoes (which we have speeded up by a factor of $\sim 10^3$ in the orbital model) do not affect the expected adiabaticity of the orbital evolution; see Malhotra (1991) for discussion.

Nowhere in the orbital model is $Q_{J_{real}}$ specified. However, our thermal model specifies the actual value of Ganymede's Q/k, not a ratio to Q_J. Furthermore, convective cooling rates depend on actual time. In the coupled orbital-thermal model, therefore, we must specify $Q_{J_{real}}$, in order to fix the actual time axis. We use $Q_{J_{real}} = 3 \times 10^5$.

Our Ganymede interior model calculates both geophysical parameters (such as the size of the ocean) and Q/k over time; we feed the latter into the orbital part of the model. Thus, Ganymede's Q/k is no longer a free parameter (as in Malhotra 1991), but is determined by our thermal model. The Q/k of Io, Europa, and Jupiter are still free parameters.

The concept of the Ganymede model is as follows. By specifying satellite composition and temperature with depth at a given time, we can determine the physical structure (sizes of ice layers and internal oceans). By assuming a model for $Q(T)$ in ice and using the satellite physical and thermal structure, we can calculate the

effective Q/k. Given the eccentricity from the orbital model, this specifies the dissipated power through equation (1). Coupled with a method for calculating heat loss to space, we can estimate the net heat source or sink within Ganymede, and can then determine how the temperature profile (and therefore physical structure) changes over time. Because the model for Q is so unconstrained, we keep the rest of the thermal model simple.

Here we describe the Ganymede physical model:

i. Bulk properties

We assume a differentiated Ganymede, consisting of a pure water mantle overlying a rock/iron core. The mass, radius, and gravity (taken to be constant with depth) are 1.5×10^{23} kg, 2640 km, and 1.5 m sec^{-1}. We assume that the ice mantle comprises half of Ganymede's mass.

The assumption that Ganymede entered the resonance in a differentiated state is consistent with available constraints. The Galileo gravity data imply that Ganymede is strongly differentiated at present (Anderson et al. 1996). Thermal models including accretional and radiogenic heating suggest differentiation early in Ganymede's history (Schubert et al. 1981, McKinnon and Parmentier 1986). Further, Ganymede's outer layers must have differentiated *before* dark terrain formation. If not, then the crust underlying dark terrain would be primordial and of density ~ 1.6 g cm^{-3}. These dense regions, overlying the clean, differentiated ice mantle, would be unstable and would founder over geologic time. The idea that the crust cannot support such large density contrasts is bolstered by the low topography on Ganymede. Therefore, the dark terrain must have a density comparable to that of clean ice, implying differentiation of the outer layers. (The fact that Ganymede's dark terrain has half the crater density of Callisto, despite a higher impactor flux at Ganymede, suggests ancient resurfacing of Ganymede's dark terrain and is consistent with an early differentiation event.) Once differentiation initiates, the heat it produces generally drives it to completion (Friedson and Stevenson 1983). We therefore infer that Ganymede was massively differentiated at or before dark terrain formation 3.5 – 4 billion years ago.

ii. Water physical data

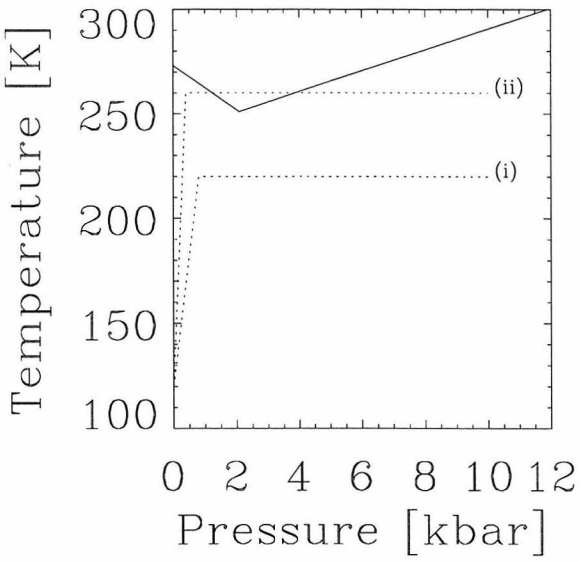

Figure 5.2: The water ice melting curve used in the Ganymede thermal model (solid line). Overlain on the melting curve we show two sample model temperature profiles (dotted lines). Each contains a conductive lithosphere and thermal boundary layer, underlain by an isothermal convective region. Case (i) corresponds to a solid Ganymede and case (ii) represents a Ganymede with an internal liquid ocean bounded above and below by ice layers.

We assume a simplified ice melting curve as shown in Fig. 5.2 (solid line). Each branch of the curve is linear with pressure, and the curve contains one kink, representing the ice I-III-liquid triple point at 2.08 kbar and 251 K. The region to the left of the kink represents the ice I field, and that to the right represents the field of high-pressure polymorphs, ice III, V, and VI.

We use the data on the physical properties of water given in Table 5.1. (c_p is specific heat at constant pressure, L is latent heat of melting, ρ is density, α is thermal expansivity, κ is thermal diffusivity, dT_m/dp is the slope of the melting curves in Fig. 5.2, and μ is the rigidity.) Because we do not explicitly distinguish between ices II, III, V, or VI, the table shows data for the phases ice I, liquid water, and "high-pressure ice." All the parameters are taken to be constant with pressure.

iii. Satellite thermal and physical structure

We assume Ganymede's ice mantle undergoes solid state convection, and that

Table 5.1: Water physical data used in model

	Liquid	Ice I	High Pressure Ice
$c_p(\mathrm{J\,kg^{-1}\,K^{-1}})$	4218	2000	2000
$L(\mathrm{J\,kg^{-1}})$	–	3×10^5	3×10^5
$\rho(\mathrm{kg\,m^{-3}})$	1000	1000	1000
$\alpha(\mathrm{K^{-1}})$	–	1.5×10^{-4}	–
$\kappa(\mathrm{m^2\,sec^{-1}})$	–	10^{-6}	–
$dT_m/dp(\mathrm{K\,Pa^{-1}})$	–	-1.0577×10^{-7}	5×10^{-8}
$\mu(\mathrm{Pa})$	0	4×10^9	4×10^9

there is a rigid, thermally conductive lithosphere at the surface, underlain by a thermally conductive boundary layer and an adiabatic zone which together comprise the convective region. The adiabatic zone is assumed isothermal; call this temperature T_c.

Based on the phase diagram and temperature profile, two different internal structures for Ganymede exist (dotted lines in Fig. 5.2). For $T_c < 251\,\mathrm{K}$, the entire mantle is frozen. For $T_c > 251\,\mathrm{K}$, the mantle consists of an uppermost ice layer (ice I), an internal ocean, and a lowermost ice layer (high pressure ice polymorphs). Specifying T_c specifies both the upper and lower depths of the ocean and the thickness of the uppermost ice layer: i.e., the whole mantle structure.

Assuming an isothermal convection zone below the upper boundary layer should be fine if no melting has occurred. The expected adiabatic temperature increase across the $\sim 10^3\,\mathrm{km}$ deep ice mantle is $\sim 10\,\mathrm{K}$. Any temperature discontinuities caused by layered convection or phase changes are $\sim 10\,\mathrm{K}$ as well. These temperature variations are negligible given our uncertainty in tidal Q.

The assumption of a convecting, isothermal region is not so obvious if internal melting occurs. In absence of convection, tidal heating in ice I would produce a temperature profile following the melting curve. (Darcy's law predicts rapid drainage of the melt water to the ice I-III interface.) This profile is locally *stable* to convection. However, the extreme coldness of the boundary layer should allow strongly

non-local convection from above, driving the temperature profile toward a dry adiabat. The convective overturn time is less than the timescale for major temperature changes (discussed later), so relaxation to the dry adiabat seems reasonable. We thus tentatively conclude that convection will occur, an isothermal temperature profile is reasonable, and discrete oceanic and solid ice layers (rather than partially molten regions) comprise the relevant structure when internal melting occurs.

We do not model the detailed evolution of the rock/iron core, since this is unimportant for evolution of the ice mantle.

iv. Heat source

To determine the heat source from Eq. (5.1), we need to determine the "effective" Q/k for the whole satellite, which we obtain by assuming Q and k are local quantities and volume averaging their ratio k/Q over the satellite. Although k is not strictly a local quantity, most of the tidal energy dissipation takes place near the surface of the satellite, so the error involved in this formulation should not be large compared to other uncertainties.

The Q of all materials is poorly understood, particularly at tidal frequencies. However, we expect that warming promotes creep in ice and accordingly lowers Q. In warm ice, unlike rock, tidal periods are close to the Maxwell time, so creep is plausible for the anelastic portion of the response. We therefore assume that the Q of ice is determined by the Maxwell model (Ojakangas and Stevenson 1989):

$$Q = \frac{1 + (n\tau_M)^2}{2n\tau_M}, \tag{5.2}$$

where $n = 1.0 \times 10^{-5}\,\mathrm{sec}^{-1}$ is Ganymede's mean motion and $\tau_M \equiv \eta/\mu$ is the Maxwell time. $\mu = 4 \times 10^9\,\mathrm{Pa}$ is the rigidity of ice, and η is the local ice viscosity. The temperature dependence of η is

$$\eta = \eta_0 \exp\left[A\left(\frac{T_m}{T} - 1\right)\right], \tag{5.3}$$

where T_m is the local melting temperature, T is the local actual temperature, and η_0 is the melting-point ice viscosity. We treat η_0 as a free parameter, with magnitude 10^{13} –

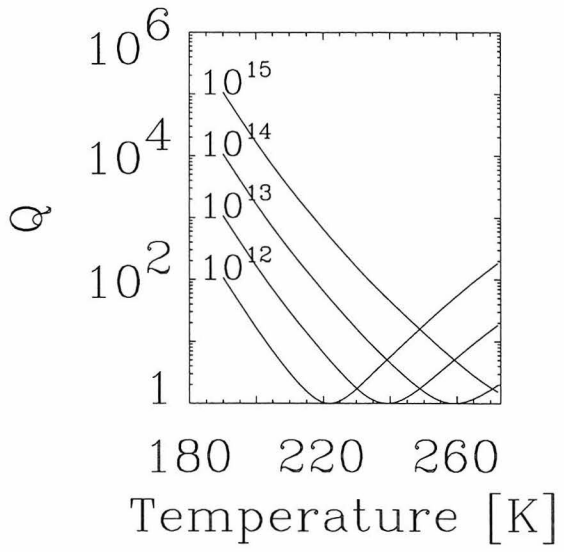

Figure 5.3: Ice $Q(T)$ used in thermal model, as determined by the Maxwell model, Eq. (5.2)-(5.3). We use $A = 26$, and show four curves, for η_0 from $10^{12} - 10^{15}$ Pa sec.

10^{15} Pa sec, the expected range for small grain sizes ($\sim$ 1 mm; Kirk and Stevenson 1987). We use $A = 26$ (Weertman 1973).

Sample $Q(T)$ curves predicted by Eqs. (5.2) and (5.3) are shown in Fig. 5.3 for values of η_0 from $10^{12} - 10^{15}$ Pa sec. The low temperature behavior allows runaways.

When Ganymede is frozen, we estimate k from the formula for a homogeneous satellite (Munk and MacDonald 1960)

$$k = \frac{3/2}{1 + \frac{19\mu}{2\rho g R}} \tag{5.4}$$

where μ is the shear modulus, ρ is the density, g is surface gravity, and R is the satellite radius. Since the material in the tidal bulge is icy, we use $\rho = 1000\,\mathrm{kg\,m^{-3}}$ and $\mu = 4 \times 10^9$ Pa, appropriate to ice. This gives $k = 0.14$ for a frozen Ganymede. (We assume k/Q is zero in the rock core.)

When the ocean forms, however, the situation becomes more complicated. Ganymede would then have at least four layers: the outer ice shell, ocean, inner ice shell, and rocky core (which may be further differentiated into silicate and iron

layers). The exact deformation of such a body under a variable tidal potential is extremely complex and depends on the rigidity, density, viscosity, and location of each layer. Although this full problem has not been attempted, simpler two-layer problems have been solved by Dermott (1979) and Peale and Cassen (1978); these studies can provide insight. Dermott (1979) showed that for a body consisting of an ocean overlying a solid elastic core, the effective Love number for the solid layer is

$$k = \frac{\frac{3}{2}\left(1 - \frac{\rho_w}{\rho}\right)}{1 - \frac{\rho_w}{\rho} + \frac{19\mu}{2\rho g R_c}\left(1 - \frac{3\rho_w}{5\rho}\right)}$$

where ρ_w is the ocean density, g is gravity at the core-ocean interface, and ρ, μ, and R_c are the core density, rigidity, and radius respectively. Considering the "core" to be the high pressure ice phases (which typically have densities 10% greater than liquid water at the same pressure), $k \approx 0.04$. Because the ice is near melting temperature, however, viscous creep may be as (or more) important than elastic strain, so the actual tidal deformation is likely to be greater.

Peale and Cassen (1978) explored two-layer models consisting of an elastic outer shell overlying a liquid core, and solved for the deformation in the case where the two layers have equal densities. They found that the effective Love number depends on the shell thickness. For thin shells, the shell's strength is negligible relative to the gravitational force driving the material to an equipotential. The effective Love number is then just 1.5, the value for a fluid planet (obtainable from Eq. (5.4) using $\mu = 0$.) Thick shells are strong enough to resist the gravitational force and have lower values of k. Peale et al. (1979) demonstrated that for Io the transition between the two regimes occurs for shell thicknesses of $\sim$ 20% the satellite radius, and the transition thickness for Ganymede is probably greater because the rigidity of ice is ten times less than that of rock. Since Ganymede's ice I layer is only 6% of the satellite radius at ocean formation, we therefore expect that the Love number will discontinuously rise to values near 1.5 when the ocean forms.

Ross and Schubert (1987) explored three layer models for Europa, consisting of an outer ice shell, ocean, and rocky core, each with different densities and rigidities.

They found that the tidal deformation for the thin outer shell is half that predicted by Peale and Cassen's model because the low density and small mass of the outer layers (relative to the core) allows only minimal amplification of the bulge size by self-gravitation. Further, the perturbing effect of the *core's* bulge on the ice shell is small simply because the high rigidity limits the core bulge size. For Ganymede, however, we expect k to be much closer to the Peale and Cassen prediction because the ice mantle is much thicker.

We adopt a highly simplified scheme for calculating k when an ocean exists. We assume that $k = 1.5$ in the ice I layer and continue to use $k = 0.14$ in the lower ice layer; k/Q is taken to be zero in the rock core and ocean, as dissipation is expected to be low there. We then volume average k/Q over the satellite for use in calculating the heat source from Eq. (5.1). This approach, of course, is not rigorous and may be in error by up to a factor of a few. Despite the lack of precision, however, our approach is justified by the fact that Q has uncertainty of one to two orders of magnitude. Further, more rigorous calculation would not necessarily improve the accuracy in k. For example, lack of knowledge about salts and other impurities creates uncertainty in the temperature of ocean formation and the density difference between the ocean and ice layers, both of which affect k.

The Maxwell model has the deficiency that it predicts arbitrarily large increases in Q with decreasing temperature. In real ice, dissipation mechanisms other than steady state creep doubtless prevent this. Accordingly, we terminate the growth of Q/k above 2000, corresponding to $Q \sim 300$ for reasonable k.

We ignore radiogenic heat output and secular cooling or warming of the core. The neglect of radiogenic heat is reasonable if runaways occur over a few $\times 10^8$ years or less.

v. Heat loss

We use the parameterized convection scheme of Friedson and Stevenson (1983) to calculate the convective heat flux over time in a planet with no plates and strongly temperature-dependent viscosity. Recent theoretical work (Solomatov 1995) supports such scaling, first applied to the icy satellites by Reynolds and Cassen (1979).

The convective flux is given by

$$F_{conv} = c\frac{k_t \Delta T}{d} Ra^{1/3} \tag{5.5}$$

where k_t is thermal conductivity, d is the depth of the convecting layer, ΔT is the temperature drop across the convecting region (equal to the temperature drop across the convective boundary layer in our model, since the adiabat is isothermal and the lower boundary layer is assumed negligible), c is an independent parameter, and the Rayleigh number Ra is given by

$$Ra \equiv \frac{g\alpha\rho\Delta T d^3}{\kappa\eta_{1/2}} \tag{5.6}$$

Here g is gravity, α is thermal expansivity, ρ is density, κ is thermal diffusivity, and $\eta_{1/2}$ is the viscosity evaluated at a temperature half-way across the boundary layer. We use $c = 0.1$, which implies a critical Rayleigh number of $\sim 10^3$. This choice of c is compatible with Solomatov (1995) to within a factor of two. We evaluate ΔT by assuming the system adjusts ΔT to maximize F_{conv} for a given T_c (Friedson and Stevenson 1983). This gives

$$\Delta T = 2\{b - [b^2 - T_c^2]^{1/2}\}, \tag{5.7}$$

where $b \equiv T_c + AT_m/8$. Finally, we find that

$$F_{conv} = ck_t \left(\frac{g\alpha\rho}{\eta_{1/2}\kappa}\right)^{1/3} (\Delta T)^{4/3}, \tag{5.8}$$

with ΔT given by (5.7). The convected flux is independent of the depth of the convecting region, so Eq. (5.8) applies whether or not Ganymede contains an internal ocean. The scheme assumes, however, that the convecting depth is much greater than the boundary layer thickness. When the ice I layer becomes so thin that $Ra < 1000$, we assume the heat is conducted out.

vi. Time evolution of thermal state

The internal heating rate for the satellite is

$$\frac{dE}{dt} = \frac{21}{2}\left\langle \frac{k}{Q} \right\rangle \frac{GM_J^2 R^5 n e^2}{a^6} - 4\pi R^2 F_{conv}, \tag{5.9}$$

where the first term is the tidal dissipation from Eq. (5.1), with a volume average of k/Q over the satellite.

When Ganymede is completely frozen, the change in T_c over time is related to the change in internal energy by

$$\frac{dE}{dt} = M_i c_{p_i} \frac{dT_c}{dt} \tag{5.10}$$

where M_i is the mass of ice in Ganymede (7.5×10^{22} kg for the frozen state model), and c_{p_i} is the specific heat of ice. When Ganymede contains an ocean, we must consider the latent heat of melting and the different specific heats of liquid water and ice. The change in internal energy over time is then

$$\frac{dE}{dt} = [M_w c_{p_w} + M_i c_{p_i}]\frac{dT_c}{dt} + L\frac{dM_w}{dt}, \tag{5.11}$$

where M_w is the mass of liquid water, L is the latent heat, and c_{p_w} is the specific heat of liquid water. The first term accounts for warming of the water, the second for warming of the ice, and the third for melting ice. (We assume L is the same for ice I and high pressure ice; Table 5.1 lists the assumed values of L, c_{p_i}, c_{p_w}, and ρ). The rate of growth of the ocean, dM_w/dt, is given by

$$\frac{dM_w}{dt} = \frac{4\pi}{g}\frac{dT_c}{dt}\left[r_u^2\left(\frac{-dp}{dT_m}\right)_1 + r_l^2\left(\frac{dp}{dT_m}\right)_{hp}\right] \tag{5.12}$$

where T_m is the local melting temperature. r_u is the radius at the ocean-ice I interface, and r_l is the radius at the ocean-high pressure ice interface; the subscripts "1" and "hp" refer to ice I and high-pressure ice. Using equations for the melting curves and hydrostatic equilibrium, we then obtain r_u and r_l as functions of T_c. These relations, plus Eq. (5.11), (5.12), and the two constraints $M_w = 4\pi\rho(r_u^3 - r_l^3)/3$ and $M_i = 0.5M - M_w$, where M is Ganymede's mass, then constitute a relation between dE/dt and dT_c/dt for a molten Ganymede. The analogous expression for

a frozen Ganymede is simply Eq. (5.10). Therefore Eq. (5.9) is transformed to an ordinary differential equation in $T_c(t)$, which is coupled to those for the orbital evolution through the semi-major axis and eccentricity factors in the first term. We assume that we never melt all of either the ice I or high pressure ice (i.e., that we always have the latent heat term in the molten state) and neglect the solid-solid latent heats of transition, the largest of which (ice II-III) is roughly 20% of the solid-liquid latent heat.

5.4 Model results

To perform a simulation, we must specify initial values for ω_1, ω_2, and T_c, as well as the values of the parameters η_0, c, and the Q/k for Io and Europa. We perform runs for two sets of orbital initial states. The first set starts at $\omega_1 = -6.2^\circ\,\mathrm{day}^{-1}$ and $\omega_2 = -2.65^\circ\,\mathrm{day}^{-1}$, with initial $\omega_1/\omega_2 \approx 2.3$. Thus, we begin the system just short of the $\omega_1/\omega_2 \approx 2$ resonance, so that the system encounters this Laplace-like resonance in the first $\sim 10^8$ years of evolution. (This allows convenient systematic study of the runaway, since we can better specify T_c just as the resonance is starting. However, the system need not enter resonance so early.) We use $(Q/k)_{Io}/(Q/k)_J = 4 \times 10^{-4}$ and $(Q/k)_{Europa}/(Q/k)_J = 4 \times 10^{-3}$, which yield reasonable values of Q for the expected k for these satellites. (The low value for $(Q/k)_{Io}$ is required for capture into $\omega_1/\omega_2 \approx 2$; Showman and Malhotra 1997).

For the second set, we start at $\omega_1 = -4.7^\circ\,\mathrm{day}^{-1}$ and $\omega_2 = -8.0^\circ\,\mathrm{day}^{-1}$, so that $\omega_1/\omega_2 \approx 0.6$. In this case, the system encounters the $\omega_1/\omega_2 = 1/2$ resonance. We use the same $(Q/k)_{Europa}$ as above, but use $(Q/k)_{Io}/(Q/k)_J = 1.1 \times 10^{-3}$. This is the value Io would have at present if its present eccentricity were constant in time. Both resonances can lead to the Laplace resonance and are therefore plausible paths to the current state (Showman and Malhotra 1997, Malhotra 1991).

In each of these two sets of runs, we used $\eta_0 = 10^{13}, 10^{14}$, and 10^{15} Pa sec, and a range of values for initial $T_c(t = 0)$.

Three general types of model behavior were found, exemplified by the three runs

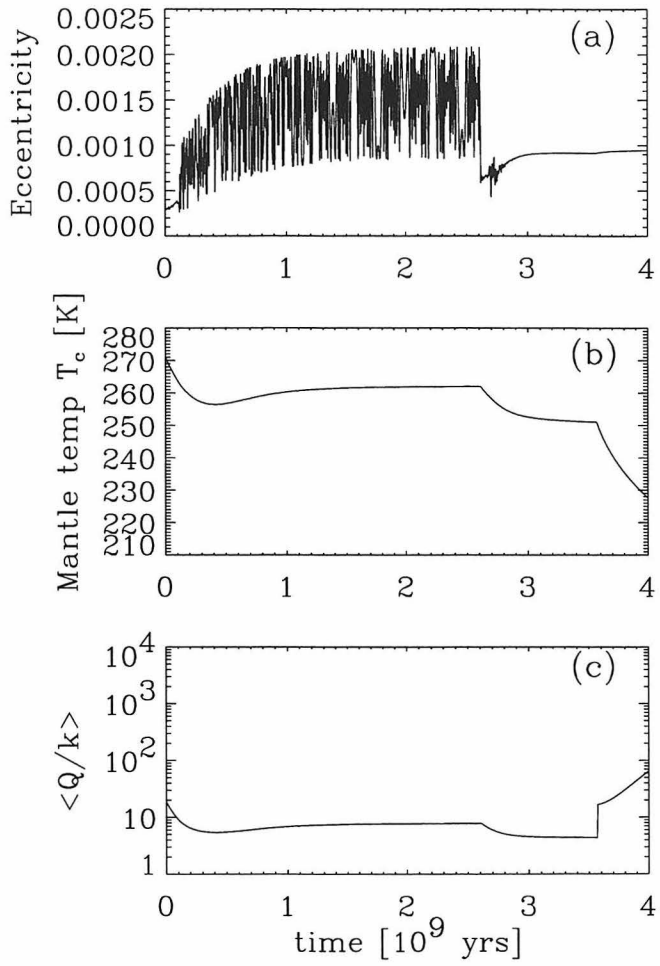

Figure 5.4: Results of a run from the Ganymede coupled orbital- thermal model. (a) Ganymede's eccentricity, (b) Ganymede's ice mantle temperature T_c, and (c) Ganymede's effective Q/k vs. time for 4 billion years of evolution (the time axes in all three plots are the same). In this run the system passes through the $\omega_1/\omega_2 \approx 2$ resonance before capture into the Laplace resonance at 2.6 Ga. The final state in this run thus resembles that of the modern state. No radiogenic heating is included. In this run, Ganymede has begun warm ($T_c = 271\,\mathrm{K}$), and no runaway occurs.

displayed in Figs. 5.4, 5.5, and 5.6. All three runs passed through the $\omega_1/\omega_2 = 2$ resonance, followed by capture into the Laplace resonance; they differed only in the initial temperature T_c of Ganymede. In each of the figures, panel (a) shows the time evolution of Ganymede's eccentricity, (b) shows Ganymede's mantle temperature T_c, and (c) shows Ganymede's effective Q/k. (Because we have assumed an isothermal adiabat, the entire state of the mantle at a particular time corresponds to a single value of T_c.) In all panels, the time axes are the same, $t = 0$ to 4×10^9 years.

In Fig. 5.4, Ganymede starts warm, with initial $T_c = 271$ K, implying existence of a large internal ocean. Q/k thus starts low, so the resonance is never able to pump the eccentricity to a high value: the maximum eccentricity attained is 0.002 (Fig. 5.4a). Thus, runaway is not possible. From Fig. 5.4b, the temperature can be seen to reach a steady state (at ~ 2 Ga) in which convective cooling balances dissipative heating. (The ice I layer is 80 km thick and the ocean is several hundred km deep at this time.) At 2.6×10^9 years, $(Q/k)_{Io}/(Q/k)_J$ (an imposed free parameter) is increased by a factor of six to 1.9×10^{-3}, disrupting the $\omega_1/\omega_2 \approx 2$ resonance and leading to capture into the Laplace resonance (see Showman and Malhotra 1997). Thereafter, the satellite cools monotonically. The kink in T_c at 3.6 Ga corresponds to freezing of the ocean, at which point latent heat buffering ceases. The mean tidal heating rate during the resonance was roughly 10^{12} W.

In Fig. 5.5, the satellite starts cold and frozen, with $T_c = 170$ K. Q/k is high, and tidal energy dissipation is small. The increase in dissipation caused by increasing e is not enough to change the temperature significantly during the resonance: the internal temperature is nearly constant throughout the evolution. Thus, no runaway has occurred, and the mean dissipation remains low. At 2.6×10^9 years, the system is again disrupted into the Laplace resonance.

In Fig. 5.6, we start Ganymede at an intermediate temperature of 183 K. Q/k starts high enough to allow the eccentricity to rise, but *low* enough that the increase in eccentricity to 0.02 causes some warming. Eventually Q/k begins to decrease. The warming then accelerates, and a runaway occurs. The temperature warms by ~ 65 K, and an ocean several hundred km deep forms. In this example, about half

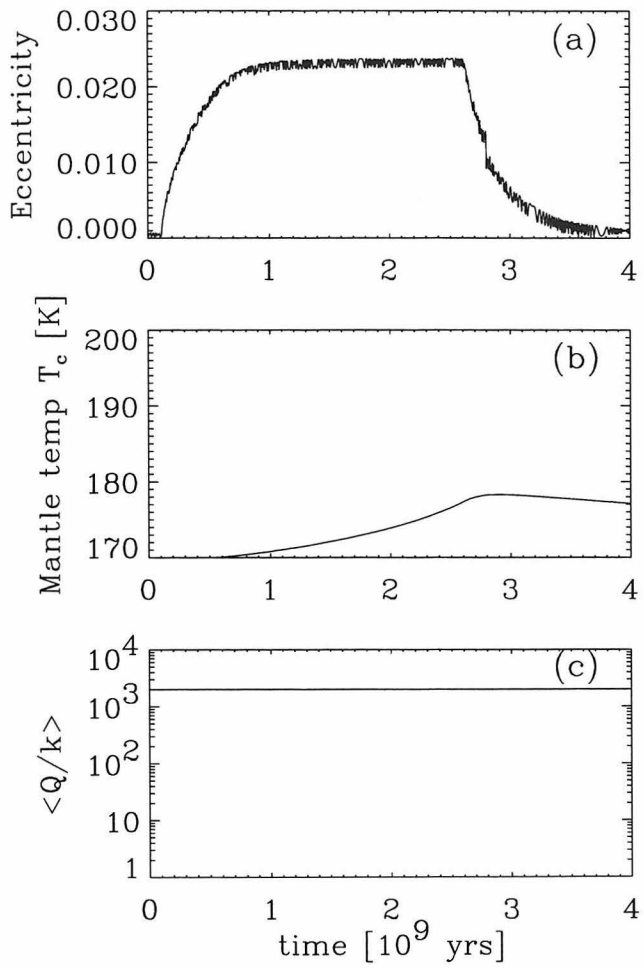

Figure 5.5: Same as Fig. 5.4, but for a colder initial mantle temperature of T_c = 170 K. In this run, Ganymede has begun too cold, and no runaway occurs.

of the temperature increase occurs in 10^7 years. In Fig. 5.6 the $\omega_1/\omega_2 \approx 2$ resonance continues to exist after the thermal runaway has occurred; the resonance does not end until 2.6×10^9 years (again triggered by an increase in Q_{Io}), at which time the Laplace resonance is established. The $\omega_1/\omega_2 \approx 2$ resonance is thus stable against large changes in the Q/k of Ganymede; this is true of $\omega_1/\omega_2 \approx 3/2$ and $1/2$ as well. The minimum ice I thickness (which occurs just before 2.6 Ga) is ~ 80 km. Note that the eccentricity after the runaway is comparable to that in Fig. 5.4, because Q/k is roughly the same.

The runaway magnitude (quantified by the temperature rise) and the runaway timescale both vary with initial T_c. Figs. 5.7a-b summarize our results for two Laplace-like resonances, $\omega_1/\omega_2 \approx 2$ (solid dots) and $\omega_1/\omega_2 \approx 1/2$ (open squares), in runs with a choice of $\eta_0 = 10^{15}$ Pa sec. The timescales shown are the times needed for approximately two-thirds of the temperature rise to take place. Runaways can occur in the $\omega_1/\omega_2 \approx 3/2$ resonance, as well; these are slightly weaker than those with $\omega_1/\omega_2 \approx 2$.

Several features are evident. First, the largest runaway causes ~ 70 K warming, and a continuum of smaller runaways exist. Second, the shortest runaway occurs in just over 10^7 years, and a continuum of slower runaways exist. Third, timescale is inversely correlated with the magnitude: the shortest runaways are also the largest. The thickness of the ice I layer is roughly ~ 130 km immediately after the largest runaways.

We performed runs using $\eta_0 = 10^{13}$ Pa sec and $\eta_0 = 10^{14}$ Pa sec as well. Qualitatively, the results are very similar to those shown in Fig. 5.7, except that the curves are shifted to lower temperatures. In other words, the strongest runaways start at ~ 170 K for $\eta_0 = 10^{14}$ Pa sec and ~ 150 K for $\eta_0 = 10^{13}$ Pa sec, as compared with 190 K for $\eta_0 = 10^{15}$ Pa sec. Therefore, the models with lower melting point viscosity are less likely to produce oceans.

Interestingly, the temperature continues to rise *after* a runaway has occurred in the $\omega_1/\omega_2 \approx 2$ or $3/2$ resonances, eventually reaching a steady state in which surface cooling balances dissipative warming. The minimum ice I thickness therefore often

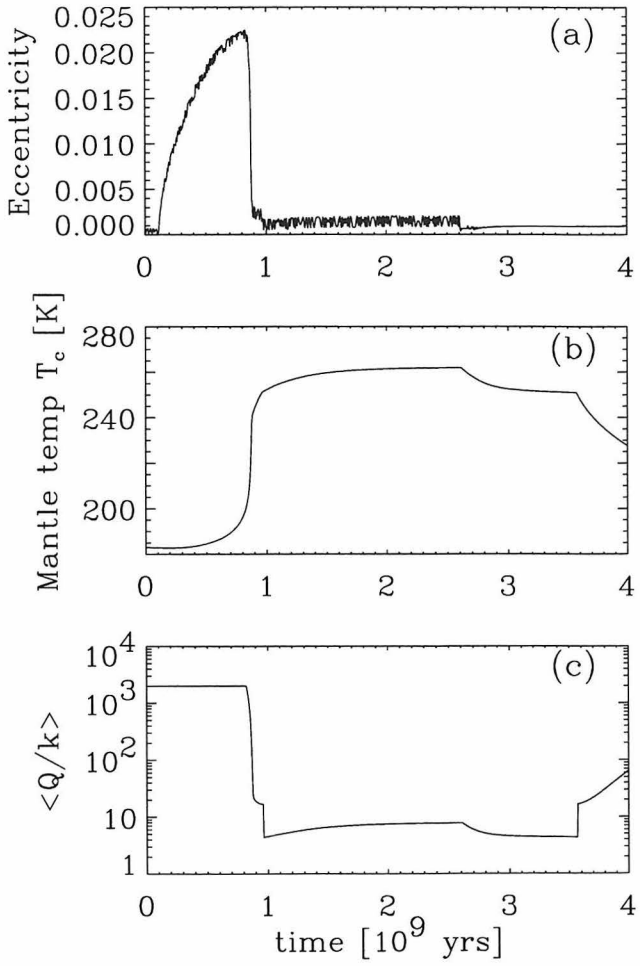

Figure 5.6: Same as Fig. 5.4, but for an intermediate starting temperature of 183 K. In this run, Ganymede's temperature is just right, and a large runaway occurs: Ganymede's mantle warms by ~ 65 K and a large ocean forms in just $\sim 10^7$ years.

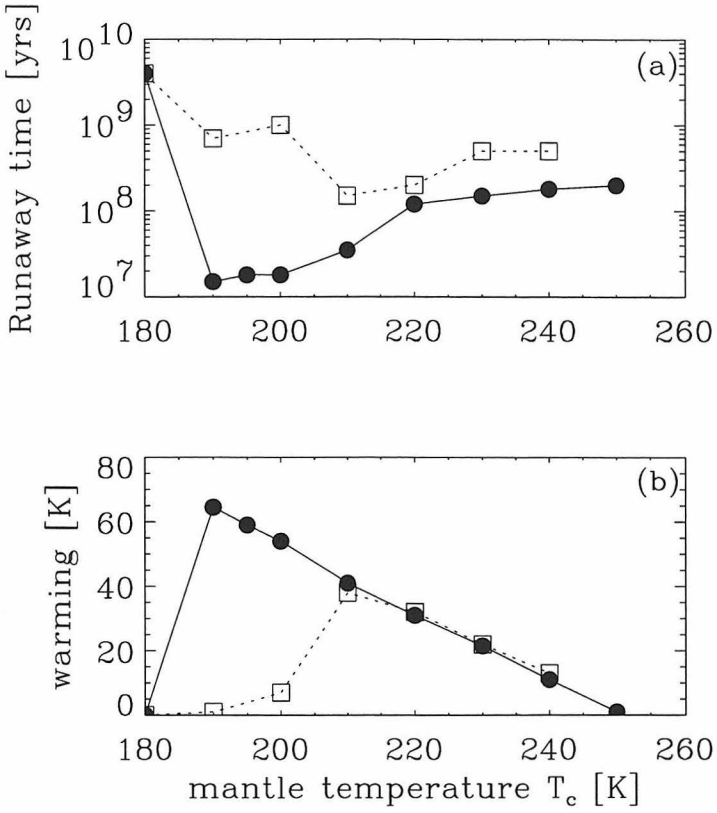

Figure 5.7: Summary of results on thermal runaways from coupled orbital-thermal model. Shows (a) time over which runaway occurs and (b) warming occurring during a runaway, as a function of Ganymede's mantle temperature T_c at the onset of resonance. Each circle or square represents the results of a model run. Filled circles represent runs passing through $\omega_1/\omega_2 \approx 2$, while open squares correspond to runs passing through $\omega_1/\omega_2 \approx 1/2$. All runs use the Maxwell model for $Q(T)$, with the constraint that Q/k not exceed 2000. The runs shown use $\eta_0 = 10^{15}$ Pa sec, $c = 0.1$, and $Q_J = 3 \times 10^5$.

occurs several hundred million years after the runaway. The reason is that for $c = 0.1$, the steady state mantle temperature (for the high tidal dissipation rate in $\omega_1/\omega_2 \approx 3/2$ or 2) is at least 70 K above the temperature needed to initiate large runaways. Since runaways produce less than 70 K warming, the temperature immediately following runaway is colder than the steady state value. If $c \geq$ several $\times 10^{-1}$, however, *cooling* (rather than warming) always follows the runaway, implying that the ice I layer reaches its minimum thickness during runaway. (Assuming values of c greater than 0.1 is equivalent to assuming that ice is softer at convective timescales than tidal flexing timescales; see Eqs. [5.5]-[5.6].)

We assumed $Q_J = 3 \times 10^5$ in all our runs. The runaways would be weaker for larger Q_J and vice versa. For example, if Q_J were near its time-averaged lower limit of a few $\times 10^4$, Ganymede's eccentricity would rise to 0.04 rather than 0.02 before a large runaway (see Fig. 4.7 in this thesis; Showman and Malhotra 1997). The strongest possible runaways would then be four times more energetic than those displayed in Figs. 5.6-5.7, and the steady state ice I thicknesses would be smaller.

The magnitude of tidal flexing at the surface is important for models of resurfacing. According to the models discussed here, $e \sim 0.02$ before a runaway and ~ 0.001 afterward (Fig. 5.6). Conversely, $k \approx 0.14$ before and 1.5 afterward. These conditions imply a tidal strain amplitude of a few $\times 10^{-6}$ or less both before and after runaway. However, *during* a runaway, the ice shell decouples (implying $k = 1.5$) while the eccentricity is still high. The maximum achievable eccentricity at decoupling is ~ 0.01 for the $\omega_1/\omega_2 \approx 2$ resonance. This yields a strain amplitude of 10^{-5} over a period of 10^7 years.

The results in Fig. 5.7 show that large runaways cannot occur unless the mantle temperature is below 200 K at the onset of resonance. However, radiogenic and accretional heating may prevent cooling to such temperatures. We now consider the question of whether Ganymede can cool to $\sim$ 200 K before resonant eccentricity pumping begins. To do this, we must know when resonant heating began.

Traditional crater dating techniques yield ages for Ganymede's grooved terrain of $\sim$ 3.5 billion years (Shoemaker and Wolfe 1982). This age for the cratered terrain

was obtained using a modern cratering rate of $2.3 \times 10^{-14}\,\mathrm{km}^{-2}\,\mathrm{year}^{-1}$ for 10-km diameter craters (Shoemaker and Wolfe 1982), and assuming that the impact rate of comets doubled 0.5 billion years ago (as indicated in the lunar and terrestrial cratering history). However, recently revised estimates yield $1.1 \times 10^{-13}\,\mathrm{km}^{-2}\,\mathrm{year}^{-1}$ for the modern 10-km crater production rate (Shoemaker, personal communication 1995), which suggest ages for the grooved terrain of a billion years or less. The uncertainty in these estimates means that we cannot as yet place a constraint on the time at which tidal heating began.

We consider the most generous scenario, in which resonant heating begins late in solar system history. We therefore wish to determine whether Ganymede can cool to 200 K over solar system history.

We start Ganymede differentiated, with initial $T_c = 270\,\mathrm{K}$ 4.6 billion years ago, and use the Ganymede model with no tidal dissipation (i.e., zero eccentricity). Such a warm starting temperature is suggested by plausible accretion scenarios (McKinnon and Parmentier 1986). We include a core model to account for radiogenic heating since this heat source substantially affects the cooling rate. We run the model for two cases: (1) using carbonaceous chondritic radionuclide abundances for the core rock, and assuming that all radionuclides are contained in the core, and (2) using carbonaceous chondritic abundances, but assuming 30% of the radionuclides were leached into the ocean. If Ganymede rock were ordinary chondritic (i.e., with a K/U ratio close to that of the terrestrial mantle), the radiogenic output would be intermediate between the carbonaceous chondritic cases and that with no radionuclides, since ordinary chondrite is substantially depleted in $^{40}\mathrm{K}$ relative to carbonaceous chondrite.

We use the core model of Kirk and Stevenson (1987). The model assumes carbonaceous chondritic abundances for $^{40}\mathrm{K}$, $^{232}\mathrm{Th}$, $^{235}\mathrm{U}$, and $^{238}\mathrm{U}$. The core initially starts at 270 K, the same as the ice mantle, and gradually warms as the radionuclides decay. Initially, heat is conducted into the ice mantle across a boundary layer of thickness $(\kappa_c t)^{1/2}$, where κ_c is the thermal diffusivity of the core rock. Once the core Rayleigh number reaches 10^3, convection begins. In this regime, the model assumes the core "self-regulates," so that the power released to the ice equals the instanta-

neous radiogenic power production. We use a core rock melting point viscosity of 1.7×10^{16} Pa sec rather than 1.7×10^{13} Pa sec as used by Kirk and Stevenson (1987).

In Fig. 5.8 we show T_c over time resulting from the above model, using $k_t = 4.1\,\mathrm{W\,m^{-1}\,K^{-1}}$ and $c = 0.1$ for the ice mantle model. Panels (a) and (b) correspond to cases (1) and (2) above, and panel (c) corresponds to no radiogenic heating. In each case we show curves for four separate runs, for $\eta_0 = 10^{12} - 10^{15}$ Pa sec. With no radiogenic heating, T_c plummets below 200 K for all four runs, so runaway seems possible if resonance capture were to occur. However, Figs. 5.8a and b show that radiogenic heating prevents the mantle from cooling to 200 K; for $\eta_0 = 10^{15}$ Pa sec, the ocean never freezes. The implication is that large runaways are unlikely if Ganymede's core rock contains carbonaceous chondritic radionuclide abundances, although small runaways (initiated from $T_c \sim 220 - 230$ K) could still occur.

The failure of our model to predict large, ocean-forming global runaways should be taken seriously, and may mean that such runaways are impossible. However, our model contains several major uncertainties. First, our formulation of Q is particularly suspect. We equated viscosities at tidal flexing (one week) and convective overturn (10^7 year) timescales. If ice were 4-5 orders of magnitude softer at convective timescales than at tidal timescales, large runaways would be possible. Alternatively, if additional dissipation mechanisms besides viscous creep cause $Q(T)$ to be strongly temperature dependent near melting, reasonable values of η_0 (10^{12} Pa sec) at convective timescales could allow large runaways. Second, although the work of Solomatov (1995) strengthens our parameterization of convection in the ice mantle, we stress that the formulation is still not rigorous and is subject to uncertainty. Finally, a major depletion of radionuclides in Ganymede's rocky portion would allow sufficient cooling for large runaways to occur, although such depletion is unlikely.

5.5 Effects of runaway: Global expansion

The observation that bright terrain edges are sharp and linear strongly suggests that bright terrain formed in a global system of graben. This interpretation, as well as

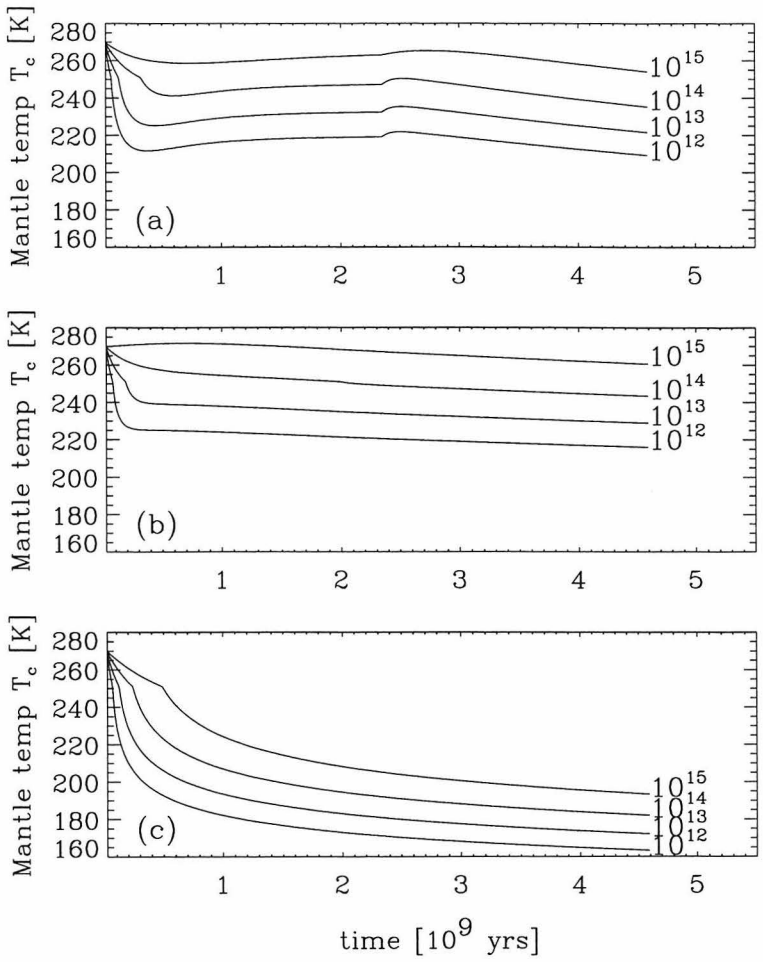

Figure 5.8: Ganymede's mantle temperature T_c over 4.6 billion years, assuming no resonant eccentricity pumping. Uses Ganymede model from Section 5.3 with the rock core model of Kirk and Stevenson (1987). Shows evolution for (a) carbonaceous chondritic radionuclide abundances for rock core, and assuming 100% of radionuclides remain in core, (b) same, but assuming 30% of nuclides have been leached into the ocean and 70% remain in core, and (c) no radiogenic heating. Each panel shows evolution for four model runs, with values of η_0 from $10^{12} - 10^{15}$ Pa sec. With radiogenic heating, the temperature never drops below 200 K. Since large runaways require such low temperatures, they may be impossible.

other geologic features (Parmentier et al. 1982) suggest global expansion. Ganymede thermal models (Schubert et al. 1981, McKinnon and Parmentier 1986) generally predict extensive or complete differentiation early in solar system history. Therefore, any global expansion and lithospheric fracture accompanying differentiation is probably not associated with grooved terrain formation, as suggested by some authors (Squyres 1980).

Although our model does not predict large runaways, the uncertainties of our model, the lack of other processes capable of causing global expansion, and the *success* of our model in predicting small runaways warrant consideration of the effects of runaway. The warming and phase changes during global runaway could cause the inferred expansion.

5.5.1 Expansion caused by melting

Here we consider the expansion undergone by Ganymede in passing from a warm, frozen state (as in Fig. 5.1b) to a state with an internal ocean (as in Figs. 5.1c, d, or e). We calculate only the volume changes that accompany the phase change of ice into liquid water. (Thermal expansion is considered in the next section.) In addition, we neglect the small volume change associated with conversion of ices I and V to ice III as the temperature warms. Under these assumptions, we need not specify the details of temperature with depth in the ice. (However, we will need the oceanic temperature profile.)

We take as initial state a frozen, differentiated Ganymede consisting of a rock core overlain by a pure water ice mantle of ice I, III, V, and VI, corresponding to a mantle temperature of $\sim 240 - 250\,\mathrm{K}$. (At these temperatures, Ganymede cannot contain any ice VII or VIII for reasonable core densities.) We characterize this initial state by specifying pressure with depth. To do this we specify gravity as a function of depth and integrate the hydrostatic equation down from the surface, assuming incompressible ice phases with densities of 0.92, 1.16, 1.27, and 1.31 $\mathrm{g\,cm^{-3}}$ for ices I, III, V, and VI, respectively. The expressions are valid only as long as the core radius

is smaller than the radius in question. With this caveat, however, the expressions are *independent* of core density (and therefore radius). We assume $p(r)$ does not change during the melting process.

Let the local volume change per mass ($\mathrm{m^3\,kg^{-1}}$) from ice i (where $i = 1, 3, 5$ or 6 for ice I, III, V, or VI, respectively) to liquid water be $\Delta v_{il}(p)$. We assume Δv_{il} is linear with pressure and interpolate between values at triple points, using data from Fletcher (1970). Using our $p(r)$ relations, we then obtain relations for $\Delta v_{il}(r)$. We next integrate $\Delta v_{il}(r)$ over the appropriate spherical shell to obtain the volume change of the shell, ΔV_{il}, when that shell has been converted from ice to liquid. The *total* volume change is obtained by summing the volume changes of the individual shells. To calculate the total volume change, we must know the thickness of the ocean as a function of the depth of the ocean-ice I interface.

For a given pressure at the upper surface of the ocean, we can find the pressure at the lower surface by locating the point at which the oceanic adiabat $dT/dp = \alpha T/\rho_w c_p$ crosses the high pressure ice melting curve. The thermal expansivity, α, changes by a factor of several along such an adiabat, while the temperature, T, the density of liquid water, ρ_w, and specific heat, c_p, change by only $10 - 20\%$. We thus approximate the latter three as constant, with values 270 K, $1100\,\mathrm{kg\,m^{-3}}$, and $3900\,\mathrm{J\,kg^{-1}\,K^{-1}}$ (typical of conditions at a few kbar), and take α to be piecewise linear with pressure along the adiabat, with fits to data from Dorsey (1940, pp. 232-233) and Weast (1987). We then solve to obtain $T(p)$ along the adiabat (for a given pressure at the ice I-ocean interface). We equate this temperature to the melting curve of ice III, V, or VI, and solve for the ocean thickness as a function of the depth of the ice I-ocean interface. More detailed calculations, performed using linear fits to c_p and ρ and letting T vary, give relations in good agreement with those described above.

We modify the expressions for ΔV_{5l} and ΔV_{6l} because of the rock core: once pressure at the ocean-high pressure ice interface exceeds the pressure at the rock core-ice mantle boundary, no more melting of high pressure ice can occur, and any continued melting of ice I leads only to satellite *contraction*, not expansion. This affects the way we sum the volume changes ΔV_{il}.

Some data suggest that the room-pressure regime of negative thermal expansivity from $0 - 4°$ C exists also at higher pressure, perhaps following the ice I melting curve, although other data suggest that high pressure thermal expansivity is positive everywhere (Dorsey 1940, p.230). Such a region of negative thermal expansivity (which might comprise the uppermost 10^2 m of ocean for fluxes of 10^{-2} W m^{-2}) would be stable against convection, and would thus act as a thermally conductive boundary layer, increasing interior temperatures for a given external temperature. For a given volume of ice I melted, the volume of high pressure ice melted would be *greater* than that if α were positive everywhere. We considered two cases: assuming (1) thermal expansivity is positive everywhere, so that the adiabat strikes the ice I melting curve directly, and (2) at any pressure along the ice I melting curve, the region between the melting temperature T_m and $T_m + 4$ K is considered to have negative expansivity (equivalent to assuming an oceanic adiabat 4 K warmer than before for a given pressure at the ocean's upper surface).

We plot the final results in Fig. 5.9. There, we show the net satellite volume change from our frozen reference state as a function of ice I layer thickness. (Specifying the ice I thickness determines the ocean's depth and the entire satellite structure, for a given rock core size. The core size is uniquely specified by the core density.) We show the results for both assumptions about thermal expansivity, and for core densities of $\rho_c = 2.5$, 3.0, and 3.5 g cm^{-3} in Figs. 5.9a, b, and c respectively. Expansion is always predicted. Simple calculation shows that if gravity and density are constant with depth, if the area of an infinitesimal spherical shell is constant with depth (i.e., if a "plane-parallel" Ganymede is assumed), if the entropy of transition from ices I, III, V, and VI to liquid are assumed to be equal, and if the oceanic adiabat is isothermal, then the volume change on melting is exactly zero. Relaxing these assumptions leads to a residual volume change. Most importantly, using a realistic adiabat allows more high pressure ice to melt for a given volume of ice I melted than for an isothermal adiabat, leading to net expansion.

For each case, as expected, $\Delta V/V$ is greater when we allow the region of negative α than when α is positive everywhere. For a small core, $\rho_c = 3.5$ g cm^{-3}, the

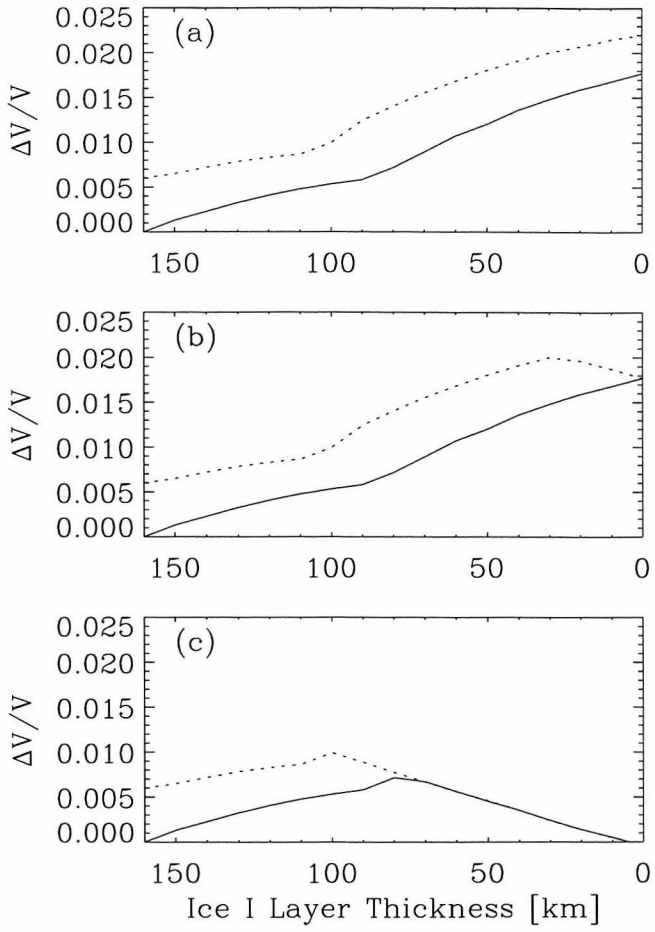

Figure 5.9: Fractional volume expansion occurring in Ganymede because of internal melting, shown as a function of ice I layer thickness, for three core densities: (a) $\rho_c = 3.5\,\mathrm{g\,cm^{-3}}$, (b) $\rho_c = 3.0\,\mathrm{g\,cm^{-3}}$, and (c) $\rho_c = 2.5\,\mathrm{g\,cm^{-3}}$. The expansion is that relative to a frozen reference state, for which the ice I layer is 160 km thick. Each panel displays the results for two cases: (1) assuming thermal expansivity is positive everywhere (solid curve), and (2) assuming a 4 K region of negative expansivity follows the ice I melting curve (dotted curve), which implies a 4 K boundary layer at the top of the ocean. The expansions shown, of order 1-2%, are those that might accompany a large thermal runaway.

expansion peaks at $\sim$ 2% for complete melting of the ice I layer. For a large core ($\rho_c = 2.5\,\mathrm{g\,cm^{-3}}$), however, all the ice VI is gone after only about half of the ice I melts. The expansion thus peaks at $\sim$ 1% and declines with further melting of ice I. In the positive α cases, expansion begins at $\Delta V/V \approx 0.006$. This is because no melting of ice I occurs (except for the 10^2 m boundary layer) until all the ice III and part of the ice V is melted.

Our results differ from those of Squyres (1980) by a factor of several, and have a different dependence on core density. In his pioneering work on the Ganymede-Callisto dichotomy, Squyres calculated that for $\rho_c = 3.5\,\mathrm{g\,cm^{-3}}$ no expansion occurs on melting, and for $\rho_c = 2.5\,\mathrm{g\,cm^{-3}}$ volume expansion is 2.2% if the final ice I thickness is 100 km (3-4 times larger than our calculated expansion for the same final ice I thickness). However, this dependence on core density cannot be correct for a differentiated Ganymede with pure water ice mantle. As long as the core is small enough that some high pressure ice remains, the expansion from a frozen reference state is *independent* of core density. A 100-km thick ice I layer implies that the radius at the ocean bottom is greater than the core radius for $\rho_c \geq 2.5\,\mathrm{g\,cm^{-3}}$. Thus, for relevant core densities, $\Delta V/V$ should be constant with respect to ρ_c for the 100-km final ice I thickness chosen by Squyres (1980).

5.5.2 Expansion caused by solid-solid phase changes and warming

We now calculate the expansion when Ganymede passes from a cold frozen state to a warm frozen state. We assume a differentiated Ganymede with a pure water ice mantle of ice I, II, and VI, at a temperature of $\sim$ 200 K. We take as final state a Ganymede with ices I, III, V, and VI, and assume the same $p(r)$ relations as before.

During the transition, ice II changes to ices I, III, and V. Conversion to ices I and III causes expansion, while conversion to ice V causes contraction. Assuming that the local volume change per mass from ice II to ices I, III, or V are independent of pressure (with values of the triple points taken from Fletcher 1970), we find that

Table 5.2: Ice flow parameters for $T < 195\,\mathrm{K}$

Reference	B	m	Q^*
Kirby et al. (1987)	$1.0 \times 10^{-31}\,\mathrm{Pa}^{-4.7}\,\mathrm{sec}^{-1}$	4.7	$36\,\mathrm{kJ\,mole}^{-1}$
Durham et al. (1992)	$1.0 \times 10^{-35}\,\mathrm{Pa}^{-5.6}\,\mathrm{sec}^{-1}$	5.6	$43\,\mathrm{kJ\,mole}^{-1}$

the expansion largely cancels the contraction. The net expansion/contraction is of magnitude ~ 0.001 or less, which is negligible.

The thermal expansivity of ice I at 250 K is $1.5 \times 10^{-4}\,\mathrm{K}^{-1}$; we adopt this value for all the ice polymorphs. Since essentially all of Ganymede's ice mantle will warm during a runaway, and since Ganymede is roughly half ice by mass, the fractional satellite expansion during a runaway is $\sim 7 \times 10^{-5}$ per K of warming. This gives $\Delta V/V \approx 0.005$ for the largest runaways described in Section 5.4.

5.6 Lithospheric stress

In this section, we calculate the lithospheric stress induced by satellite expansion during a runaway. We assume a steady state strain rate relation of the form

$$\dot{\epsilon} = \frac{\sigma}{\eta} + B\sigma^m \exp\left(-\frac{Q^* + pV^*}{RT}\right), \tag{5.13}$$

where η is the volume diffusion (Newtonian) viscosity, given by Eq. (5.3), p is confining pressure, Q^* is activation energy, and V^* is activation volume. B and m are empirical constants; R is the gas constant. Laboratory experiments suggest $m \sim 3 - 5$ (e.g., Kirby et al. 1987). Note that we neglected the second term in calculating tidal Q and convective heat flow.

Ganymede's surface temperature is roughly 130 K, so for thermal gradients of order $5\,\mathrm{K\,km}^{-1}$, we are interested in temperatures below 200 K if we consider the uppermost 10 km of lithosphere. This corresponds to confining pressures less than 10^2 bars. Recent experiments on the rheology of ice at these temperatures and 500 bars

confining pressure have been performed by two groups (Kirby et al. 1987, and Durham et al. 1983, 1992) who obtain different values for B, m, and Q^*. We use both sets of results (listed in Table 5.2) in our stress calculations and take $\eta_0 = 10^{14}$ Pa sec. Although we are interested in lower pressures than those of the experiments, the pV^* term is negligible for experimentally determined values of V^* (Durham et al. 1983, Jones and Chew 1983).

To find stress as a function of lithospheric temperature, we use the strain rate of Eq. (5.13) in a generalized version of the Maxwell viscoelastic equation:

$$\frac{\dot{\sigma}}{\mu} + \frac{\sigma}{\eta} + B\sigma^m \exp\left(\frac{-Q^*}{RT}\right) = \dot{\epsilon}, \tag{5.14}$$

where μ is the shear modulus. We have simply taken the steady state creep rate and added to it the elastic strain rate to give the total strain rate. Because global expansion does not depend on lithospheric stress, we can independently specify $\dot{\epsilon}$ as a function of time and solve the differential equation to find the maximum value of stress at a given temperature. We take $\dot{\epsilon}$ to have a Gaussian form:

$$\dot{\epsilon} = \left(\frac{\Delta V}{3V}\right) \frac{1}{\tau\sqrt{\pi}} \exp(-\frac{(t-3\tau)^2}{\tau^2}), \tag{5.15}$$

where t is time, τ is the characteristic expansion timescale and $\Delta V/V$ is the fractional volume expansion. Then, at any time t, the cumulative linear strain is $(\Delta V/3V)\,\mathrm{erf}(t/\tau)$, which is just $\Delta V/3V$ as $t \to \infty$. We solve Eq. (5.14) starting at $t = 0$ (three standard deviations away from the peak), and use $\Delta V/V = 0.02$.

Fig. 5.10 shows the peak stress as a function of depth using the flow parameters of Durham et al. (1992), for expansion timescales of $\tau = 10^6$ to 10^8 years. Panels (a), (b), and (c) show the results for surface temperatures of 130 K, 110 K, and 90 K respectively. (The latter may be relevant since the sun was less luminous several billion years ago, and is relevant at high latitudes on Ganymede even with current solar heating.) We assume a thermal gradient of $5\,\mathrm{K\,km^{-1}}$. The different curves in each panel correspond to stresses attained for different expansion timescales, marked in the figure. We also show the hydrostatic pressure with depth (dotted lines); the

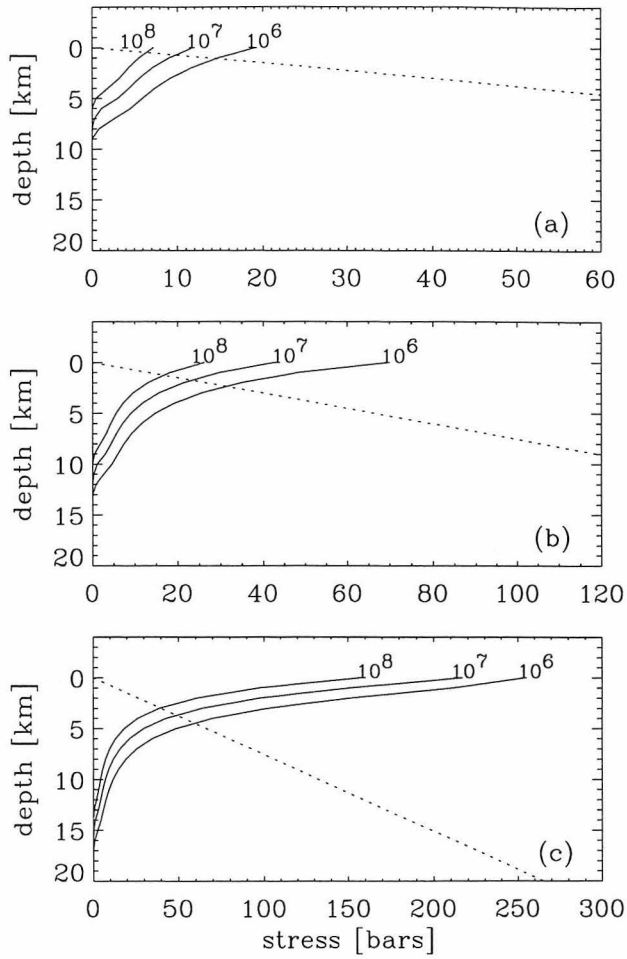

Figure 5.10: Lithospheric stress vs. depth occurring for a volume expansion of 2%, using flow parameters of Durham et al. (1992), for the expansion times shown in the plots (years). Assumes $dT/dz = 5\,\mathrm{K\,km^{-1}}$. Dotted line is hydrostatic pressure. (a) Surface $T = 130\,\mathrm{K}$, (b) surface $T = 110\,\mathrm{K}$, and (c) surface $T = 90\,\mathrm{K}$. Note the different horizontal scales. The stresses shown imply cracking to several km depth during a large thermal runaway.

intersection between this curve and $\sigma(z)$ depicts the maximum depth of open fracture for ice with zero strength (the actual tensile strength may be $\sim 10 - 30$ bars; Kirk and Stevenson [1987], Squyres [1982]). These results show that open cracks could occur to a depth of a few km, and might cause the inferred graben. Cracks could conceivably propagate to a greater depth.

Stresses calculated using Kirby et al.'s rheology are at most $\sim 30\%$ lower than those calculated using Durham et al.'s (1992) data. Increasing the value of B by an order of magnitude to account for the possibility of particulate contamination in the ice, as suggested by Durham et al. (1992), has only a minor effect on the results.

5.7 Conclusions

The mean frictional heating Ganymede undergoes within the eccentricity pumping Laplace-like resonances is generally quite low, and exceeds primordial radiogenic heating only for particular choices of poorly known parameters (e.g., Q_J, the tidal Q of Jupiter). It is therefore unclear how resurfacing would occur on Ganymede but not Callisto, since at first glance resonance passage appears to have only a secondary effect on Ganymede's thermal evolution. However, frictional heating is qualitatively different than radiogenic heating because it can depend on the thermal state. Non-linear effects are therefore possible wherein the heating rate varies in time, far exceeding radiogenic heating during short time intervals. This would place Ganymede's thermal history in a qualitatively different regime than Callisto's and might allow resurfacing. Our goal has been to explore this phenomenon under "garden-variety" scenarios in which mean tidal heating is below primordial radiogenic heating. We have extended the models of Malhotra (1991) and Showman and Malhotra (1997) for the orbital evolution of the Galilean satellites to include the thermal evolution of Ganymede. For plausible dependence of tidal Q/k on temperature, thermal runaway events can occur in Ganymede during tidal evolution preceding capture into the Laplace resonance. We have explored such runaways for the $\omega_1/\omega_2 = 1/2$, $3/2$, and 2 Laplace-like resonances. Runaway timescale and magnitude vary sensitively on the details of the

model for $Q(T)$ and the initial temperature, but a wide range of initial conditions can lead to runaway.

Convective cooling over billion year timescales appears insufficient for Ganymede to reach the ~ 200 K temperatures needed for large runaways, for carbonaceous chondritic radionuclide abundances in Ganymede's rock. Thus, large runaways cannot occur if our model is correct, but small runaways are possible. (Scenarios in which Ganymede is "too cold" for runaway — depicted in Fig. 5.5 — are therefore also ruled out.) Different parameterizations of tidal Q or convective heat flow could allow large runaways.

Massive melting of Ganymede leads to a fractional volume expansion of 1-2%, assuming reasonable core densities. Thermal expansion for the largest runaways is 0.5%. Additional expansion may occur if differentiation is not complete when the runaway begins. The total expansion expected *if* a large runaway can occur is thus $\sim 2-3\%$. Surface stresses caused by 2% expansion over $10^6 - 10^8$ years are $\sim 10^2$ bars at the surface, and drop to a few bars at several km depth.

There are several possible mechanisms for resurfacing. Liquid water could be pumped to the surface by tidal flexing or thermal expansion stresses; such water might derive from a global ocean or from melting of near-surface lithospheric ice during local thermal runaways. These mechanisms are far more likely with large tidal flexing, and probably are not viable unless the tidal strain amplitude exceeds 10^{-5} (Showman and Stevenson 1996). Alternatively, slush or soft ice diapirs may buoyantly rise to the surface; this mechanism requires existence of lithospheric conduits through which the diapirs can rise. This is why the global runaway scenario is so attractive: for our thermal model, the strain amplitude exceeds 10^{-5} *only* during large global runaways; further, the *rapid* global expansion occurring during runaways allows cracking, providing conduits for slush and explaining the inferred set of graben. (Rapid expansion is required because otherwise the strain would be accommodated by viscous creep rather than cracking.) Thus, resurfacing seems problematic if a large global runaway cannot occur.

Even if Ganymede can cool to the appropriate temperatures for runaway, our

model cannot predict the time at which the runaway (and presumably resurfacing) occurred. We can easily produce a runaway at any time during solar system history simply by choosing appropriate initial temperatures, flow parameters, and orbital initial conditions. For a $\omega_1/\omega_2 \approx 2$ resonance of a given duration (say two billion years), for example, we can easily produce runaways which occur at almost any time during the resonance (except the very beginning, before the eccentricity is pumped) simply by varying $T_c(t = 0)$ by a few degrees. Similarly, for a given temperature at the onset of resonance, we can shift the time of runaway by shifting the time at which the system enters resonance (by altering ω_1 and ω_2 at $t = 0$), on which we have no constraint.

Ganymede's resurfacing took place over perhaps $\sim 10^8$ years or longer (McKinnon and Parmentier 1986). A possible explanation is that Ganymede passed through *both* the $\omega_1/\omega_2 \approx 1/2$ and $\omega_1/\omega_2 \approx 2$ (or $\omega_1/\omega_2 \approx 1/2$ and $3/2$) resonances before evolving into the Laplace resonance (Showman and Malhotra 1997). If thermal runaways occurred during both resonances, two distinct resurfacing episodes could occur, leading to a variation in ages of bright terrain. Another possibility is that thermal heterogeneities in the mantle could allow a sequence of regional runaways, perhaps spread over $\sim 10^8$ years, which together comprise a single global runaway.

We propose here an alternate scenario which might allow resurfacing in absence of a runaway. The melting point viscosities we have used assume a grain size of $d \sim 1$ mm or smaller. In *pure* ice, however, grains anneal and grow over time, possibly reaching ~ 1 m over the age of the solar system if the temperature exceeds 200 K (Azuma and Higashi 1983). The assumption of small grain size is based on the uncertain idea that Ganymede's mantle contains enough foreign inclusions (e.g., silicate particles) to limit grain growth. Because $\eta_0 \propto d^2$ (Kirk and Stevenson 1987), absence of such contamination could lead to very high viscosities. η_0 would grow rapidly after satellite formation, soon rising high enough to prevent solid state convection. Heat loss would be low and Ganymede would enter the resonance in a warm, molten state (by itself, this active state does *not* imply resurfacing; see Showman and Stevenson 1996). For $\eta_0 \geq 10^{16}$ Pa sec, viscous dissipation would be minimal, and Q might achieve 100 even

though the mantle is very warm. (In contrast, our thermal model predicts $Q \sim 1$ for such a state, for $\eta_0 \sim 10^{13}$ Pa sec.) With $Q \sim 100$, the relevant Laplace-like resonances pump Ganymede's eccentricity to ~ 0.01 for reasonable Q_J (Fig. 4.7). This yields a strain amplitude of 10^{-5} throughout the entire resonance. Thus, resurfacing might occur *without* a global runaway at all. This scenario has the additional advantage that resurfacing could easily take place over a period of several hundred million years.

If this occurred, Ganymede's ocean should still exist. At the present eccentricity, the variation in height of the tidal bulge over the one-week orbital period is ~ 16 m if a large ocean and thin ice I layer exists, but only 1 m if the satellite is fully frozen. This scenario might therefore be tested observationally by measuring the magnitude of changes in the tidal bulge from an orbiting satellite.

Regardless of which thermal model is appropriate (and whether a runaway occurred), time variability of Jupiter's tidal dissipation factor Q_J could make resurfacing far more likely. The only proposed mechanisms for achieving a time-averaged Q_J of 10^5 to 10^6 (necessary for tidal evolution of the resonances) allow Q_J drop to $\sim 10^3 - 10^4$ for short periods of time (Ioannou and Lindzen 1993, Stevenson 1983). If Q_J plummeted to $10^3 - 10^4$ for a short $\sim 10^8$ year interval while the system was locked in an eccentricity-pumping resonance, the eccentricity and therefore tidal flexing amplitude would rise. Liquid water could therefore be pumped to the surface from a much greater depth, and regional runaways occurring in lithospheric ice would be far more likely to generate liquid near the surface. The fact that Q_J might exceed 10^6 at other times would not lessen the likelihood of resurfacing during the low-Q_J phase.

Finally, the models proposed here have important implications for the thermal evolution of Ganymede's rock/iron core and hence for producing a magnetic field. The key difficulty lies in explaining how convective motion could occur in a liquid iron core at present (Stevenson 1996, McKinnon 1996). If the Galilean satellites passed through the $\omega_1/\omega_2 \approx 2$ or 3/2 resonance, Ganymede's interior would have become warm and a large internal ocean might have formed regardless of whether a runaway occurred. Upon disruption of the resonance (followed by capture into the Laplace

resonance), dissipative heating would cease and the temperature would plummet at a rate $\sim 30 - 50\,\mathrm{K/Ga}$ for half a billion years or more. Although such cooling is insufficient to drive convection in an iron core with *thermal* buoyancy (Kuang and Stevenson 1996), convection driven by *compositional* buoyancy might be possible: the cooling would cause freezing of the solid iron inner core, leaving behind sulfur rich, buoyant fluid at the base of the liquid iron outer core. Dynamo activity and a magnetic field would ensue. Only after 10^9 years would the thermal "memory" of the tidal heating disappear, at which point convection in the liquid core — and the internally generated magnetic field — would cease. Thus, if significant tidal heating occurred within the past billion years, a modern-day internally generated magnetic field could be explained. This is consistent with the suggestion of Shoemaker (personal communication 1995) that Ganymede's grooved terrain, presumably formed during the same heating event, is younger than a billion years. Further, Ganymede's substantial free eccentricity (0.0015) is probably remanent from a previous resonance passage, since neither cometary impacts nor the present Laplace resonance can excite such large values (Showman and Malhotra 1997). As the eccentricity damping time is $\sim 10^8$ years for reasonable Q/k, the inferred resonance must have ended less than a billion years ago.

5.8 References

ANDERSON, J.D., E.L. LAU, W.L. SJOGREN, G. SCHUBERT, AND W.B. MOORE 1996. Gravitational constraints on the internal structure of Ganymede. *Nature* **384,** 541-543.

AZUMA, N. AND A. HIGASHI 1983. Effects of hydrostatic pressure on the rate of grain growth in Antarctic polycrystalline ice. *J. Phys. Chem.* **87,** 4060-4064.

CASSEN, P., S.J. PEALE, AND R.T. REYNOLDS 1980. On the comparative evolution of Ganymede and Callisto. *Icarus* **41,** 232-239.

DERMOTT, S.F. 1979. Tidal dissipation in the solid cores of the major planets.

Icarus **37**, 310-321.

DORSEY, N.E. 1940. Properties of Ordinary Water Substance, Reinhold Publishing, New York.

DURHAM, W.B., H.C. HEARD, AND S.H. KIRBY 1983. Experimental deformation of polycrystalline H_20 ice at high pressure and low temperature: preliminary results. *J. Geophys. Res. Suppl.* **88**, B377-B392.

DURHAM, W.B., S.H. KIRBY, AND L.A. STERN 1992. Effects of dispersed particulates on the rheology of water ice at planetary conditions. *J. Geophys. Res.* **97**, 20,883-20,897.

FLETCHER, N.H. 1970. *The Chemical Physics of Ice,* Cambridge U. Press, London.

FRIEDSON, A.J. AND D.J. STEVENSON 1983. Viscosity of rock-ice mixtures and applications to the evolution of icy satellites. *Icarus* **56**, 1-14.

GREENBERG, R. 1987. Galilean satellites: evolutionary paths in deep resonance. *Icarus* **70**, 334-347.

HOBBS, P.V. 1974. *Ice Physics,* Oxford Univ. Press (Clarendon), London/New York.

IOANNOU, P.J. AND R.S. LINDZEN 1993. Gravitational tides in the outer planets. II. Interior calculations and estimation of the tidal dissipation factor. *Astrophys. J.* **406**, 266-278.

JONES, S.J. AND H.A.M. CHEW 1983. Creep of ice as a function of hydrostatic pressure. J. Phys. Chem. **87**, 4064-4066.

KIRBY, S.H., W.B. DURHAM, M.L. BEEMAN, H.C. HEARD, AND M.A. DALEY 1987. Inelastic properties of ice Ih at low temperatures and high pressures. *J. Phys. C suppl.* **48**, 227-232.

KIRK, R.L., AND D.J. STEVENSON 1987. Thermal evolution of a differentiated Ganymede and implications for surface features. *Icarus* **69,** 91-134.

KIVELSON, M.G., K.K. KHURANA, C.T. RUSSELL, R.J. WALKER, J. WARNECKE, F.V. CORONITI, C. POLANSKEY, D.J. SOUTHWOOD, AND G. SCHUBERT 1996. Discovery of Ganymede's magnetic field by the Galileo spacecraft. *Nature* **384,** 537-541.

KUANG, Z. AND D.J. STEVENSON 1996. Magnetic field generation in the Galilean satellites. *Eos suppl.* **77,** F437.

LUNINE, J.I. AND D.J. STEVENSON 1982. Formation of the Galilean satellites in a gaseous nebula. *Icarus* **52,** 14-39.

MALHOTRA, R. 1991. Tidal origin of the Laplace resonance and the resurfacing of Ganymede. *Icarus* **94,** 399-412.

MCKINNON, W.B. 1996. Core evolution in icy satellites. *Eos suppl.* **77,** F442.

MCKINNON, W.B. 1981. Tectonic deformation of Galileo Regio and limits to the planetary expansion of Ganymede. *Proc. Lunar Planet. Sci. Conf. 12th,* 1585-1597.

MCKINNON, W.B. AND E.M. PARMENTIER 1986. Ganymede and Callisto. In Satellites (J.A. Burns and M.S. Matthews, Eds.), pp. 718-763. Univ. of Arizona Press, Tucson.

MUNK, W.H. AND G.J.F. MACDONALD 1960. *The Rotation of the Earth,* Cambridge U. Press, London.

OJAKANGAS, G.W. AND D.J. STEVENSON 1989. Thermal state of an ice shell on Europa. *Icarus* **81,** 220-241.

PARMENTIER, E.M., S.W. SQUYRES, J.W. HEAD, AND M.L. ALLISON 1982. The tectonics of Ganymede. *Nature* 295, 290-293.

PEALE, S.J. AND P.M. CASSEN 1978. Contribution of tidal dissipation to lunar thermal history. *Icarus* **36,** 245-269.

PEALE, S.J., P. CASSEN, AND R.T. REYNOLDS 1979. Melting of Io by tidal dissipation. *Science* **203,** 892-894.

REYNOLDS, R.T. AND P.M. CASSEN 1979. On the internal structure of the major satellites of the outer planets. *Geophys. Res. Lett.* **6,** 121-124.

ROSS, M.N. AND G. SCHUBERT 1987. Tidal heating in an internal model of Europa. *Nature* **325,** 133-134.

SCHUBERT, G., D.J. STEVENSON, AND K. ELLSWORTH 1981. Internal structures of the Galilean satellites. *Icarus* **47,** 46-59.

SHOEMAKER, E.M. AND R.F. WOLFE 1982. Cratering time scales for the Galilean satellites. In *Satellites of Jupiter* (D. Morrison, Ed.), pp. 277-339. Univ. of Arizona Press, Tucson.

SHOWMAN, A.P. AND R. MALHOTRA 1997. Tidal evolution into the Laplace resonance and the resurfacing of Ganymede. *Icarus* **127,** 93-111.

SHOWMAN, A.P. AND D.J. STEVENSON 1996. Resurfacing of Ganymede and other icy satellites by passage through orbital resonance. Submitted to *Icarus.*

SOLOMATOV, V.S. 1995. Scaling of temperature- and stress-dependent viscosity convection. *Phys. Fluids* **7,** 266-274.

SQUYRES, S.W. 1980. Volume changes in Ganymede and Callisto and the origin of grooved terrain. *Geophys. Res. Lett.* **7,** 593-596.

SQUYRES, S.W. 1982. The evolution of the tectonic features on Ganymede. *Icarus* **52,** 545-559.

STEVENSON, D.J. 1983. Anomalous bulk viscosity of two-phase fluids and implications for planetary interiors. *J. Geophys. Res.* **88,** 2445-2455.

STEVENSON, D.J. 1996. When Galileo met Ganymede. *Nature* **384,** 511-512.

TITTEMORE, W.C. 1990. Chaotic motion of Europa and Ganymede and the Ganymede-Callisto dichotomy. *Science* **250,** 263-267.

WEAST, R.C. (Ed.) 1987. *CRC Handbook of Chemistry and Physics*, 68th ed. Chemical Rubber Company, Boca Raton, Florida.

WEERTMAN, J. 1973. Creep of ice. In *Physics and Chemistry of Ice* (E. Whalley, S.J. Jones, and L.W. Gold, Eds.), pp. 320-337. Roy. Soc. of Canada, Ottowa.